Modification of Precipitation in Mid-Latitude Cyclones Passing over a Coastal Mountain Range

Joseph Paul Zagrodnik

A dissertation

submitted in partial fulfillment of the

requirements for the degree of

Doctor of Philosophy

University of Washington

2019

Reading Committee:

Lynn A. McMurdie, Chair

Robert A. Houze

Cliff Mass

Program Authorized to Offer Degree:

Atmospheric Sciences

University of Washington

Abstract

Modification of Precipitation in Mid-Latitude Cyclones Passing over a Coastal Mountain Range

Joseph Paul Zagrodnik

Chair of the Supervisory Committee:
Dr. Lynn McMurdie
Department of Atmospheric Sciences

As mid-latitude cyclones pass over a coastal mountain range, the processes producing their clouds and precipitation are modified, leading to considerable spatial variability in precipitation amount and composition. Surface, radar, and aircraft observations from the 2015-16 Olympic Mountains Experiment (OLYMPEX) field campaign and realistic, high-resolution WRF model runs provided complimentary perspectives on the dynamic and microphysical processes associated with terrain-induced precipitation processes. To the first order, the location of the mid-latitude cyclone relative to the mountain barrier determines the likely modes of precipitation enhancement or lack thereof. The prefrontal, warm, and postfrontal sectors have distinct synoptic-scale environmental conditions (flow, stability, and temperature), which were shown to exert significant controls over the flow and microphysical response upon encountering complex terrain.

Prefrontal sectors contained homogeneous stratiform precipitation with a slightly enhanced ice layer on the windward slopes and rapid diminishment to a lee rain shadow. A stably stratified coastal environment deflected the low-level flow in front of the barrier. Stationary mountain waves over the smaller-scale windward ridges had minimal impact on the overall precipitation pattern due to a lack of generation of cloud water or generation of small raindrops at low elevations. Warm sectors contained a broad spectrum of sizes and concentrations of raindrops where high precipitation rates were achieved from varying degrees of both liquid and ice precipitation-generating processes. Significant quantities of cloud water were produced over coastal foothills and lower-windward slopes, leading to a remarkable enhancement of precipitation on the lower-windward slopes. Enhancement in the ice layer occurred directly over the barrier where the ice particles were further advected downstream by cross-barrier winds and spilled over into the lee.

As a whole, this dissertation demonstrates that precipitation enhancement over the Olympic Mountains depends on a complex mix of warm low-level rain processes and upper level ice processes. The relative importance of these processes depends on both the synoptic system and the position on the barrier. The greatest precipitation enhancement on the windward slopes occurred when both warm and ice processes were amplified by flow over the barrier and were acting together during the warm sectors of strongly-forced atmospheric river-type storms. The least precipitation enhancement occurred when the warm processes were absent. Lee side precipitation must overcome persistent descent on the downstream side of the higher windward ridges.

TABLE OF CONTENTS

LIST OF FIGURES

LIST OF TABLES

ACKNOWLEDGEMENTS

First and foremost, I would to thank my advisor, Lynn McMurdie, for mentoring me through grad school, for being continually available for discussions, and for being a role model scientist and leader in many ways. I would also like to thank Bob Houze for giving me the opportunity to study at the University of Washington, for co-advising my dissertation, and for providing considerable advice and support. Both Lynn and Bob provided detailed and constructive critiques of my writing and presentations and while giving me the space to be creative and explore topics that interested me. I would also like to thank my committee members: Cliff Mass for feedback on my written dissertation and numerous engaging discussions on the weather and my career, Dale Durran for many theoretical studies and conversations that provided the framework for this dissertation, and Jessica Lundquist for providing the perspective of a hydrologist and serving as my Graduate School Representative.

I am thankful to past and present members of the Mesoscale Group for their feedback including Angela Rowe, Jen DeHart, Scott Powell, and Hannah Barnes. Stacy Brodzik provided data and computing support and Beth Tully provided graphics support. Harry Edmon and David Warren provided additional technical support. Neal Johnson, Steve Domonkos, and Allen Hart provided instrumentation support. I was lucky to be a part of the UW Department of Atmospheric Sciences and I thank all of the staff and graduate students for the collegial, fun, and intellectually stimulating environment. I especially thank the 2013 graduate student class for their support and friendship.

This research would not have been possible without the support of numerous agencies and individuals during the OLYMPEX field campaign. Bill Baccus and C. J. Urnes from Olympic National Park provided considerable support on ground site design, logistics, deployment, and maintenance. Matt Wingo from NASA designed many components of the ground instruments and provided mentorship on the technical aspects of instrument deployment. Ali Tokay, Dave Wolff, and Larry Bliven provided assistance with disdrometer data that was integral to this dissertation. I would especially like to thank the Quinault Indian Nation for allowing us to deploy instruments on their land and for supporting the OLYMPEX campaign.

Finally, I would like to thank my immediate and extended family, especially Mom and Dad for supporting my pursuit of science from a young age and Beth Boomgard for being my partner and best friend.

Chapter 1. INTRODUCTION

1.1 BACKGROUND AND UNANSWERED QUESTIONS

The west coasts of the Americas are frequented by landfalling extratropical cyclones during the cold seasons. These storms produce copious amounts of rain and snow when they pass over coastal mountain ranges. Excessive rainfall contributes to hazards such as flooding and landslides. Snow accumulation is a crucial source of warm season water supply and hydroelectricity generation. Understanding cold season precipitation in mountains is crucial for predicting these events and mitigating negative effects. Additionally, understanding the processes responsible for enhanced precipitation over mountains is necessary for 1) advancing ongoing efforts to measure precipitation from space and 2) parameterizing microphysical processes in numerical models, which are moving toward finer scales and more explicit characterizations of precipitation microphysics.

Precipitation over midlatitude west coastal mountain ranges is usually associated with baroclinic cyclones containing distinct cloud patterns that are modified during passage over complex terrain. The cloud and precipitation structures within these cyclones are forced on a hierarchy of scales including large-scale lifting associated with the baroclinic wave, frontogenetic processes associated with airstreams of contrasting thermal properties, and mesoscale rainbands or convective elements embedded within these larger features. An idealized storm sector paradigm proposed by Nagle and Serebreny (1962) and subsequently modified by numerous studies divides maritime cyclones into four characteristic sectors: prefrontal (early), frontal (middle), postfrontal (late), and warm sector (Kreitzberg and Brown 1970; Browning 1974; Houze et al. 1976; Matejka et al. 1980; Houze 1981; Medina et al. 2007; Houze 2014; Houze et al. 2017). Figure 1.1 shows a

conceptual diagram of the storm sector paradigm. The prefrontal sector contains the leading edge of precipitation ahead of the occluded or warm front and is associated with warm advection and rising melting levels. The frontal sector is a broad, elongated cloud shield within which the circulation from a cold or occluded front generates banded precipitation. The broad, moist warm sector located ahead of the cold frontal zone sometimes contains an extensive narrow zone of water vapor flux commonly called an "atmospheric river" (Newell et al. 1992; Zhu and Newell 1994, 1998; Ralph et al. 2004; Neiman et al. 2008; Warner et al. 2012). Behind the cold front, the postfrontal sector is associated with cold advection and low melting levels. Precipitation consists mainly of small-scale convective elements, which sometimes form into bands or other mesoscale features.

The kinematic and thermodynamic environment surrounding a terrain feature characterizes the mechanisms by which clouds and/or precipitation may be modified within each of the above synoptic regimes (Smith 1979; Roe 2005; Houze 2012). In stable flow approaching a barrier, the response of the flow to the terrain depends on the height of the terrain, h; the upstream flow velocity, U; and the upstream stability, N. These factors are often combined into a non-dimensional Froude Number, $Fr = U/Nh$ (Markowski and Richardson 2010; Houze 2014) indicating the potential for the incoming air to flow over the terrain (high Fr) or be blocked/dammed (low Fr, Fraser et al. 1973; Rotunno and Ferretti 2001; Houze et al. 2001; Houze 2014). Unblocked, unsaturated air parcels will adiabatically ascend terrain until the point of saturation, resulting in the formation of clouds and the release of latent heat to the environment. Within clouds, the rate of condensation is closely related to the rate of change of the saturation vapor pressure, which decreases exponentially with temperature (and hence with height). This thermodynamic constraint

may result in the maximum precipitation occurring below the top of a sufficiently tall mountain range (Frei and Schär, 1998).

To generate precipitation, the impinging airmass must rise over a blocked or reversed flow layers prior to reaching the adjacent mountain range. Conversely, unblocked flow ascends directly over the mountain barrier. Numerous studies have shown evidence of different precipitation patterns between blocked and unblocked flow regimes (Houze et al. 2001; Rotunno and Ferretti 2001; Neiman et al. 2002; James and Houze 2005). Blocked flow tends to enhance precipitation upstream of the windward mountains as incoming air lifts over the lower-level stable layer. Unblocked flow results in a precipitation maximum near or on the slopes of the first major peak encountered by the incoming air. The precise precipitation pattern also depends on the microphysics of particle growth, which may be accelerated by a number of different processes. Medina and Houze (2003) found that potentially unstable layers within an unblocked flow regime coincided with the occurrence of convective cells and enhanced coalescence and riming on the lower windward slopes of the Alps. Kumjian et al. (2014) found that potentially unstable layers drove the formation of convective "generating cells" with pockets of supercooled liquid water during Colorado snowstorms.

Other proposed microphysical growth mechanisms do not require convection and can occur within stable or neutral flow regimes. Bergeron (1968) suggested that precipitation-sized particles from a preexisting "seeder" cloud could collect smaller cloud drops formed locally by a lower "feeder" cloud as air lifts over small hills. Often, the two cloud layers are not actually distinct but rather part of a deep layer of nimbostratus. At other times rainfall may occur with only the lower cloud layer. White et al. (2003) describes this warm or nonbrightband rain over the California coastal range, finding that coalescence alone is enough to produce appreciable rain in shallow,

warm cloud layers. Kingsmill et al. (2006) further showed that periods of nonbrightband rain could be interspersed with bright band rain depending on the synoptic storm sector passing overhead. The sheared boundary between a lower blocked layer and the free atmosphere has also been hypothesized to accelerate cold processes such as aggregation and/or riming through the generation of turbulent cells sometimes associated with Kelvin-Helmholtz instabilities (Medina and Houze 2005, 2015; Barnes et al. 2018).

As a whole, these studies highlight the complexity of precipitation production over mountains. The precipitation in a given storm likely results from a varying combination of both warm processes (condensation/collision-coalescence) and cold processes (riming, accretion, aggregation) that evolve with the changing synoptic situation or storm sector. Additional studies are needed to determine the relative importance of these processes within different types of storms crossing over west coastal mountains.

The complex interplay between the dynamical and microphysical processes described above is expected to also apply to precipitation reaching the lee side. As on the windward side, high-terrain/leeside precipitation would be affected by the variations in flow, stability, and melting level that occur with the passage of frontal cyclones. The stability and directional shear determine the vertical extent of mountain waves and associated clouds. Storms with higher melting levels have more liquid hydrometeors at crest level with faster fall speeds that are more likely to fall out on the windward size. Hobbs et al. (1973) showed how the rate of particle riming could determine if particles grow fast enough to fall out on the windward side or are advected downwind to the lee side. Jiang and Smith (2003) and Smith and Barstad (2004) generated realistic-looking precipitation patterns by parameterizing the time scales of microphysical growth, particle fallout, and advection. This framework has been shown to accurately reproduce small-scale precipitation

features on the windward side of the Olympic Mountains (Anders et al. 2007) but underestimates precipitation on the lee side. In some cases with low melting levels, the precipitation maxima can actually occur on the lee side of small-scale ridges, a consequence of downwind advection and mountain wave descent (Zängl 2007; Minder et al. 2008). Mass et al. (2015) and Siler et al. (2016) investigated the synoptic and dynamic mechanisms responsible for weak and strong rain shadows in the lee of the Washington/Oregon Cascades. From a synoptic viewpoint, weaker rain shadows are favored in the prefrontal period of midlatitude cyclone passages, prior to the erosion of the preexisting stable airmass in the lee. Storms with weaker rain shadows tend to have muted wave activity, as a consequence of low-level cold, stagnant air suppressing descent in the lee.

Leeside observational data are rare. Observations of precipitation processes by dual-polarization radar or ground disdrometers are especially limited. Colle and Mass (1996) and Medina et al. (2005) both described aircraft observations of leeside mountain waves over the Olympic Mountains and Oregon Cascades respectively. Doppler radar observations in MAP and IMPROVE-2 (Medina et al. 2005) extended somewhat to the lee side but were limited by terrain blockage and beam widening. Unlike the windward side, there are virtually no detailed studies of precipitation reaching the lee side using modern instrumentation such as disdrometers and dual-polarization radars. Accurately predicting leeside precipitation in realistic high-resolution numerical models requires that this observational gap be filled. Leeside precipitation is also important from a hydrologic perspective, as the precipitation scarcity limits water resources more than the rainy windward sides.

To summarize, the above background highlights several open questions relating to the dynamical and microphysical processes controlling precipitation during midlatitude cyclone passages over complex terrain:

1) What are the relative roles of liquid and ice microphysical processes in producing enhanced precipitation over windward slopes of west coastal mountain ranges?
2) What dynamic and microphysical processes control characteristics of the rain shadow (namely, its overall size and the sharpness of its boundaries)
3) What is the origin and composition of precipitation reaching the lee side?

1.2 THE OLYMPIC MOUNTAINS EXPERIMENT (OLYMPEX)

The 2015-16 Olympic Mountains Experiment (OLYMPEX, Houze et al. 2017) dataset presents an unprecedented opportunity to address these questions because its extensive and technologically advanced network observed the detailed dynamics, thermodynamics, and microphysical processes on the windward, high-terrain, and leeward portions of the Olympic Mountains on a range of scales. OLYMPEX exceeded previous field campaigns in terms of the variety of instrumentation and level of technology deployed. The extensive radar and aircraft dataset enables a multifaceted study that examined the dynamical and microphysical evolution of precipitation in midlatitude cyclones as they transitioned from offshore to the windward slopes and valleys, to the high terrain, and finally to the lee side.

The Olympic Peninsula in Washington State was an ideal venue for this campaign because it receives copious amounts of precipitation from midlatitude cyclones arriving frequently from the Pacific Ocean and abruptly transitioning to mountainous terrain. The author of this dissertation participated extensively in the site selection, deployment, and maintenance of the OLYMPEX ground network as well as in the post-processing and quality control of the final dataset. Figure 1.2 shows the OLYMPEX observational network. The OLYMPEX ground network measured over 65 distinct synoptic storms that produced seasonal precipitation totals that ranged from 1700 to 4900 mm on the windward slopes (Figure 1.3). Ground sites were set up on the western side of the

Olympic Peninsula within and near the Quinault Valley, which is a narrow southwest-northeast oriented rain-forested valley on the windward side of the Olympic Mountains. Rain gauges and disdrometers were placed at over a dozen sites along the valley and surrounding ridges. Three vertically pointing Micro Rain Radars (MRRs) were deployed at windward-side ground sites connected to the power grid. Another MRR and two disdrometers were deployed at the high-terrain Hurricane Ridge site. In addition to these surface sites, Professor Jessica Lundquist's group installed tree-mounted snow cameras to monitor snow depth, and permanent SNOTEL sites provided information on snow water equivalent at high elevation sites (Currier et al. 2017).

The white dashed line in Figure 1.2 outlines the region where aircraft missions were conducted during OLYMPEX. Two NASA aircraft (DC-8 and ER-2) flew above the clouds with onboard radars and passive microwave sensors. The DC-8 also launched dropsondes over the ocean to document upstream conditions. The University of North Dakota Citation aircraft flew primarily within the clouds with cloud microphysics instrumentation and collected in situ observations of liquid and ice particle characteristics at a wide range of temperatures.

In addition to NWS operational radars, four scanning dual-polarization Doppler radars, operating at several frequencies were installed for OLYMPEX and provided detailed observations of the vertical and horizontal variability of hydrometer characteristics in coordination with the aircraft and ground network. The coastal radar site had two radars: the NASA dual-polarization S-band radar (NPOL) and the NASA Ku-/Ka-band Dual-polarization Doppler radar (D3R). In order to maximize vertical resolution of dual-polarization data, the NPOL and D3R radars operated primarily in range height indicator (RHI) mode in the wedge- shaped sectors indicated in Figure 1.2, one over ocean and one over land. The land sector was supplemented by the Doppler on Wheels (DOW) X-band dual-polarization Doppler radar, which provided additional coverage in

the Quinault Valley below the lowest NPOL beam. The DOW operated exclusively in RHI mode. The Environment Canada X-band dual-polarization Doppler radar was operated on Vancouver Island to provide views of the leeside precipitation structure. It executed RHI scans in a zone including the Hurricane Ridge ground site.

To address the questions at the end of section 1.1, the dissertation is organized into three chapters, corresponding to combinations of data sources and geographic regions of interest. Each chapter applies OLYMPEX observations or high-resolution model output to determine the dominant dynamical and microphysical processes producing precipitation within the broader synoptic context. The dominant processes often differ by geographic region. Five different regions are referenced throughout this work. The *ocean* region contains the open waters of the Pacific Ocean more than ~20 km offshore. The *coast* region contains the near coastal waters (within ~20 km of land) and the near coastal plains and foothills (< 200 m elevation). The *windward* region contains the more significant network of ridges (~500-1,500 m elevation) and valleys on the south and west facing sides of the main Olympic Mountains barrier. The *high terrain* contains the interior valleys, river source regions, and taller mountains (~1,000-2,500 m elevation). The *lee side* contains the more abruptly sloped north-northeast edge of the main Olympic Mountains barrier and the coastal portion of the Strait of Juan de Fuca.

Specific objectives in each chapter are as follows:

1) *Chapter 2*: This chapter examines the multiscale relationships between synoptic regimes, precipitation patterns, and modes of drop-size distributions over the windward slopes of the mountain range within periods of continuous stratiform precipitation.
2) *Chapter 3:* This chapter uses airborne radar observations to examine the vertical structure of precipitating clouds across the full transect of all five geographic regions.

3) *Chapter 4:* This chapter uses realistic, high-resolution numerical simulations to examine the relative importance of warm and ice precipitation processes across both the full barrier scale of the Olympic Mountains and localized small-scale ridges.

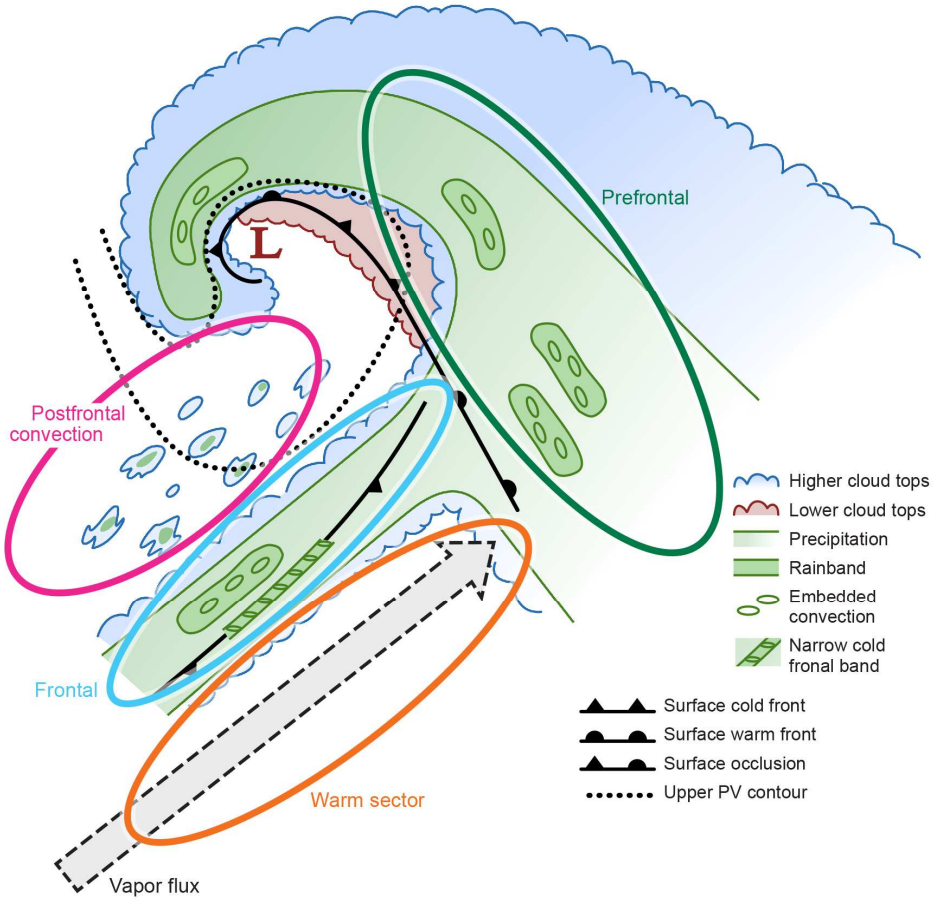

Figure 1.1: Idealized diagram of the sectors of an extratropical cyclone passing over the Olympic Mountains. Modified from Houze et al. (2017).

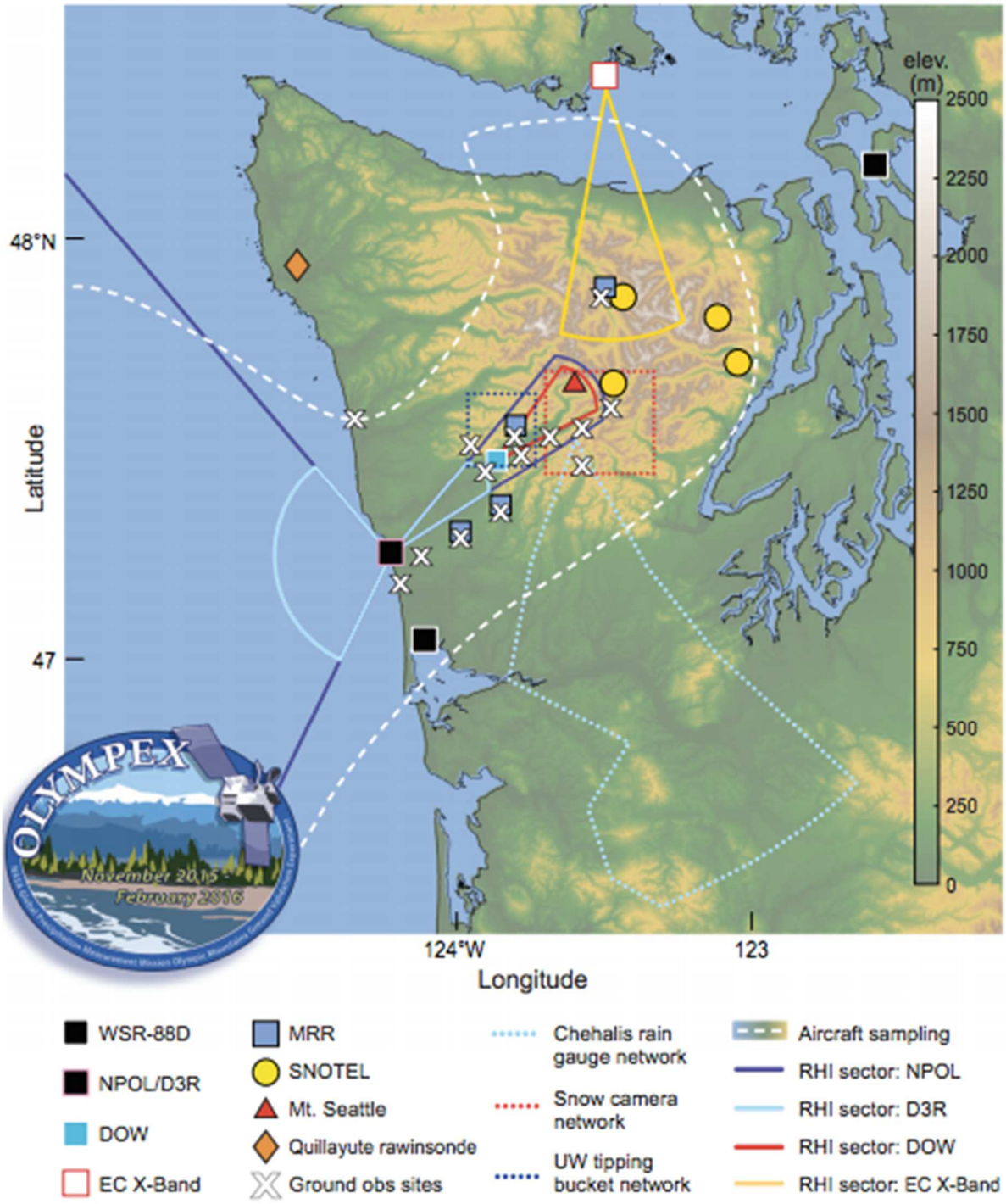

Figure 1.2: Location of OLYMPEX radars and ground sites used in this study. The black line denotes the 52° NPOL RHI and the 58.4° DOW RHI. The right panel includes the total measured precipitation from 10 October 2015 to 30 April 2016. Figure reproduced from Houze et al. (2017).

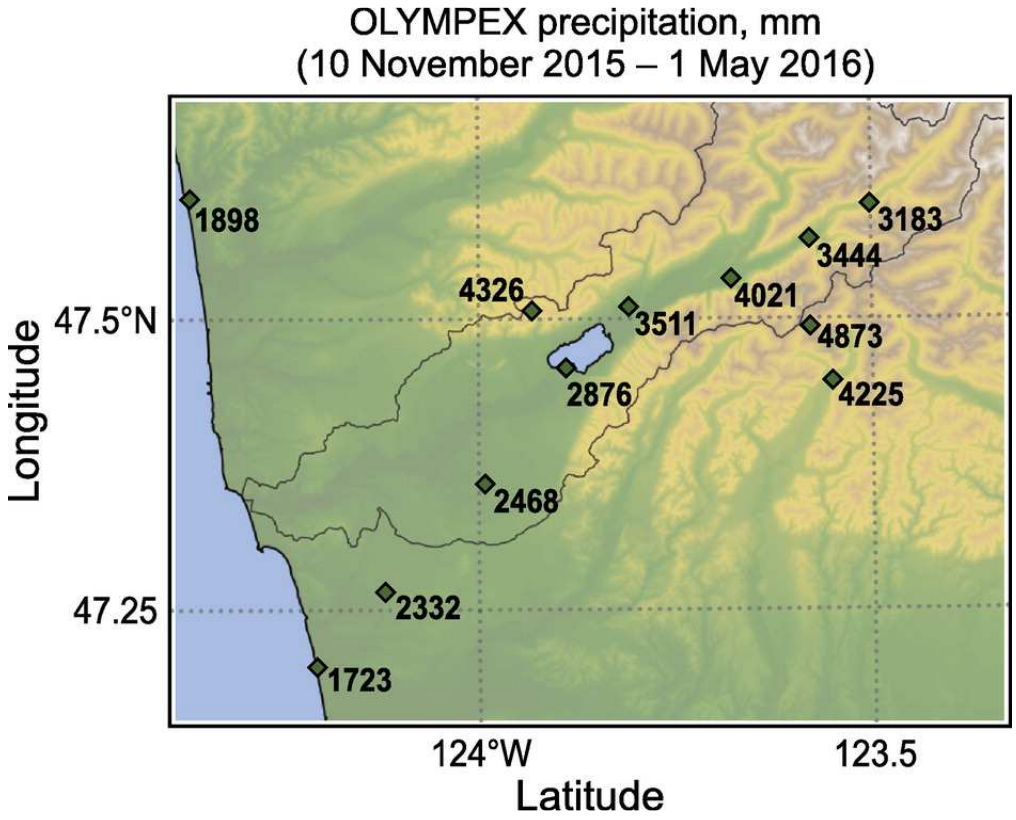

Figure 1.3: Total accumulated liquid water equivalent precipitation at OLYMPEX ground sites from 10 Nov 2015 through 1 May 2016. The elevation scale is as in Figure 1.2. Figure reproduced from Houze et al. (2017).

Chapter 2. STRATIFORM PRECIPITATION PROCESSES IN CYCLONES PASSING OVER A COASTAL MOUNTAIN RANGE

2.1 ABSTRACT

The Olympic Mountains Experiment (OLYMPEX) documented precipitation and drop-size distributions (DSDs) in landfalling mid-latitude cyclones with gauges and disdrometers located at various distances from the coast and at different elevations on the windward side of the mountain range. Statistics of the drop-size and gauge data for the season and case study analysis of a high-rainfall producing storm of the atmospheric river type show that DSDs during stratiform raining periods exhibit considerable variability in regions of complex terrain. Seasonal statistics show that different relative proportions of drop sizes are present, depending on synoptic and mesoscale conditions, which vary within a single storm. The most frequent DSD regime contains modest concentrations of both small and large drops with synoptic factors near their climatological norms and moderate precipitation enhancement on the lower-windward slopes. The heaviest rains are the most strongly enhanced on the lower slope and have DSDs marked by large concentrations of small-to-medium drops and varying concentrations of large drops. During the heavy rain period of the case examined here, the low-level flow was onshore and entirely up-terrain, the melting level was ~2.5 km, and stability moist-neutral, so that large amounts of small raindrops were produced. At the same time, melting ice particles produced at upper levels contributed varying amounts of large drops to the DSD, depending on sub-synoptic variability of storm structure. When the low-level flow is directed downslope and offshore, small drop production at low altitudes is reduced or eliminated.

2.2 INTRODUCTION

The west coast of North America is frequented by land-falling extratropical cyclones from the Pacific Ocean during the fall through early spring. When these storms pass over coastal mountain ranges, they produce copious precipitation on the windward slopes, frequently contributing to hazards such as flooding and landslides. These storms are also responsible for the accumulation of snow at higher elevations, which is crucial for summer water supply. Understanding the processes responsible for producing precipitation in these storms has been the subject of numerous past field programs (e.g. Hobbs et al. 1971; Houze et al. 1976; Hobbs 1978; Matejka et al. 1980; Bond et al. 1997; Ralph et al. 1999; Stoelinga et al. 2003; Houze and Medina 2005; Medina et al. 2007). Similar processes also occur on the west coast of South America (Barret et al. 2009; Viale et al. 2013; Garreaud et al. 2016; Massmann et al. 2017).

It is well known that the precipitation associated with these landfalling extratropical storms is enhanced on the windward slopes of west-coastal mountains. Neiman et al. (2002) used wind profiler observations to show that the rain rate on windward slopes in the California coastal range is highly correlated with the intensity of unblocked low-level flow. When the low-level flow is blocked, rain rate correlates with the flow strength near the mountaintop, likely from the low-level flow lifting over the blocked air. Minder et al. (2008) used case studies and climatologies from both rain gauges and high-resolution model output to demonstrate that enhanced precipitation growth by collection of cloud water occurs during periods when stable flow ascends over the windward slopes of the Olympic Mountains. White et al. (2003) and Kingsmill et al. (2006) used profiling radars to show that collision-coalescence can produce precipitation on the low-elevation windward slopes of the California coastal range without radar indication of ice-phase hydrometeors. Martner et al. (2008) further illustrated that this “nonbrightband rain” was

associated with greater concentrations of small drops, while the presence of melting ice hydrometeors from deeper clouds, when present, shifted the drop-size distribution (DSD) toward larger drop sizes and smaller drop concentrations. These studies have highlighted how precipitation production depends on the relative role of warm processes (condensation/collision-coalescence) and cold processes (riming, accretion, aggregation). Much work remains, however, to understand the factors that determine the relative roles of the warm and cold processes, as they typically occur within the same storm. This paper aims to shed light on how the relative importance of warm and cold processes varies within storms passing over west coastal mountains.

The 2015-16 Olympic Mountains Experiment (OLYMPEX, Houze et al. 2017) provides unprecedented data for this purpose. OLYMPEX was a physical and hydrologic ground validation project for the U.S./Japan Global Precipitation Measurement (GPM) satellite mission. However, it was conducted in a way that also facilitates study of the mechanisms of precipitation in Pacific frontal systems and how passage of these storms over coastal mountains modifies the precipitation processes. OLYMPEX deployed extensive observational assets, including four NASA research aircraft, four dual-polarization Doppler research radars, rain gauges, particle-size distribution measurements, and Micro Rain Radars at a variety of elevations ranging from the coast to middle elevations. At the latitude of OLYMPEX, the melting layer in storms arriving from the Pacific Ocean typically is at a relatively low-altitude so that both low-level warm growth of drops and melting ice particles from higher levels contribute to the precipitation, but to differing degrees depending on the sector of the storm passing over the region (Figure 1.1), and on smaller scale variability within each storm sector. This study focuses on ground-based measurements of DSDs in OLYMPEX in combination with synoptic and radar data. The goal is to elucidate the mechanisms of precipitation growth and how these processes are enhanced over the Olympic

Mountains. We analyze the statistics of DSD data over the season in which OLYMPEX occurred, and to further elucidate the precipitation processes, we examine an atmospheric river type storm that produced the heaviest precipitation during OLYMPEX.

2.3 DATA

2.3.1 *Synoptic Data*

The synoptic data used in this study to describe the dynamic and thermodynamic properties of the maritime flow impinging upon the mountains is from the North American Regional Reanalysis (NARR, Mesinger et al 2006). The NARR dataset (NOAA/OAR/ESRL PSD, 2004) has 3 h time resolution, 32 km horizontal grid spacing and 25 hPa vertical resolution. The 925 hPa wind magnitude and direction provides low-level flow context. NARR includes a derived 3 h horizontal water vapor flux accumulation parameter that we converted to instantaneous Integrated Vapor Transport (IVT, kg m^{-1} s^{-1}) to compare to the analyses in atmospheric river studies such as Nieman et al. (2008). The melting level is the height of the highest NARR pressure level with a temperature above 0°C. Similar to Medina and Houze (2015), the upstream low-level stability is evaluated using the dry and moist Brunt Väisälä frequency, N_d^2 and N_m^2, respectively, calculated for the 950 – 850 hPa layer according to Durran and Klemp (1982). These parameters are evaluated at the 0.3° grid box centered on the coast upstream of the Olympic Mountains at the location of the S-band radar installed during OLYMPEX (marked as NPOL in Figure 2.1).

2.3.2 *OLYMPEX Data*

Surface sites installed for OLYMPEX collected precipitation and drop-size distribution data during the entire cold season from 10 October 2015 to 30 April 2016 (Petersen et al. 2017c).

Particle Size and Velocity-2 (Parsivel) disdrometers were co-located with either pairs of tipping bucket rain gauges at low elevation sites or Pluvio^2-400™ weighing buckets designed to measure either liquid or frozen precipitation at high elevation sites. Figure 2.1 indicates the five ground sites used in this study and the total precipitation observed at these sites during the entire cold season. Table 2.1 lists exact locations and elevations. The three low-elevation sites – Fishery, Bishop Field, and Graves Creek – were within the Quinault Valley. Prairie Creek was located at an intermediate elevation, often below the snow line, on the first significant ridge encountered by westerly or southwesterly flow. This ridge was previously instrumented by Minder et al. (2008). The Wynoochee site was in an area of higher terrain to the south of the Quinault Valley on the south side of the Olympic Mountains. The rain gauges and Pluvio did not have wind shields so there was likely some under-catch (Nespor and Sevruk 1999). A co-located NOAA Climate Reference Network site (CRN) with a wind-shielded gauge at Bishop Field differed from the OLYMPEX gauges by only 3-5%. The windier Wynoochee site compared favorably with a better-protected tipping bucket site on the same ridge in raining periods. Under-catch was likely greater in snowing periods, but the NARR melting level was only below 1.2 km in 19 of the 181 3 h periods and comparison of precipitation measurements between the wind-shielded Buckinghorse SNOTEL and Wynoochee sites (not shown) suggests that the conclusions drawn from the Wynoochee site are applicable elsewhere in the Olympic Mountains.

The case study discussed in Section 2.5 used data from two radars. The NASA dual-polarization S-band Doppler radar (NPOL) was located on a coastal hill with direct views of the Quinault Valley. The NSF-sponsored mobile dual-polarization X-band Doppler radar (DOW) of the Center for Severe Weather Research was operated in the Quinault Valley where it scanned underneath the lowest NPOL beam in order to resolve finer details of the processes within the

valley. We focus here on a vertical cross section (RHI) along the DOW 58.4° azimuth and NPOL 52° azimuth. This configuration diagrammed by the solid line in Figure 2.1 accounts for the rightward bend of the Quinault Valley.

2.3.3 *Selection of three-hour samples*

To compile statistics, we combined all of the rain gauge and disdrometer data into 3 h periods centered on the synoptic times of the NARR data (0000 UTC, 0300 UTC, etc.). Other recent statistical studies of disdrometer data (e.g. Thompson et al. 2015) have used a much shorter (usually 1-min) interval because they were analyzing convective precipitation, which occurs on short time and space scales. In OLYMPEX, the precipitation was primarily stratiform, and the DSDs remained consistent for many hours at a time, tending to shift only when there were substantial synoptic or mesoscale environmental changes. To be selected for inclusion in our statistics, a 3 h period must have had three consecutive hours with precipitation rates > 1 mm h^{-1} at one or more ground sites. In order to focus on stratiform precipitation periods, we did not include postfrontal convective periods. Most postfrontal periods did not meet the 1 mm h^{-1} criterion, and those that did were excluded based on subjective examination of radar data for the presence of discrete convective cells. However, some postfrontal periods with predominantly non-convective character such as comma clouds, occluded fronts, or cutoff lows did meet the continuous 3 h consecutive precipitation criteria and were retained in the dataset. Some of the accepted stratiform periods had shallow embedded (generating) cells aloft. No deep convection was observed in any of the time periods that met the 3 h consecutive rainfall criteria. Some precipitation data was eliminated from individual sites because of snow contamination in the tipping buckets, isolated power outages, and overflowing of the Wynoochee Pluvio bucket. Mean differences between

various samples of 3 h rain rates or synoptic parameters are compared with two-sided t-tests and considered significant at the 95% confidence level or greater.

2.3.4 *Analysis of disdrometer data*

The Parsivel measurements were used for the DSD data since they were installed for the full 2015-16 cold season. The Parsivel is a laser optical disdrometer that measures the size and fall velocity of hydrometeors passing through a 180 x 30 x 1 mm sheet laser. The raw output contains 32 size and velocity bins from 0.2 to 25 mm diameter and 0.2 to 20 m s^{-1} velocity, respectively, with 10 s time resolution. The Parsivel output assumes drops are falling straight down and corrects drops greater than 1 mm for oblateness. The 3 h DSDs were computed following Eq. 6 of Tokay et al. (2014) using terminal fall velocities from Atlas et al. (1973) and a time interval of 3 h centered on the synoptic times (e.g. 0000, 0300 UTC, etc.). Within each 3 h period, 10 s periods with error flags in the Parsivel data or frozen precipitation were removed. If less than 50% of the 3 h period had good data, the entire 3 h period was removed. The final accepted Parsivel dataset included 209 three-hour periods at the Fishery, 217 at Prairie Creek, 217 at Bishop Field, and 192 at Graves Creek. Over 90% of the raw Parsivel and gauge data that met the 1 mm h^{-1} criterion was accepted. The 3 h DSDs were the basis for the analysis of the season-long statistics discussed in Section 2.4. The DSDs were calculated in 1 h segments for analysis of the case study presented in Section 2.5. For high-resolution of DSDs of the case study, the DSDs were calculated in 5 min segments.

To make comparisons between DSDs from different time periods, it is important to use an appropriate DSD model. DSDs typically can be approximated by a gamma distribution:

$$N(D) = N_o D^{\mu} \exp(-\Lambda D) \tag{2.1}$$

where D is drop diameter, and the parameters of the distribution are: the slope parameter Λ, intercept parameter N_o, and shape parameter μ. Here slope and intercept refer to a plot of logN_o on the y-axis vs D on the x-axis. A series of papers (Ulbrich 1983; Willis 1984; Testud et al. 2001; Bringi et al. 2002, 2009; Thompson et al. 2015) have led to the understanding that Λ and μ are interrelated, and consequently that a gamma distribution of a given liquid water content LWC can be represented by an exponential distribution for which the intercept parameter N_w in m^{-3} mm^{-1} given by:

$$N_w = \frac{1.81 \times 10^5 LWC}{\pi \rho_w D_o^4} \tag{2.2}$$

where the density of liquid water has the value 1 g cm^{-3}, LWC has units of g m^{-3}, and D_o is in mm. N_w is referred to as the "normalized intercept parameter." Because every combination of N_w and D_o correspond to a given LWC, if the DSD is approximately a gamma distribution, an N_w –D_o coordinate system is useful for characterizing observed DSDs because each measured DSD can be mapped using its specific combination of N_w and D_o. Figures 2.2, 2.3, 2.4, and 2.6 use this coordinate system, wherein N_w is a proxy for the number concentration of drops and D_o is a proxy for their predominant drop size. For each observed combination of N_w and D_o, we can indicate the number of observations, mean rain rate, and synoptic parameters observed at the time of the DSD measurement. As a result of using this plotting method, our figures are directly comparable to those of Thompson et al. (2015), who studied DSDs in tropical oceanic convective storms, in contrast with the orographically influenced stratiform midlatitude frontal systems examined here.

2.4 RELATIONSHIP BETWEEN DSD, SYNOPTIC ENVIRONMENT, AND OROGRAPHIC ENHANCEMENT FOR THE FULL 2015-16 COLD SEASON

This section describes statistics of the stratiform precipitation observations for the full 2015-16 cold season. As discussed in Section 2.3.4, Figure 2.2 shows the rain rate R for each of the combinations of three-hourly values of D_o and N_w measured by the OLYMPEX disdrometers over the whole season of the campaign. Results are shown for two windward sites:

- Fishery—representing near coastal conditions
- Prairie Creek—representing conditions at medium elevation on the windward side of the mountains, where some of the greatest amounts of rain were observed.

The average rain rates corresponding to different combinations of (N_w, D_o) in Figure 2.2c,d were calculated from the dual tipping buckets rather than the Parsivel estimates, which depend on particle fall velocity assumptions.[1] The rain rate of the most frequent DSD was 2.7 mm h^{-1} at both sites. This rate is similar to the mean rain rate during the entire season at Fishery of 2.5 mm h^{-1} but considerably less than the 4.7 mm h^{-1} mean rain rate at higher-elevation Prairie Creek.

The distributions shown in Figure 2.2 for Prairie Creek and Fishery have the same general shape and similar modes to each other, with the frequency maxima in the mid-ranges of number and size (highlighted by the white-dashed box in Figure 2.2). The shape of these distributions, which are for midlatitude cyclonic stratiform precipitation, are similar to those seen in studies of convective precipitation (e.g., Thompson et al. 2015), indicating that raindrop-size distributions have a fundamental similarity regardless of dynamical context. A notable difference from the

[1] The corresponding rain rate bins for a given N_w and D_o between Figs. 2.2c,d may differ slightly because 1) the bins contain different samples of N_w and D_o; and 2) the Parsivel and tipping bucket gauges estimate slightly different rain rates.

convective studies is that the stratiform precipitation analyzed here over 3 h samples has fewer outliers than in the 1 min interval statistics of convective rain (Thompson et al. 2015).

Much of the contrast between Fishery and Prairie Creek is in the outliers of the distributions. The Prairie Creek distribution is shifted due to heavier precipitation rates such that there are more bins to the right of the stair-step diagonal line for Prairie Creek in Figure 2.2. Especially notable is that rain rates > 10 mm h^{-1} were much more common at Prairie Creek than at Fishery. These periods of greater rainfall, especially those exceeding 15 mm h^{-1}, were associated with landslides, road washouts, and rapid increases in the level of Lake Quinault.[2] The DSDs for rain rates > 10 mm h^{-1} at Prairie Creek were highly variable, sometimes favoring higher N_w, larger D_o, or both, relative to the most frequent DSD.

The remainder of this section examines the N_w-D_o distribution at Prairie Creek, the rainier site located at mid-elevation on the windward slope of the Olympic Mountains. Figure 2.3 shows Prairie Creek DSDs with the bins color-coded by the difference in average precipitation rate between Prairie Creek and four ground sites with blue-shaded areas denoting DSDs where Prairie Creek had more precipitation than the comparison site and red boxes where Prairie Creek had less. Figure 2.4 shows the Prairie Creek DSDs with the bins color-coded by synoptic environment parameters derived from the NARR reanalysis data: (a) average melting level, (b) integrated water vapor transport (IVT), (c) 925 hPa wind speed, (d) 925 hPa wind direction, (e) dry Brunt Väisälä frequency, N_d^2, and (f) moist Brunt Väisälä frequency, N_m^2. Other variables were tested, but, consistent with Neiman et al. (2002), we found that temperature, low-level flow, and static stability were the factors most strongly related to precipitation processes affected by topography. In the following subsections, we organize the discussion of these figures around four regimes in N_w-D_o

[2] Lake Quinault is a natural lake on the lower Quinault River.

space: most frequent DSDs, small-drop dominated DSDs, large-drop dominated DSDs, and DSDs in the heaviest rain events.

2.4.1 *The most frequently occurring distributions (moderate N_w and D_o)*

The most frequent drop-size regime (box outlined by white dashes in the middle of Figures 2.2, 2.3, and 2.4) is where D_o ranges from 1.0 to 1.6 mm and N_w ranges from 3.4 to 4.0 m^{-3} mm^{-1}. Figure 2.4 shows that: 1) the average melting level of this regime was 1870 m, slightly below the average melting level of 1920 m observed for the full sample; 2) the IVT was 250–300 kg m^{-1} s^{-1}; 3) the 925 hPa wind speed averaged 15 m s^{-1}, generally from the south; and 4) both N_d^2 and N_m^2 were greater than zero, indicating statically stable conditions upstream. Despite modest IVT, none of the other environmental parameters are especially favorable for low-level enhancement on the southwest side of the Olympic Mountains, consistent with the modest enhancement between Fishery and Prairie Creek, which lie in the southwest-facing Quinault Valley.

Figure 2.3 shows that Fishery and Graves Creek had rain rates lower than Prairie Creek in this regime. In contrast, the rain rates at the highest elevation Wynoochee site were greater than at Prairie Creek by 1.2 mm h^{-1}. All of these differences passed statistical significance testing. Wynoochee received more precipitation than any other OLYMPEX site (Figure 2.1) but was often not the highest during individual events, including the case examined in section 2.5.

2.4.2 *Distributions with large quantities of small drops (high N_w and small D_o)*

We define the regime of "large quantities of small drops" as $log_{10}N_w$ greater than 5 m^{-3} mm^{-1} and D_o less than 1 mm. Compared to the most frequent distribution, the small-drop regime has a 410 m higher melting level and 9.7 m s^{-1} weaker low-level flow from the west-southwest (Figure 2.4). These differences are statistically significant at levels of 95% or greater. The IVT is slightly

higher than the most frequent regime, but the difference is not statistically significant. The upstream flow in this small drop regime is statically stable on average.

The overall DSD in this regime (Figure 2.5) favors small drops, as seen in the non-convective, nonbrightband rain of White et al. (2003), Martner et al. (2008), and Massman et al. (2017). Following the brightband/nonbrightband algorithm from Massman et al. (2017), a vertically pointing Micro Rain Radar (MRR) at the Fishery site indicated nonbrightband rain by their criteria in 9% of the 30 minute segments within the 3 h raining periods used in this study. This nonbrightband precipitation was most frequent within the small drop regime. However, a bright band was present in 74% of 30 min periods classified as large numbers of small drops (Table 2). While a large dataset of MRR data is not available at other OLYMPEX sites, a limited sample from 1 November 2015 through 15 January 2016 at Bishop Field observed nonbrightband rain in only 21 of 366 (6%) 30-minute periods covering all DSD regimes. In a broader study encompassing four rainy seasons, White et al. (2015) also reported relatively low frequencies (14.4%) of nonbrightband rain near the Washington coast. Therefore, while nonbrightband rain may be more important in other coastal mountainous regions, it cannot be used to explain the DSD variability during stratiform steady raining periods in OLYMPEX.

Figure 2.3 shows that the average precipitation rate in the small drop regime at Prairie Creek is modestly but not significantly higher than Fishery and Bishop Field (Figure 2.3a) and significantly higher than Graves Creek, and Wynoochee (Figure 2.3b,c,d) at a 99% confidence level. The absence of large drops and the weak low-level flow suggest that this orographic enhancement pattern has weak synoptic forcing and is predominantly the consequence of condensation and rapid fallout of small drops near the front of the Olympic Mountain barrier where the flow is initially lifted.

2.4.3 *Distributions with small quantities of large drops (low N_w, large D_o)*

The regime with smaller quantities of large drops is defined by $N_w < 3$ m^{-3} mm^{-1} and $D_o > 2$ mm. Figure 2.5 shows that relative to the most frequent regime, the large drop regime has fewer drops smaller than 2 mm and more drops larger than 2.5 mm. The plots in Figure 2.4 clearly show that this regime was characterized by cold conditions, with a mean melting level of 1400 m; weak IVT averaging 200 kg m s^{-1}; light-to-moderate low-level winds, generally from the south, but occasionally from the west or northwest[3]; and frequent conditional instability (54% of 3 h periods), typically a consequence of cold air aloft. The differences between the synoptic conditions of melting level height, IVT and stability in this regime are statistically significant from those in the most frequent regime, whereas the 925 hPa wind speed and direction are not. In this low-N_w /large-D_o regime, orographic enhancement is negligible on average with no statistically significant differences in precipitation rate between the five OLYMPEX sites (Figure 2.3). The lack of moisture and the weak low-level flow evidently limited the ability of this regime to produce strong orographic enhancement, while cold processes above the bright band nevertheless generated medium- to large-sized raindrops.

2.4.4 *Distributions during heavy rain (high N_w, and large D_o)*

The highest rain rates observed at the OLYMPEX sites concentrate to the upper-right of the diagonal stair-step boundary in Figures 2.2, 2.3, and 2.4. We therefore call this part of the N_w-D_o

[3] From synoptic experience, prefrontal sectors traversing the OLYMPEX region with low melting levels generally tend to be accompanied by southerly or southeasterly flow, while in occluded fronts or colder cyclones tracking from the northwest the flow tends to be westerly or northwesterly.

diagram the *heavy rain regime*. The characteristics of the heavy rain regime include elevated values of N_w, D_o, or both, an average rain rate of 13.3 mm h^{-1}, and considerable orographic enhancement at low to middle elevations near the front of the barrier, when the Bishop Field and Prairie Creek sites often had 8-12 mm h^{-1} greater rain rates than near-coastal sites such as Fishery. The overall DSD in this regime has the same shape as the most frequent regime (Figure 2.5) but with much greater concentrations of drops of all sizes above 0.5 mm diameter.

This regime had a characteristic synoptic environment (Figure 2.4) in which the average melting level (2300 m), IVT (500 kg m s^{-1}), and 925 hPa flow (19 m s^{-1}) were all higher than in any other regime and passed statistical significance testing with the most frequent regime at 95% confidence or greater. The low-level flow direction was generally from the southwest (Figure 2.4d), matching the orientation of the Quinault Valley (Figure 2.1). The low-level static stability was close to moist-neutral with an average N_m^2 of 0.15 (Figure 2.4f) although the variance in stability is higher than the other synoptic parameters and it is not significantly different from the most frequent regime. These characteristics are consistent with previously described "atmospheric river" events. Neiman et al. (2002) found large orographic enhancement when the low-level pre-frontal jet was strong and unblocked. The environmental conditions shown in Figure 2.4 during the heavy rain regime support the conclusion of a strong correlation between low-level jet intensity and mountain precipitation made by Neiman et al. (2002). The OLYMPEX observations show that the most pronounced characteristic of the heavy rain regime is the location of the maximum precipitation enhancement at low to middle elevations near the front of the topographic barrier. The higher elevation sites near the front of the range, Wynoochee and Prairie Creek, averaged 10.7 and 13 mm h^{-1}, respectively, in the heavy rain regime, far more than Fishery's 5.4 mm h^{-1}. The even-higher elevation Snow Telemetry Site (SNOTEL) at Buckinghorse (1480 m) recorded less

precipitation than Wynoochee in 24 of 27 3 h heavy rain periods (not shown)[4]. Graves Creek and neighboring interior valley sites also had lower mean precipitation rates in this regime.

An important caveat is that Figure 2.3 and Figure 2.4 examine only the processes that contribute to precipitation at Prairie Creek. However, there were 14 3 h periods when Wynoochee, at 1020 m elevation compared to 543 m at Prairie Creek, experienced a 5 mm h^{-1} or greater precipitation rate than Prairie Creek. These periods also had above-average IVT, melting levels, and 925 hPa wind speeds. The key difference is that the 925 hPa flow direction was 28 degrees more southerly (179° vs 207°) than the periods of the heavy rain regime at Prairie Creek. All 14 of these periods were binned in the most-frequent distribution at Prairie Creek (Section 2.4.1,Figure 2.2), meaning there was minimal small drop production at Prairie Creek. It is plausible that at least some warm rain production occurred on the lower south-facing slopes during these events, but there were no low-elevation disdrometer observations during OLYMPEX on the south side of the Olympic Mountains to confirm this hypothesis.

2.4.5 *Variations in DSD regime by location*

The distributions of (N_w, D_o) in Figure 2.2a,b indicate that the four DSD regimes described above occur at different frequencies at different locations. Table 2.2 compares the frequency of occurrence and contribution to the total rainfall of each DSD regime at four of the five sites. Over 90% of the 3 h DSDs at Fishery and Graves Creek were categorized as either the "most frequent" category or the "other" category, which contains DSDs that are not classified as any of the four categories. Prairie Creek experienced a far greater variety of DSDs, especially the "heavy rain"

[4] The sample size is 27 instead of 28 in this comparison because of missing precipitation data at Wynoochee.

category that accounted for 13-14% of 3 h periods and 31-34% of the total rainfall at Bishop Field and Prairie Creek, respectively.

The contrast between the two sets of sites indicates that the modulation of precipitating frontal systems by the Olympic Mountains results in both more precipitation and a wider variety of DSDs on and near the lower windward slopes. Figure 2.6 further illustrates this concept by comparing the overall DSD at Fishery, Bishop Field and Graves Creek to the overall DSD at Prairie Creek in the different regimes. All time periods classified as a particular regime at Prairie Creek (say lots of small drops, i.e. high N_w and small D_o) was grouped together to obtain a single DSD for the small drop regime at Prairie Creek. For those same time periods, a single DSD was calculated at each of the other three sites. When Prairie Creek was in the most frequent regime, the other sites had nearly identical DSDs. When Prairie Creek was in other regimes, the DSDs at other sites tended to follow damped versions of the more extreme DSD variations in N_w-D_o coordinate space at Prairie Creek. Both the interior valley site (Graves Creek) and the upstream site (Fishery) tended to remain within the "most frequent" or "other" categories (Table 2.2) whereas Bishop Field had a more similar DSD to Prairie Creek, except when Prairie Creek was in the "large drop" regime. While it is not surprising that similar precipitation growth processes occur at the same times, the degree to which the DSDs are modulated is highly location dependent.

In the next section, results from the 12-13 November event provide further insight into the processes that contribute to the production of intense precipitation at low-to-mid elevation sites like Bishop Field and Prairie Creek in the heavy rain regime of southwesterly flow. One aspect of the DSDs that is not evident in the statistics for the whole season in Figures 2.2, 2.3, and 2.4 is the higher frequency variability of the DSDs in the heavy rain regime. The precipitation sometimes shifted toward lower concentrations of larger drops and at other times toward greater

concentrations of small- to medium-sized drops. These shifts were sometimes sudden and related to subsynoptic, mesoscale, or embedded convective processes, and are described in Section 2.5.

2.5 CASE STUDY: 12-13 NOVEMBER 2015

The analysis of three-hourly DSD statistics for the entire OLYMPEX period has identified large-scale synoptic controls on the DSDs of Pacific storms moving over the Olympic Peninsula. Analysis of the data at higher time resolution reveals sharp and sudden variations of the DSDs on subsynoptic scales. To illustrate this smaller-scale variability, we examine a warm, intense storm that would be considered an "atmospheric river" that passed over the Olympic Peninsula on the first two days of the OLYMPEX intensive observation period. Figure 2.7 shows the 36 h precipitation totals from this event. This storm was one of the major precipitation producers during OLYMPEX and caused major flooding of Lake Quinault. In contrast to the seasonal precipitation maximum at Wynoochee (Figure 2.1), the greatest amount of precipitation during this event was observed near Lake Quinault at Bishop Field and Prairie Creek. The greatest precipitation occurred on the forward slopes rather than at the highest elevations, which is typical of larger mountain ranges, such as the European Alps (Frei and Schär 1998). Like most Pacific cyclone passages, this storm consisted of several distinct storm sectors (Figure 1.1). All four of the DSD regimes described in the previous section were observed. Shifts in DSD regimes often occurred not only when the storm sectors transitioned, but also in response to smaller-scale variations of the internal storm structure.

2.5.1 *Synoptic overview*

Figure 2.8 shows NARR reanalysis plots of the melting level and IVT at three times: 2100 UTC 12 November (prefrontal sector), 1200 UTC 13 November (warm sector), and 0000 UTC 14

November (frontal sector). Soundings taken at NPOL and Quillayute (Figure 2.1) during the event are shown in a time-height cross-section in Figure 2.9. Environmental parameters from the NPOL soundings are listed in Table 2.3. The storm began with passage of a prefrontal sector that lasted from 1200 12 November - 0300 13 November at Prairie Creek. The sea-level pressure-gradient force had an eastward component near the Washington coast (Figure 2.8b) and the low-level winds were veering (Figure 2.9). The melting level was low compared to the region south of 40°N (Figure 2.8a). At sea level, a weak pressure trough separated a colder air mass to the north, and an elongated band of IVT > 400 kg m^{-1} s^{-1} stretched for more than 4,000 km across the Pacific Ocean Figure 2.8b). A long band of clouds (Figure 2.10a) coincided with the IVT band. Cold air remained north of the Olympic Peninsula during the entire event.

The warm sector began at 0300 UTC 13 November when soundings indicated nearly unidirectional flow from the west-southwest and a steady 0°C level just above 2500 m (Figure 2.9, Table 2.3). Cold air was well to the northwest of the Olympic Peninsula and high IVT impinged directly on the mountains from the west-southwest (Figure 2.8c,d). The warm sector was characterized by nearly unchanging large-scale synoptic conditions. However, similar to the coastal storm described by Neiman et al. (2016), smaller-scale waves along the frontal cloud band intermittently enhanced the cloud heights over the warm sector. One such wave appeared around 150°W in Figure 2.10a at 2100 UTC 12 November. By 1200 UTC 13 November (Figure 2.10b), it was at the coast and the coldest cloud tops associated with it were over the Olympic Peninsula and slightly offshore. By 1600 UTC 13 November, the wave passed and the cloud tops were considerably warmer on the coast and just offshore (Figure 2.10c).

After the warm sector, the frontal sector spanned the time period 1800–2300 UTC 13 November and includes the passage of a narrow cold frontal rainband (NCFR) just after 1800 UTC

13 November. This period of precipitation is not considered to be in a postfrontal sector of the type indicated in Figure 1.1 because the colder air remained to the northwest of the Peninsula until after 0000 UTC 14 November (Figure 2.8e,f). The band of IVT had weakened and shifted south, but modest IVT (> 250 kg m^{-1} s^{-1}) directed towards the windward slopes remained. A sounding launched behind the NCFR at 1802 UTC 13 November (Table 2.3, Figure 2.9) showed that the low-level flow decreased considerably but remained westerly and the melting level remained above 2500 m. By 2300 UTC 13 November, the Quillayute sounding finally shows weak cold advection behind the front (Figure 2.9).

2.5.2 *Drop-size distribution sequence*

For analysis of the 12-13 November 2015 event, the DSDs were calculated in 1-h segments. Figure 2.11 displays the sequence of 1 h DSDs from Prairie Creek for this case. Three different symbol shapes (circles, diamonds, and triangles) denote the three storm sectors (prefrontal, warm sector, and frontal, respectively). In the early part of the prefrontal period (blue circles), DSDs clustered near the most frequent DSD regime. As synoptic forcing increased with the approaching warm front aloft, the DSD shifted first toward the large drop regime (low N_w, large D_o) for three hours and finally into the heavy rain regime for the last five hours of the prefrontal sector. The warm sector is divided into two periods, indicated by yellow and red diamonds. Both are within the heavy rain regime (high N_w, large D_o), which was characterized by melting levels above 2,000 m and IVT above 500 kg m^{-1} s^{-1} (Figure 2.4). During the middle of the warm sector period (1000-1400 UTC 13 November, red diamonds), the DSD shifted toward a contribution from larger drops. The frontal sector (orange triangles) begins with 1 h in the most frequent regime followed by 3 h in the small drop regime (high N_w, small D_o). These shifts in the DSD are associated with changes

in synoptic and mesoscale environmental conditions, which change with storm sectors (Figure 1.1) and will be elaborated in the following subsections.

2.5.3 *Prefrontal period (1200 UTC 12 November–0300 UTC 13 November)*

The prefrontal sector for this case had characteristics consistent with descriptions of the early sector or pre-warm frontal passages in prior studies (Locatelli and Hobbs 1987, Medina et al. 2007). During the passage of this sector, southerly component winds at low levels veered with height, and the melting level rose significantly, as indicated by the soundings launched from the NPOL site at 1458, 1805, and 2110 UTC 12 November (Figure 2.9, Table 2.3). The 30-min rain rates at the five ground sites shown in Figure 2.12a gradually increased with similar rates at all sites prior to 2200 UTC 12 November. In order to illustrate the small-scale variability of the DSD during the 12–13 November storm, the DSDs at Prairie Creek are calculated at 5 min resolution (Figure 2.12b,c). During the passage of the prefrontal sector these DSDs consisted of small quantities of both larger and smaller drops, especially prior to 1900 UTC 12 November (Figure 2.12b). Figure 2.12c shows the contribution to the rain rate from each of the Prairie Creek Parsivel drop-size bins, with the total bar representing the 5 min rain rate estimated by the Parsivel. The light precipitation rates, weak orographic enhancement, and low concentrations of both small and large drops prior to 1900 UTC were all characteristics of the most frequent DSD regime (Section 2.4.1). During the period from 1900–2200 UTC 12 November, the DSD briefly shifted toward the large drop (low N_w, large D_o) regime. Figure 2.12c shows that most of the rainfall came from the larger drops (yellow-brown colors) during this 3 h period, but the overall rain rate remained below 8 mm h^{-1} at all five stations (Figure 2.12a). This period is consistent with the lack of

precipitation enhancement described for the large drop (low N_w, high D_o) regime (Section 2.4.3, Figure 2.3).

A sudden large change in the prefrontal DSD occurred at 2200 UTC 12 November when the DSD shifted to the high N_w, large D_o heavy rain regime and remained in that state for the remainder of the passage of the prefrontal sector (2200 UTC 12 November to 0300 UTC 13 November, cluster of blue circles in the heavy rain regime in Figure 2.11). This change is probably related to the increase of low-level flow associated with the arriving warm front. During this period, the melting level rose 400 m to nearly 2,600 m and the 925 hPa wind direction shifted to the southwest (Table 2.3). The Prairie Creek DSD shows high concentrations of drops of all sizes during this time period with a rapid increase in numbers of small drops (Figure 2.12b). During this time period, the precipitation rate at Prairie Creek (and to a lesser extent Bishop Field) increased to over 20 mm h^{-1}, while other sites remained below 10 mm h^{-1} (Figure 2.12a). This increase in rain rate was mostly accounted for by the increase of small- to medium-sized drops (< 2 mm), and by 0200 UTC 13 November these smaller drops contributed up to over two thirds of the total 20 mm h^{-1} rain rate at Prairie Creek (Figure 2.12c). The spike in precipitation rate at Wynoochee around 2200 UTC 12 November should be disregarded; it was caused by a chunk of snow dropping from the rim of the Pluvio into the bucket.

A vertical cross section obtained by combining NPOL and DOW radar data from this period at 2152 UTC 12 November shows several key features that help to understand the DSD variations during the passage of the prefrontal sector. The cross section (black line in Figure 2.1 and Figure 2.7) bisects the Quinault Valley to best view near-surface features and avoid low-level beam blockage near Prairie Creek. The reflectivity field in Figure 2.13a indicates a relatively deep layer

of ice particles above the bright band and nearly uniform reflectivity below the bright band[5]. An onshore-directed low-level jet exceeding 24 m s^{-1} in radial velocity (Figure 2.13b) rose from around 1-1.5 km above the surface near the coast to 2-3 km above the surface ~50 km inland. The radial velocity was directed toward the radars (down-valley) below 1 km in the Quinault Valley (Figure 2.8). Two distinct processes may have contributed to the increased concentration of larger (>2 mm drops) at Prairie Creek during this period (Figure 2.12b). The presence of enhanced reflectivity above the bright band (3-5 km elevation) indicates robust growth of ice particles at those altitudes, either due to orographic lifting of the air at mid-upper levels or, possibly, shear-generated turbulence over the Quinault Valley. The latter was indicated by increased Doppler spectrum width (not pictured), which could have been enhancing hydrometeor growth (as suggested by Houze and Medina 2005 and Medina and Houze 2015).

2.5.4 *Warm sector (0300-1800 UTC 13 November)*

After the passage of the prefrontal sector, the 0°C level rose and the low-level easterly toward-radar flow was replaced by southwesterly onshore and upslope flow. As a result, the shear-induced turbulence decreased (not shown) and the low-level flow lifting became focused directly over the low- to middle-elevation windward slopes and below the bright band. The warm sector passage began at about 0300 UTC 13 November, when the low-level temperature advection ended and the wind direction became nearly uniform with height from the west-southwest (Figure 2.9). The synoptic environment was generally uniform throughout the 15 h warm sector. During this time, the 0°C level was 2600 m ±80 m, the 925 hPa wind speed was 24 ±4 m s^{-1} and the 925 hPa wind direction was 246 ±7 degrees (see soundings from 0305, 0610, 0928, and 1632 UTC in Table 2.3,

[5] The bright band is located at a lower elevation in the Quinault Valley due to residual cold air was trapped in the valley and/or the processes described in Minder et al. (2011).

and Figure 2.9). The high melting level and strong low-level moisture advection from the west-southwest closely matches the synoptic environment described in Figure 2.4 for the high N_w and large D_o heavy rain regime.

Figure 2.11 shows that all 15 h of the warm sector passage fell along or to the right of the stair-step diagonal line, corresponding to the DSDs associated with the heaviest rain of OLYMPEX. Most of the warm sector had large quantities of small- to medium-sized drops contributing to the majority of the rain rate. However, during the 1000-1400 UTC 13 November period, the concentration of drops less than 1 mm decreased while drops greater than 2 mm reached the highest concentrations of the entire event (Figure 2.12b,c). Yet, the rain rate at Prairie Creek underwent only a modest increase during the large drop period, from 15 mm h^{-1} (0300-1000 UTC 13 November) to 17 mm h^{-1} (1000-1400 UTC 13 November). After 1400 UTC 13 November the rain rate increased further, up to 23 mm h^{-1}, when the DSDs switched back to favoring small- to medium-sized drops.

Figure 2.13c,d (1152 UTC 13 November) correspond to the larger-drop dominated period (red diamonds in Figure 2.11). During this period, the vertical cross section at 1152 UTC shows echo tops up to 8 km, a strong bright band at 2 km, and a secondary maximum in reflectivity above the melting level at 4 km (Figure 2.12c). This period coincides with the subsynoptic-scale wave perturbation discussed earlier, which was manifested by high cloud tops in the infrared satellite image in Figure 2.10b (Section 2.5.1). The deep ice layer and secondary reflectivity maximum aloft indicate that ice processes were important for precipitation growth during this period. The dynamical reason for the enhancement could have been vertical motion enhancement by a wave on the front, or some other mesoscale vertical motion perturbation superimposed on the synoptic-scale storm system. From a microphysical standpoint, the large drops observed by the Parsivel

during this time likely were formed by the melting of large aggregate snowflakes formed above the bright band and grew by collecting smaller drops formed below the bright band.

Figure 2.13e,f (1552 UTC 13 November) correspond to the period dominated by smaller drops (yellow diamonds in Figure 2.11). During this period the DOW-NPOL RHI taken at 1552 UTC shows that the bright band was above 2 km but weaker and echoes reached up to only ~4 km over the coast and ~6 km over the mountains 60 km east of NPOL. The infrared satellite image also shows a shallower cloud field at this time (Figure 2.10c) and the sounding cross-section shows drying from 550-450 hPa (Figure 2.9). Nevertheless, both velocity fields show a low-level jet (of 20-15 m s^{-1}) lifting from below 1 km near the coast up to 3-4 km over the mountains, especially during the later time period (Figure 2.13d,f). The low-level easterly flow and adjacent shear layer were not present in the warm sector. The lifting of the jet from below the bright band in the warm layer during the warm sector evidently provided the mechanism for rapid growth of small droplets through the processes of condensation and collision/coalescence.

2.5.5 *Frontal period (1800 UTC 13 November–0000 UTC 14 November)*

A NCFR passage around 1800 UTC 13 November lasted about 5 min at Prairie Creek and therefore had negligible impact on the 1 h accumulated DSDs. An NPOL sounding taken just after the NCFR passage (1805 UTC) indicated that the 0°C level was at 2.5 km and 925 hPa winds were 14 m s^{-1} from 250°. The Olympic Peninsula remained within warm, moist westerly-component flow behind the cold front, although there was a significant decrease in low-level flow speed, IVT, and the depth of the moist layer (Table 2.3, Figure 2.9). Steady precipitation continued at Prairie Creek through 2200 UTC 13 November. The DSD in Figure 2.11 was within the high N_w, small D_o small drop regime for 3 h (1900–2200 UTC 13 November). The Prairie Creek DSD (Figure 2.12b) had high concentrations of drops < 1 mm during this period and few if any drops > 1 mm.

Despite their large number concentration, these small-sized drops resulted in a low rain rate of < 5 mm h^{-1}. During this period, the DSD (Figure 2.11, Figure 2.12b) closely matched the example of nonbrightband rain in Martner et al. (2008). In the 12-13 November case, this small drop regime was not a significant contributor to the rainfall totals, although it could be significant in warm, weakly forced events of long duration.

2.6 CONCLUSIONS

Statistics of the DSDs observed in all stratiform precipitation that occurred during the season-long OLYMPEX field campaign and a case study of one strong storm have yielded the following conclusions:

- Four precipitation regimes are defined from the DSDs:
  - most frequently occurring: moderate N_w and D_o
  - less frequent: high concentrations of small drops, high N_w small D_o
  - less frequent: low concentrations of big drops, low N_w large D_o
  - heaviest rain periods: high N_w large D_o
- The most frequent DSD regime is associated with seasonally average synoptic conditions. Orographic precipitation enhancement is modest, and predominates at higher elevations.
- The heaviest rain regime had high melting level, large IVT, nearly moist-neutral stability, and strong low-level flow from the west-southwest, allowing for unimpeded lift of the flow over the topographic barrier and production of the largest rain rates at low-to-mid elevations near the front of the barrier.
- Analysis of a heavy precipitation case shows how the DSD varies with synoptic storm sectors and changes abruptly during the passage of embedded sub-synoptic structures.

Different modes of precipitation enhancement on the lower-windward slopes are summarized in Figure 2.14. This visual aid is guided by both the full cold season statistics (section 2.4) and the case study (section 2.5). It is also consistent with several other heavy rain producing cases in OLYMPEX (e.g. 16-17 November 2015 and 08-09 December 2015). The top panel (Figure 2.14a) closely corresponds to the most frequent DSD regime (section 2.4.1) and the early part of the prefrontal period of the case study (section 2.5.3). It shows a relatively deep stratiform cloud layer with primary precipitation production in the ice layer above the melting level. Relatively small concentrations of larger particles fall into a lower layer that comes from either a southerly or offshore direction that does not lift directly over the Olympic Mountains barrier. There is modest enhancement of precipitation on the low- to middle-elevation windward slopes because there is minimal generation of cloud water or small raindrops at low elevations. The DSDs are similar at all locations (Figure 2.6). Modest precipitation enhancement at higher windward elevations can occur, possibly due to midlevel flow lifting over the mountains above the lower layer.

The bottom panel (Figure 2.14b) describes the heavy rain DSD regime (section 2.4.4) and the warm sector period of the case study (section 2.5.4). During heavy rain periods onshore-directed low-level flow lifts unimpeded over the low elevation mountain slopes. Large quantities of small drops are formed by condensation and collision/coalescence above the low- to middle-elevation windward slopes. Ice-initiated drops fall from a high 0 °C level and collect some of the small drops, consistent with the process suggested by Minder et al. (2008). Deep precipitating clouds with considerable ice production are not necessary to generate heavy rainfall on the windward slopes, but can be responsible for shifts toward smaller concentrations of larger drops. Lifting of the warm, moist-neutral low-level jet is the dominant precipitation-generating process throughout the heavy rain regime. The case study analysis in section 2.5 illustrates how there can be rapid

shifts in the scenarios illustrated in Figure 2.14a,b within one storm that depend on storm sector and sub-synoptic scale variability.

The importance of warm rain processes in west coastal orographic environments was also noted in California (White et al. 2003, Kingsmill et al. 2006, Martner et al. 2008, Kingsmill et al. 2016) and in the Nahuelbuta range in Chile (Massman et al. 2017). The California studies took the approach of classifying the dominant microphysical process by using the presence of a bright band in vertically pointing radar observations. This separation is effective at isolating instances of shallow warm rain with little if any contribution from melting ice. However, it does not account for the considerable variability in precipitation microphysics that occurs when a bright band is present. During stratiform raining periods in OLYMPEX, a bright band was evident on vertically-pointing radar over 90% of the time (Table 2.2), including periods when warm-rain processes were clearly dominant (see Figure 2.13Figure 2.14). However, even during those periods, ice processes were still contributing to precipitation growth. This study demonstrates that the precipitation over the Olympic Mountains is a complex mix of warm low-level growth and ice-originated rainfall where their relative importance is modulated by synoptic and mesoscale conditions. Future studies will employ other OLYMPEX datasets such as the dual-polarization radar data, microphysical sampling from aircraft, and high-resolution modeling to further explore these precipitation processes and their modulation by synoptic environment and complex terrain.

We further note that this study has implications regarding the convective/stratiform partitioning used to characterize rainfall variability in deep convective regimes. The heavy rain and large quantities of small drops regimes described above in sections 2.4.2 and 2.4.4 fall in the same N_w-D_o space that has been associated with convective radar echoes in the tropics (Bringi et al. 2009, Thompson et al. 2015). However, this study is restricted to stratiform precipitation,

demonstrating that both convective and stratiform precipitation can exhibit the same DSDs. We therefore conclude that DSDs alone cannot in general be used to describe whether precipitation resulted from convective or stratiform processes.

A primary goal of OLYMPEX was to provide physical ground validation for the GPM satellite. Space-borne radar retrievals require a parameterized DSD to convert reflectivity to rain rate (Iguchi and Meneghini 1994), a difficult problem given the complexities of stratiform DSDs observed in this study. Sub-synoptic scale perturbations (e.g. 1000-1400 UTC 12 November 2015) can modify the vertical cloud structure and DSD without appreciably changing the underlying rain rate. Ground clutter removal algorithms must preserve as much near-surface information as possible to capture the below-bright band warm rain processes. Warm precipitation processes also present challenges for passive microwave retrievals of precipitation over land since the precipitation estimates are somewhat biased toward the mean rain rate associated with a given ice scattering signature (Kummerow et al. 2010, Kummerow et al. 2015).

2.7 TABLES AND FIGURES

Table 2.1. Description of the five OLYMPEX ground sites used in this study.

Site	Elevation (m)	Latitude	Longitude	Description	Instrument(s) Used
Fishery	52	47.36	-123.99	Windward, upstream, low-elevation	Parsivel, MRR, Tipping Buckets
Bishop Field (CRN)	85	47.54	-123.68	Windward front of valley, low-elevation	Parsivel, Tipping Buckets
Prairie Creek	543	47.51	-123.93	Windward, front of valley, middle-elevation	Parsivel, Tipping Buckets
Graves Creek	180	47.57	-123.58	Windward, interior valley, low-elevation	Parsivel, Tipping Buckets
Wynoochee	1020	47.5	-123.58	Windward, interior, high-elevation	Pluvio

Table 2.2. Frequency of occurrence (%) and contribution to the total rainfall (%) of the four DSD regimes at four ground sites. The 'other' category encompasses 3 h DSDs that fall outside of the four DSD regimes. The percentage of bright band rain is also included for 752 30 minute MRR observation periods at the Fishery site following the methodology of Massman et al. (2017).

	Fishery (204 obs)			Bishop Field (217 obs)	
Category	% of 3 h periods	% of total rainfall	% bright band	% of 3 h periods	% of total rainfall
Most Frequent	48	58	90	36	29
High N_w, Small D_o	3	2	74	6	5
Low N_w, Large D_o	2	3	92	6	3
Heavy Rain	1	1	95	13	31
Other	46	36	93	39	32

	Prairie Creek (217 obs)		Graves Creek (192 obs)	
Category	% of 3 h periods	% of total rainfall	% of 3 h periods	% of total rainfall
Most Frequent	34	27	50	52
High N_w, Small D_o	6	5	0	0
Low N_w, Large D_o	6	3	2	2
Heavy Rain	14	34	0	0
Other	40	31	47	46

Table 2.3. Synoptic environment parameters computed from the eight soundings launched at NPOL during the 12-13 November 2015 event.

Time	0 °C Level (m)	IVT (kg m^{-1} s^{-1})	925 hPa speed (m s^{-1})	925 hPa direction (deg)	950-850 hPa N_d^2(x10^{-4})	950-850 hPa N_m^2 (x10^{-4})
1458 UTC 12 Nov	1334	337	18.3	205	1.24	0.05
1805 UTC 12 Nov	1520	427	18.6	207	1.38	0.15
2110 UTC 12 Nov	2219	610	25.5	191	2.03	0.78
0305 UTC 13 Nov	2584	637	21.7	253	1.56	0.12
0610 UTC 13 Nov	2680	693	22.5	246	1.51	0.08
0928 UTC 13 Nov	2560	716	27.5	239	1.61	0.20
1632 UTC 13 Nov	2582	573	22.1	240	1.62	0.19
1802 UTC 13 Nov	2512	496	13.8	248	1.97	0.58

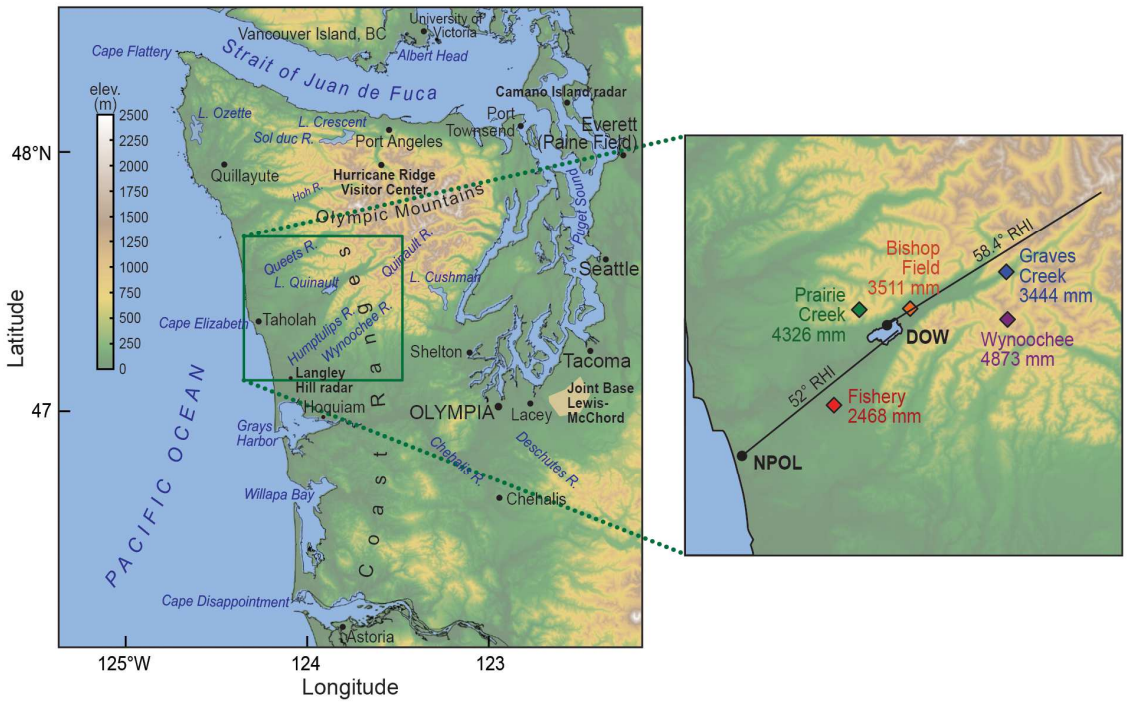

Figure 2.1: Location of OLYMPEX radars and ground sites used in this study. The black line denotes the 52° NPOL RHI and the 58.4° DOW RHI. The right panel includes the total measured precipitation from 10 October 2015 to 30 April 2016.

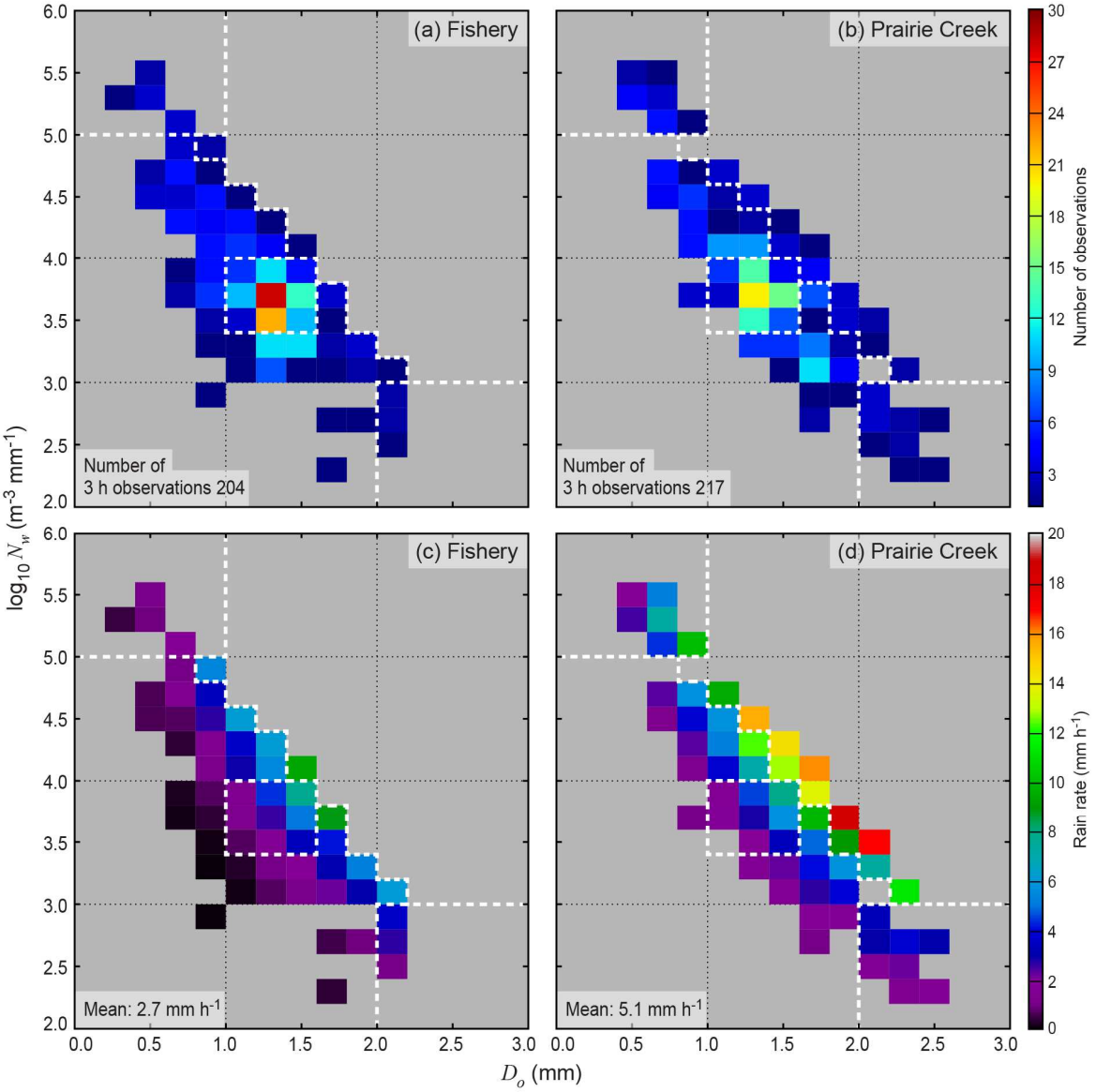

Figure 2.2: Two-dimensional histograms of 3 h drop-size distributions binned by $\log_{10}(N_w)$ and D_o at Fishery (left column) and Prairie Creek (right column). (a),(b) Number of observations in each bin. (c),(d) Average rain rate, measured by dual-tipping buckets. The dashed white lines denote the four DSD regimes: the upper left box corresponds to large quantities of small drops, the box in the middle corresponds to the most frequent regime, the lower right box corresponds to small numbers of large drops, and the region to the right of the diagonal stair-step line corresponds to the heavy rain regime.

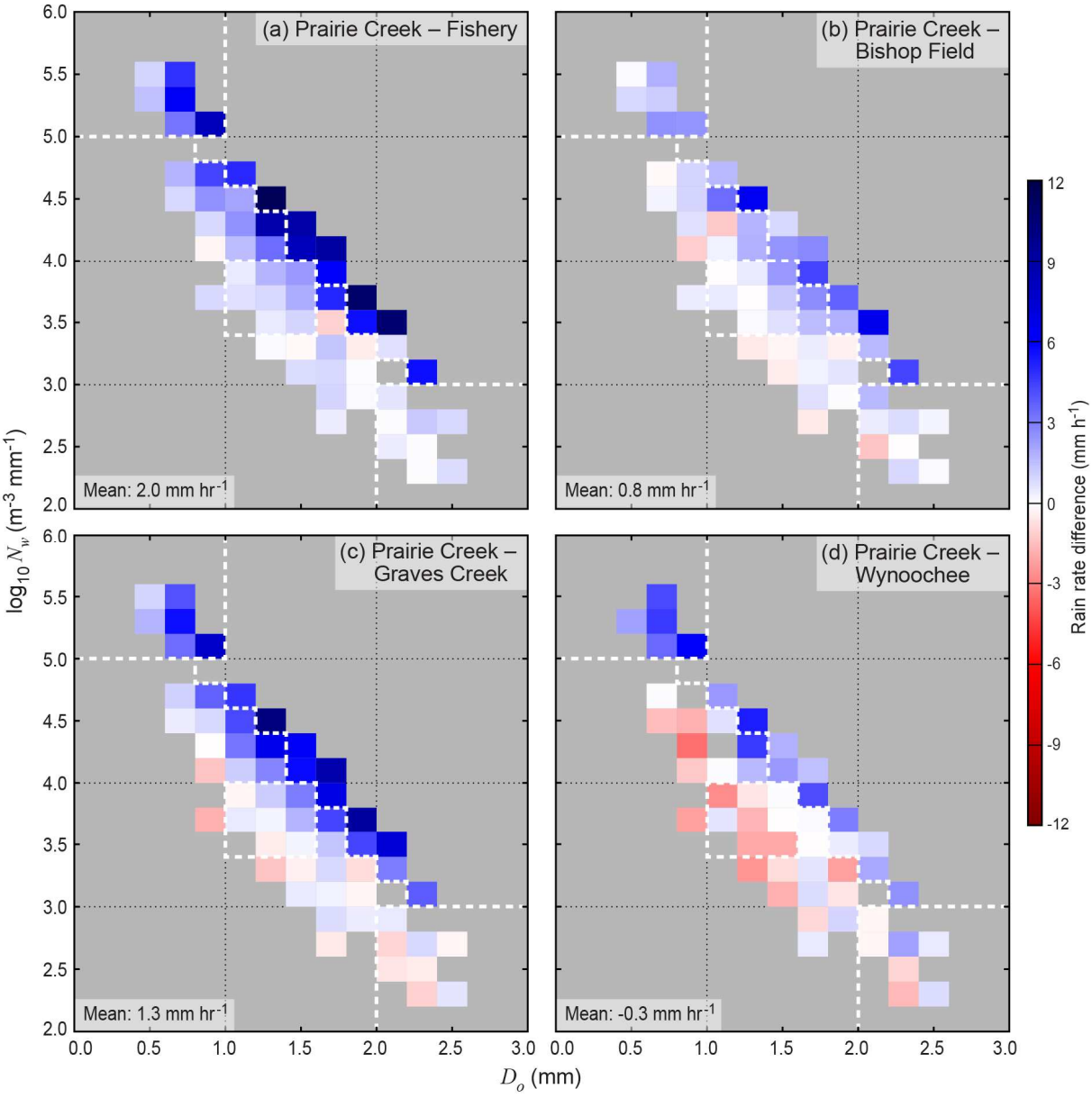

Figure 2.3: Difference in precipitation rate measured by precipitation gauges (dual tipping buckets or Pluvio weighted bucket) between Prairie Creek and the four other ground sites. The data are binned by the Prairie Creek 3 h drop-size distribution as in Fig. 2.2b. The white dashed lines are as in Figure 2.2.

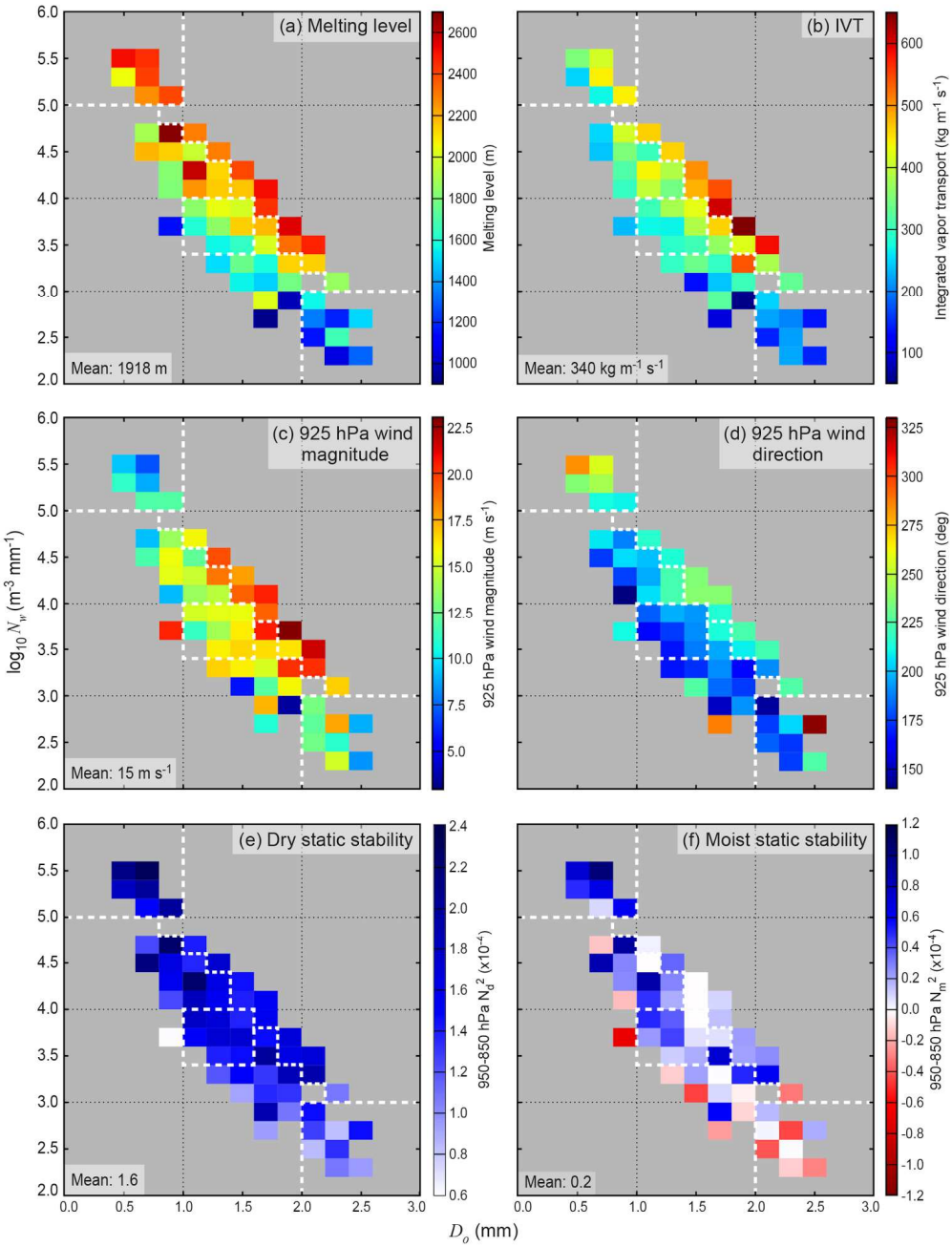

Figure 2.4: As in Figure 2.3 except for synoptic environmental parameters calculated at the NARR grid point closest to NPOL. (a) Melting Level (m), (b) Integrated Vapor Transport (IVT, kg m^{-1} s^{-1}), (c) 925 hPa wind speed (m s^{-1}), (d) 925 hPa wind direction (degrees), (e) Dry Brunt-Väisälä Frequency (N_d^2), (f) Moist Brunt-Väisälä Frequency (N_m^2). The white dashed lines are as in Figure 2.2.

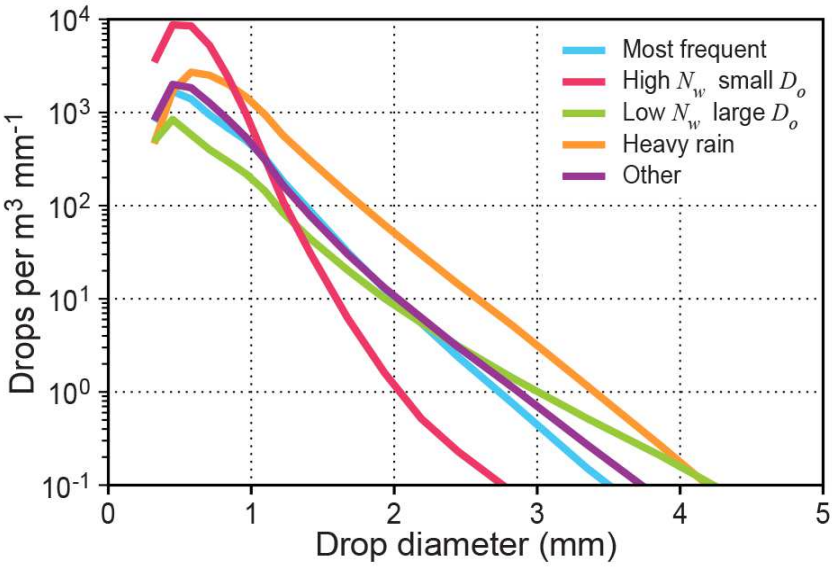

Figure 2.5: Overall DSDs at Prairie Creek for each of the four DSD regimes described in Section 2.4 of the text and the unclassified “other” category.

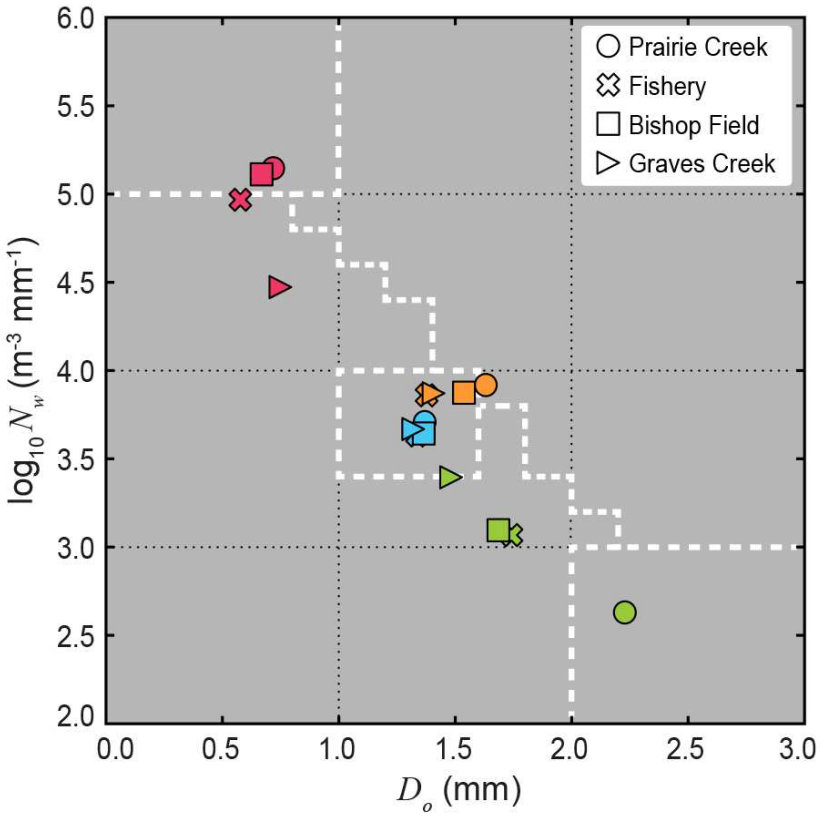

Figure 2.6: Scatterplot of the overall D_o vs. $\log_{10}(N_w)$ relationship for four of the ground sites. Each point represents the combined DSD for the times that Prairie Creek falls into each of the four DSD regimes. The colors correspond to the regimes in Figure 2.5: most frequent (blue), small drops (red), large drops (green), and heavy rain (orange).

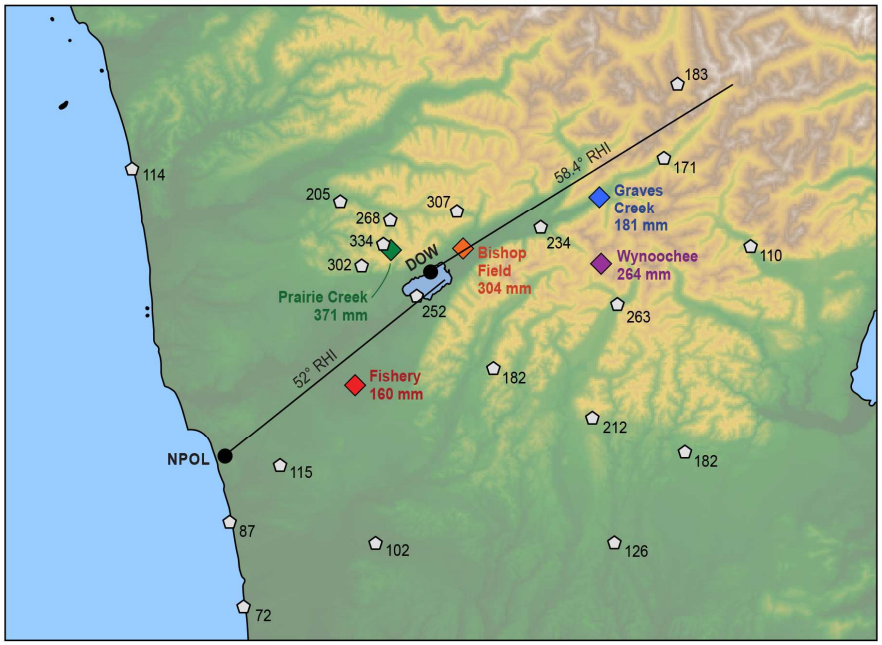

Figure 2.7: Precipitation totals for the 12-13 November 2015 case study for the sites labeled in Figure 2.1 and additional locations from OLYMPEX gauges and other sources including Remote Automated Weather Stations (RAWS) and Snow Telemetry (SNOTEL).

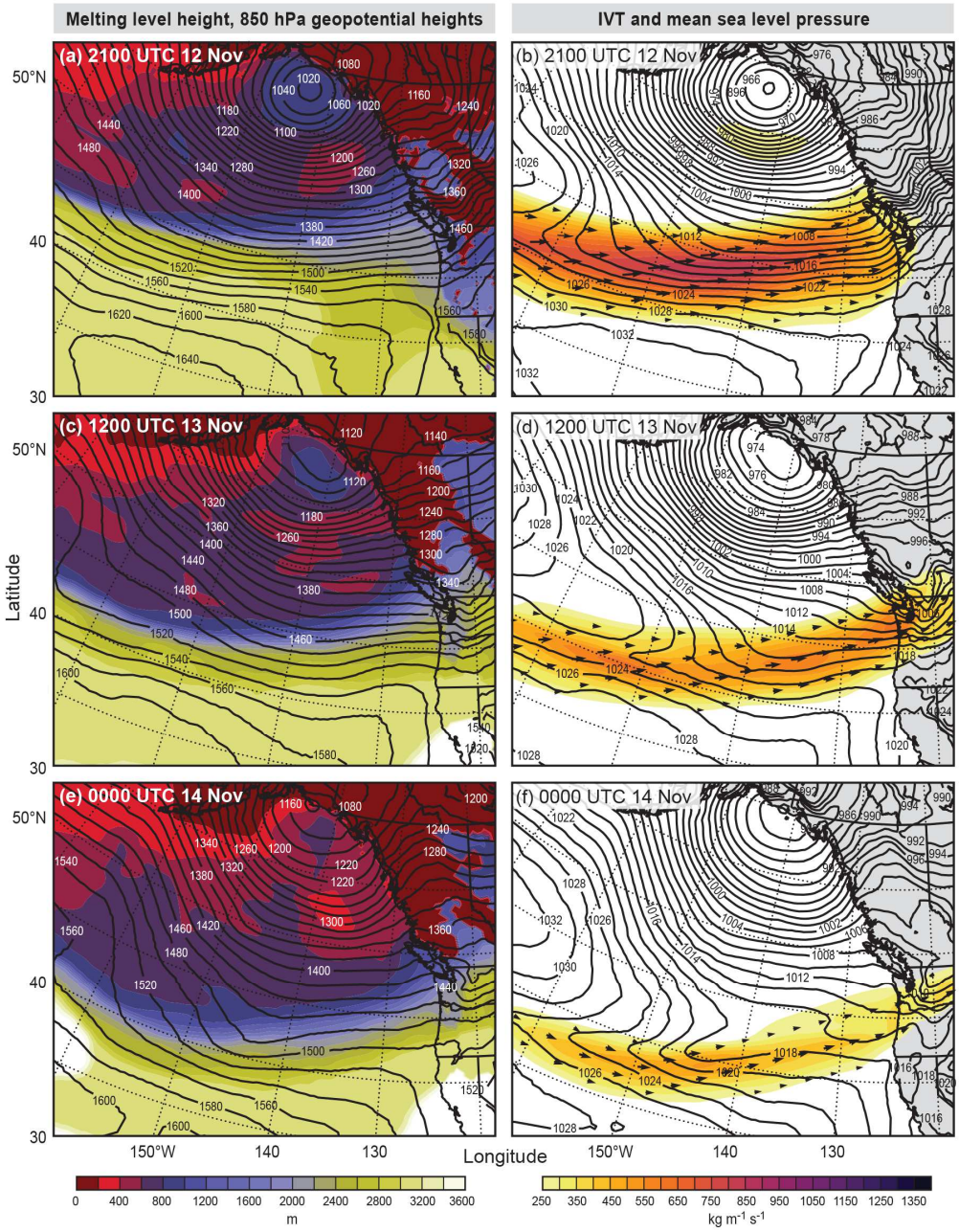

Figure 2.8: NARR reanalysis maps showing the synoptic setup of the 12-13 November 2015 case study at three times: (a,b) 2100 UTC 12 November 2015, (c,d) 1200 UTC 13 November 2015, (e,f) 0000 UTC 14 November 2015. The left column shows melting level height (colors) and 850 hPa geopotential heights (contours). The right column shows integrated vapor transport (colors and vectors) and sea level pressure (contours).

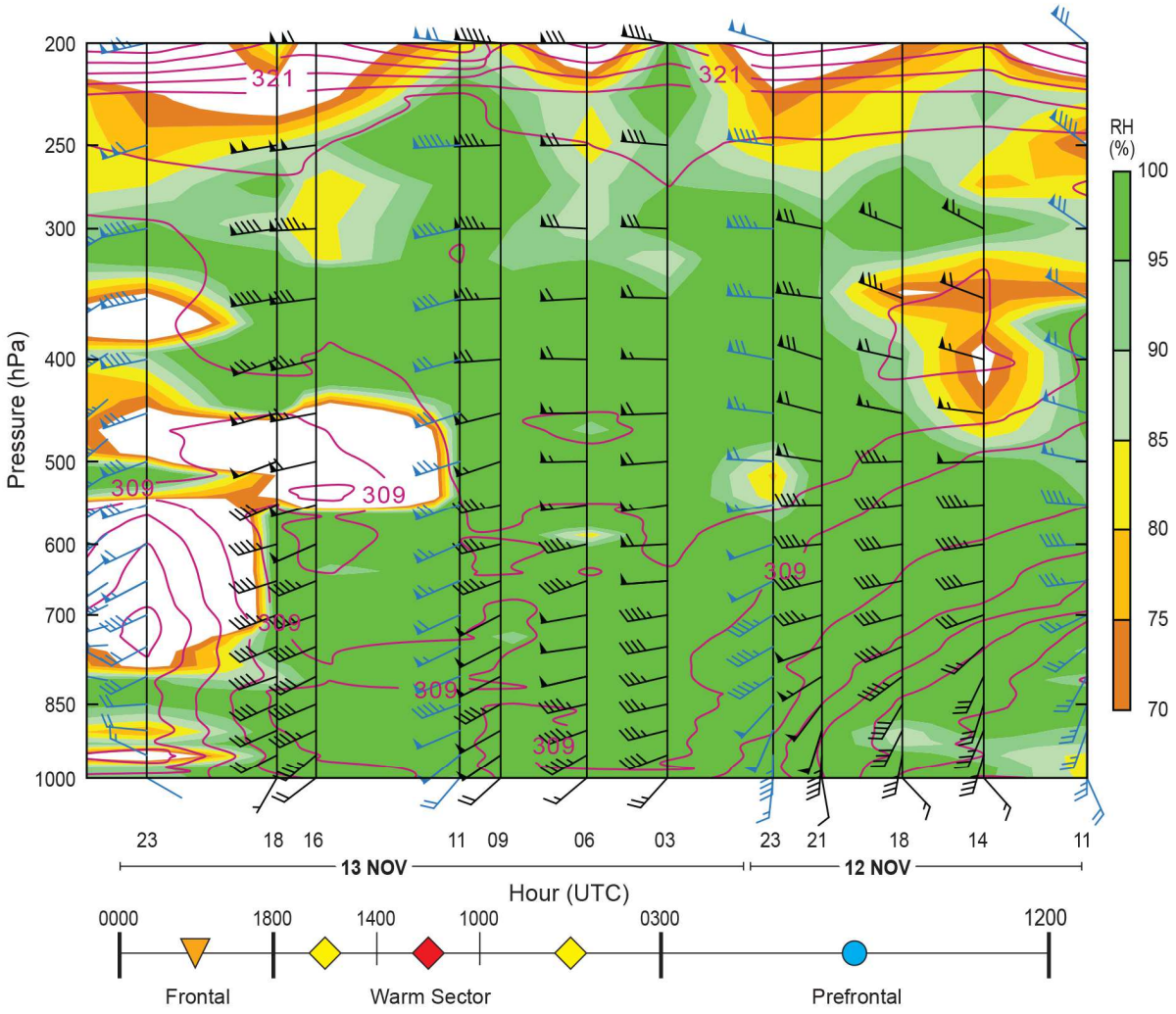

Figure 2.9: Time-height cross-section of soundings launched during the 12-13 November 2015 case study. Black lines and wind barbs (kt) denote soundings launched from NPOL. Blue lines and wind barbs (kt) denote soundings launched from Quillayute (Figure 2.1). Red contours denote potential temperature (θ). Colored contours denote relative humidity (%). Figure provided by Dr. Paul Ciesielski.

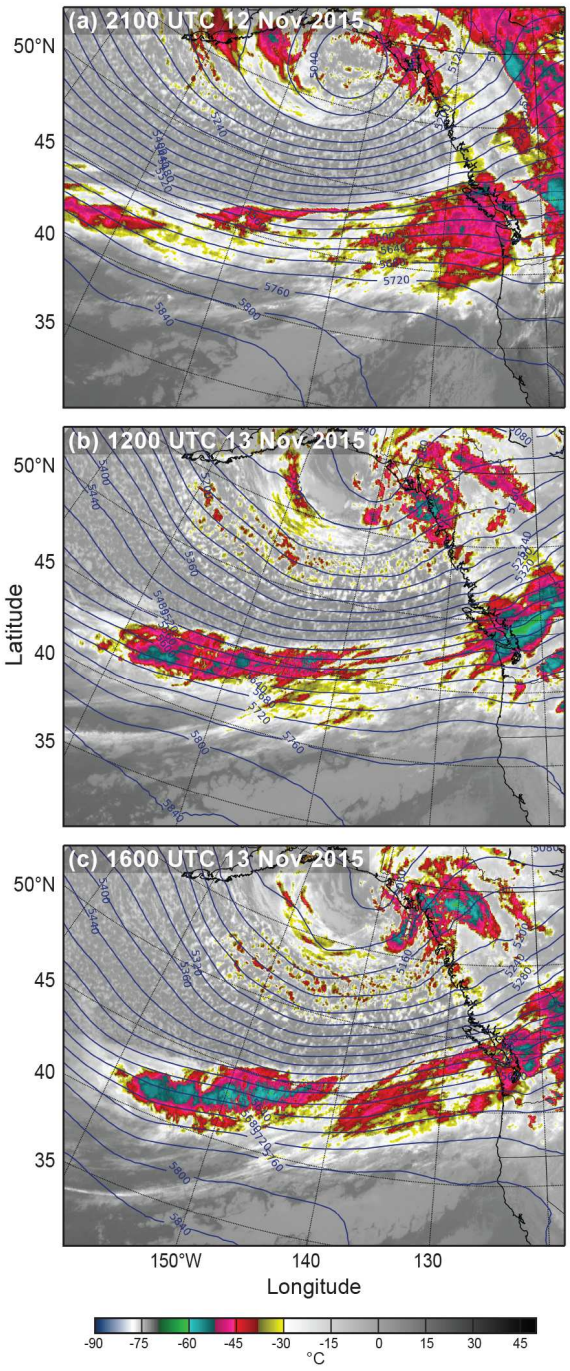

Figure 2.10: GOES-West infrared satellite imagery and NARR 500 hPa geopotential heights (contours) for (a) 2100 UTC 12 November 2015, (b) 1200 UTC 13 November 2015, (c) 1600 UTC 13 November 2015.

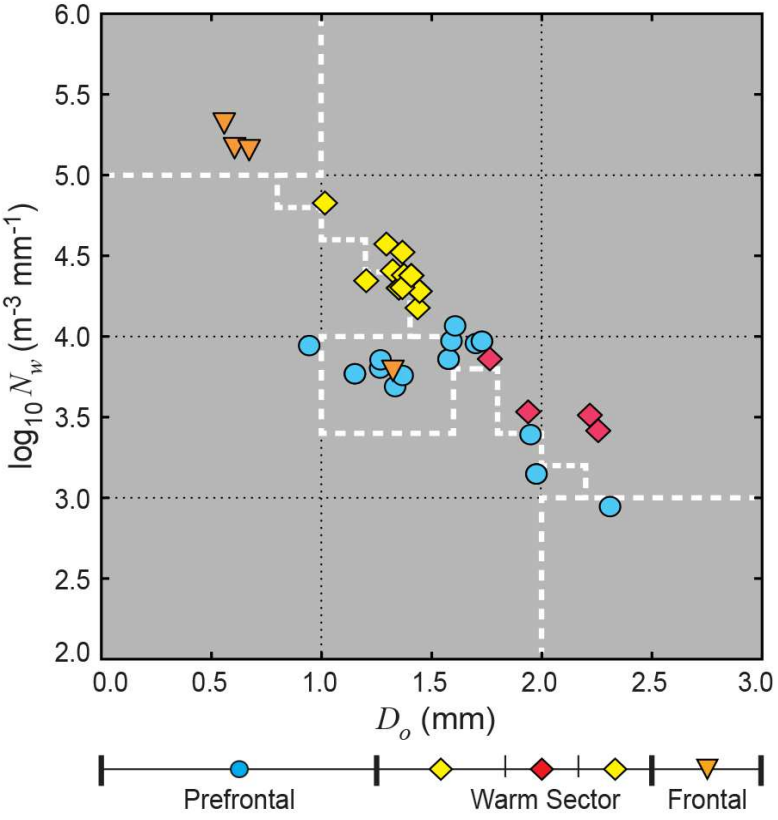

Figure 2.11: Scatterplot of the D_o vs. $\log_{10}(N_w)$ relationship for 1 h periods at Prairie Creek during the 12-13 November 2015 case study. Symbol shapes denote the prefrontal (circles), warm sector (diamonds) and frontal (triangles) periods. Symbol colors denote the four major periods described in the text.

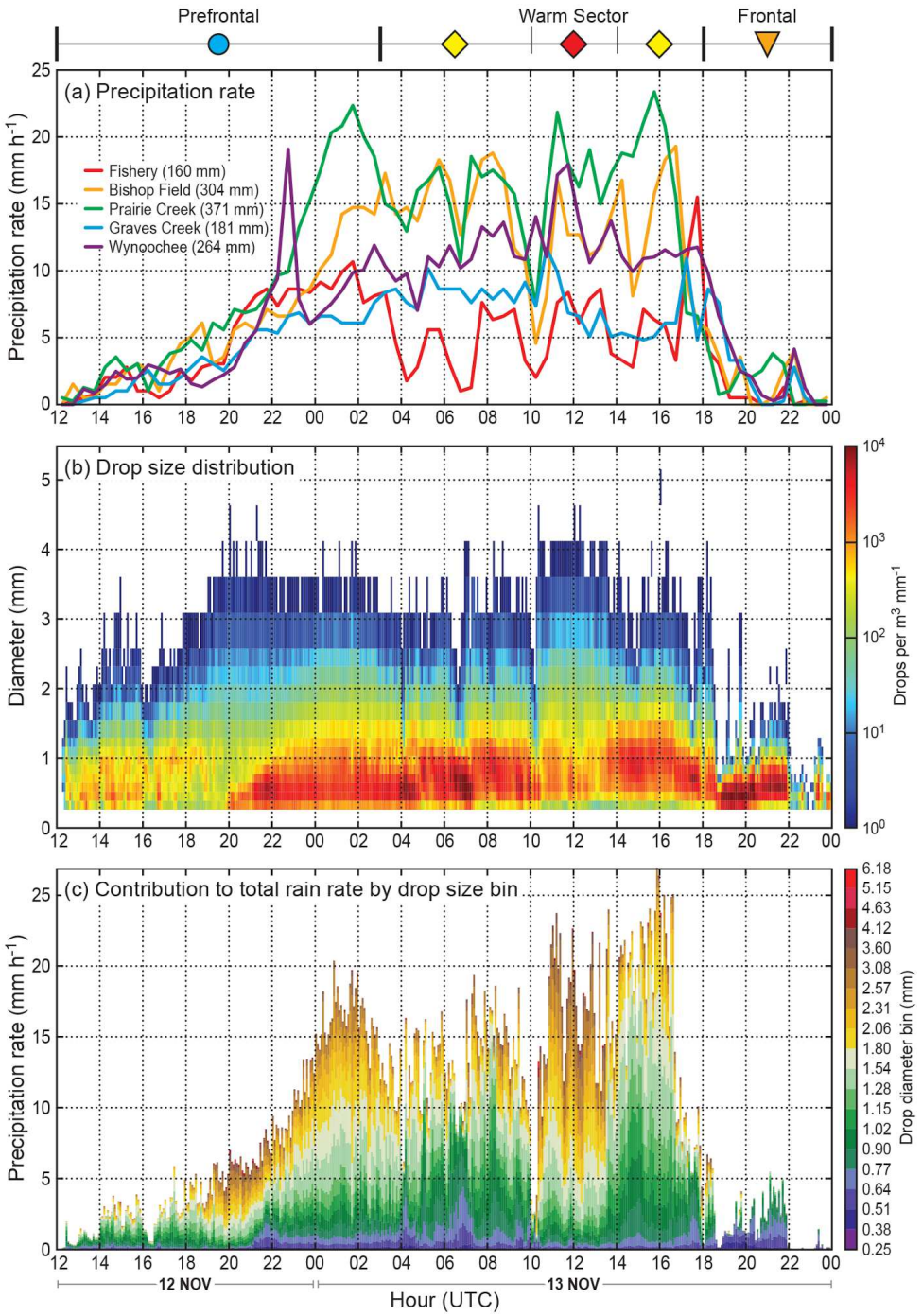

Figure 2.12: Time series of ground instrument data during the 12-13 November 2015 case study. The symbols at the top match the time periods diagrammed in Figure 2.9. (a) 30 min precipitation rate at the five ground sites. (b) 5 min Prairie Creek drop-size distribution. (c) 5 min contribution to the total rain rate by Parsivel drop-size bin at Prairie Creek. The spike in precipitation rate at Wynoochee at in panel (a) at 2230 UTC 12 November was caused by a chunk of snow dropping into the Pluvio bucket.

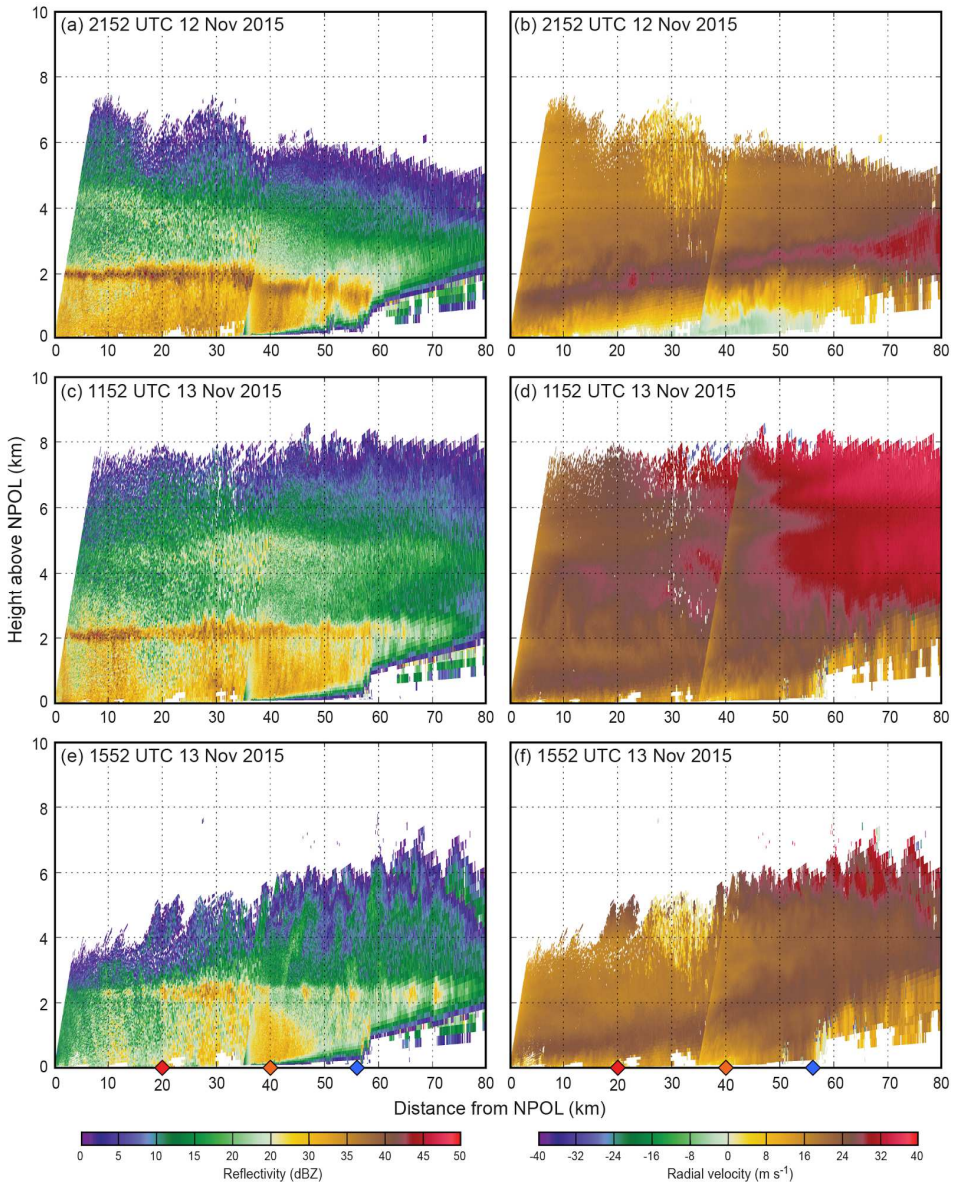

Figure 2.13: Combined NPOL-DOW cross-section images of reflectivity (a,c,e) and radial velocity (b,d,f) for (a,b) 2152 UTC 12 November, (c,d) 1152 UTC 13 November, and (e,f) 1552 UTC 13 November. The location of the cross-section is shown in Figure 2.1 and Figure 2.7. The NPOL radar was 139 m above sea level. The diamonds on the x-axis indicate the location of three ground sites along the cross-section: Fishery (red diamond, 20 km from NPOL), Bishop Field (orange diamond, 40 km from NPOL), and Graves Creek (blue diamond, 58 km from NPOL). The DOW was 35 km from NPOL. The Py-ART Python module (Helmus and Collis 2016) provided software for radar plotting.

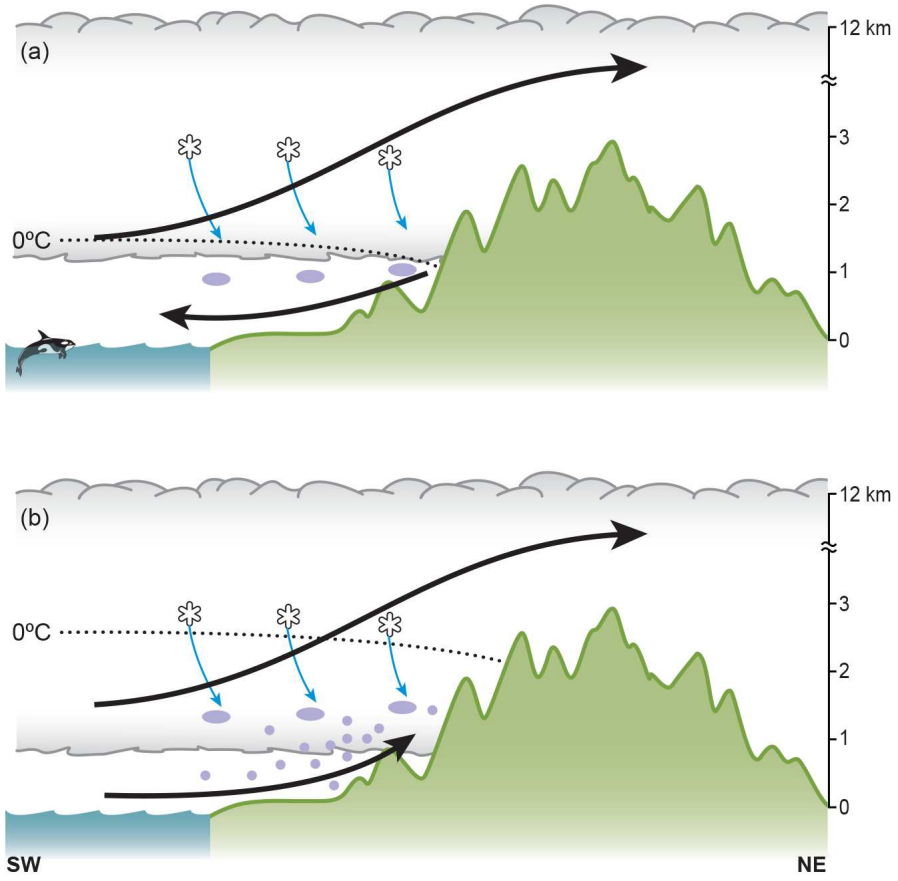

Figure 2.14: Visual aid depicting the two primary modes of precipitation enhancement as extratropical cyclones move from the Olympic Coast Marine Sanctuary to the Olympic Mountains for (a) minimal precipitation enhancement on the lower-windward slopes and (b) considerable enhancement of precipitation on the lower-windward slopes. The NASA ER-2 aircraft provided cloud top height estimates. Terminal aerodrome forecasts (TAFs) from Hoquiam, WA (Figure 2.1) provided cloud base estimates. Black arrows represent the low- and midlevel flow directions. Ellipses represent large raindrops formed from melted ice particles. Circles represent small raindrops formed by condensation and collision/coalescence.

Chapter 3. VERTICAL STRUCTURE AND MICROPHYSICAL PROCESSES OF FRONTAL SYSTEMS PASSING OVER A THREE-DIMENSIONAL COASTAL MOUNTAIN RANGE

3.1 ABSTRACT

This chapter constitutes one of the first studies to examine precipitation mechanisms in the lee as well as the windward side of a mountain range. As mid-latitude cyclones pass over a coastal mountain range, the processes producing their clouds and precipitation are modified, leading to considerable spatial variability in precipitation amount and composition. Statistical diagrams of airborne precipitation radar transects and surface precipitation and particle size measurements are examined from nine cases observed during the Olympic Mountains Experiment (OLYMPEX). Although the pattern of windward enhancement and leeside diminishment of precipitation was omnipresent, the degree of modulation was largely controlled by the synoptic environment, varying across the prefrontal, warm, and postfrontal sectors of mid-latitude cyclones. Prefrontal sectors contained homogeneous stratiform precipitation with a slightly enhanced ice layer on the windward slopes with a near-complete rain shadow in the lee. Warm sectors contained deep, intense enhancement over both the windward slopes and high terrain and less prominent rain shadows owing to downstream spillover of ice particles generated over terrain. Surface particle-size distributions in the warm sector contained a broad spectrum of sizes and concentrations of raindrops on the lower windward side where high precipitation rates were achieved from varying degrees of both liquid and ice precipitation-generating processes. Spillover precipitation was rather

homogeneous in nature and lacked the variations in particle size and concentration that occurred at the windward sites. Postfrontal precipitation transitioned from isolated convective cells over the ocean to a shallow, mixed convective-stratiform composition with broader coverage and greater precipitation rates over the sloping terrain.

3.2 INTRODUCTION

Precipitation over midlatitude west coastal mountain ranges is usually associated with baroclinic frontal cyclones containing distinct cloud patterns, which are modified during passage over complex terrain (Nagle and Serebreny 1962; Medina et al. 2007). Observations from numerous past field programs have characterized the complex ways in which warm processes (condensation/collision–coalescence) and cold processes (riming, accretion, and aggregation) contribute to the modification of precipitation processes over west coastal mountains (e.g., Hobbs et al. 1971; Houze et al. 1976; Hobbs 1978; Matejka et al. 1980; Bond et al. 1997; Ralph et al. 1999; Stoelinga et al. 2003; Houze and Medina 2005; Anders et al. 2007; Medina et al. 2007; Minder et al. 2008, Barrett et al. 2009; Viale et al. 2013; Massmann et al. 2017; Zagrodnik et al. 2018). Ground-based scanning radars have been especially valuable in determining the specific processes that lead to modification of precipitation but have tended to emphasize the windward side because of the hydrologic impacts caused by heavy precipitation. Models are able to simulate the diminishing precipitation over the high terrain and in regions of leeside descent (e.g. Colle 2004, Zängl 2005, Picard and Mass 2017). However, model accuracy is difficult to evaluate because of a dearth of observations of high terrain and leeside precipitation processes. Surface and radar observations made from ground sites near mountain ranges are often limited by inaccessibility, terrain blockage, and beam widening.

In order to better understand the mechanisms controlling the precipitation all of the way across a mid-latitude coastal mountain ranges, the 2015-16 Olympic Mountains Experiment (OLYMPEX, Houze et al. 2017) deployed numerous observational resources across the windward, interior, and lee sides of the Olympic Mountains, where the climatological windward side experiences thousands of millimeters of precipitation and the lee side is very dry (Figure 3.1). In a recent study using OLYMPEX data, Purnell and Kirshbaum (2018), hereafter PK18, used rain gauges and operational National Weather Service radars to show that orographic precipitation distributions are highly sensitive to the upstream static stability, horizontal moisture flux, and the presence of pre-existing precipitation associated with the large-scale synoptic storm sectors. McMurdie et al. (2018) found that when the large-scale conditions resembled warm sectors (moist-neutral upstream stability combined with high horizontal water vapor flux), the precipitating cloud over terrain was enhanced in the ice layer of the precipitating system. Chapter 1 (Zagrodnik et al. 2018) showed that the periods of heaviest rainfall on the windward slopes often contained large concentrations of small drops, suggesting that warm precipitation processes are dominant during the strongest terrain-induced enhancement. Based on quasi-idealized model simulations, PK18 argued that at least some pre-existing precipitation was required to fully realize the observed windward-side precipitation enhancement. However, it remains unclear how windward-side precipitation enhancement rates are controlled by the simultaneous variability of both warm and ice precipitation processes.

Precipitation reaching the lee side can be modified by synoptic and dynamic mechanisms associated with frontal cyclones. Mass et al. (2015) and Siler et al. (2016) investigated the reasons for weak and strong rain shadows in the lee of the quasi-linear (two dimensional), north-south oriented Washington Cascades. From a synoptic viewpoint, both studies showed that weaker rain

shadows on the eastern slopes were favored in the prefrontal (warm frontal) periods of midlatitude cyclone passages, prior to the erosion of the preexisting stable air mass in the lee. Siler et al. (2016) found that weaker rain shadows were associated with muted lee wave activity, a consequence of low-level cold, stagnant air disfavoring descent in the lee. Mass et al. (2015) suggested a different mechanism for weak rain shadow scenarios: southeasterly upslope flow on the eastern slopes induced by the approaching frontal trough. In contrast, PK18 found the strongest rain shadows in prefrontal periods over the circular, quasi-dome-shaped (three-dimensional) Olympic Mountains due to strong leeside mountain-wave descent favored by a statically stable upstream environment. Cold, stagnant air in the lee of a dome-shaped mountain range is more easily eroded by low-level air flowing around the barrier (Mass and Ferber 1990, Colle and Mass 1996), possibly explaining the difference in leeside behavior in the two types of mountain ranges. In addition to dynamical effects, liquid and ice-phase microphysical growth rates may determine if particles grow fast enough to fall out on the windward side or are advected to the lee side (Hobbs et al. 1973).

Surface disdrometer and airborne radar observations from OLYMPEX offer an opportunity to carefully examine the microphysical processes associated with the modification of precipitation over full transects of a coastal dome-shaped mountain range. These observations form the foundation of this study, which addresses the following two questions:

1) What large-scale environmental and microphysical processes control the enhancement of precipitation on the windward side and the diminishment of precipitation on the high terrain and lee side of a three-dimensional coastal mountain range?

2) How does the composition, size, and concentration of liquid and frozen precipitation particles vary as a function of the enhancement and diminishment characteristics?

3.3 DATA

This study uses several observational assets including precipitation rate and particle size distributions from ground-based instrumentation, and airborne radar data collected during nine separate flight missions during OLYMPEX (Petersen et al. 2018). Details of each of these platforms are described below.

3.3.1 *Airborne Precipitation and Cloud Radar Third Generation (APR-3)*

The onboard instruments of the National Aeronautics and Space Administration (NASA) DC-8 aircraft used in OLYMPEX simulated the measurements that are made aboard the GPM satellite (Skofronick-Jackson et al. 2017), including the Airborne Precipitation and Cloud Radar Third Generation (APR-3). The DC-8 flew at altitudes of 10–11 km with the APR-3 obtaining measurements of reflectivity at Ku- (13.4 GHz), Ka- (35.6 GHz) and W- (94.9 GHz) bands. The antenna scanned cross-track ±25° with 30 m range sampling. The Ku-band radar reflectivity factor is used in this study as it is sufficient to capture the salient features of the storm structure and occurrence of precipitation. The footprint was approximately 0.8 km for a 10 km flight altitude. The sensitivity of the Ku-band is 0 dBZ and the calibration uncertainty is 1 dB at 5 km distance and the calibration uncertainty is ±1.5 dB. To mitigate the effects of aircraft roll, only the beam closest to nadir in each scan is used in this study.

The original APR-3 data obtained from the Distributed Active Archive Centers (DAAC, Durden and Tanelli 2018) were further processed by first cleaning the data and removing all of the ground clutter while retaining as much near-surface data as possible. In the current version of the Ku reflectivity product, isolated spikes of 10-15 dBZ reflectivity within broader regions of weak reflectivity frequently affect low signal-to-noise (SNR) regions. A 2D gaussian filter with a standard deviation of 1.5 bins (Randy Chase, personal communication 2018) effectively removed

the speckling without degrading the reflectivity information, as seen in the example transects provided in section 3.4. We also removed all Ku data where the cleaner and more sensitive Ka-band reflectivity is less than 0 dBZ.

The surface clutter removal involves several steps. Over regions of steep terrain, the radar beam partially intersects the land surface, leading to considerable variation in the number of bins with clutter above the estimated surface height. When the radar bright band intersects with terrain it often mimics the decrease in reflectivity with height associated with ground clutter. Because of these complicating factors, we first generated an *a priori* estimate of the lowest clutter-free bin in each APR-3 profile using a surface roughness parameter defined by the standard deviation of the top of strongest ground clutter (> 50 dBZ) associated with the ground surface over a 5-footprint moving range in the horizontal. Our algorithm then removes the region above the APR-3 surface flag with decreasing reflectivity with height (< -0.1 dB per bin) within the height window predicted by the surface roughness estimate. At least 10 bins (300 m) are removed from every profile with up to 20 bins (600 m) removed in steep mountainous terrain. Visual inspection of all flight legs confirms the effectiveness of this method at removing all clutter, although it does occasionally remove a few more bins than necessary to safely ensure that all surface clutter is removed.

The accepted reflectivity data was compiled into two types of diagrams: Contoured Frequency by Altitude Diagrams (CFADs; Yuter and Houze 1995) and gridded maps of reflectivity height and coverage. The CFADs were constructed by binning the quality-controlled Ku reflectivity data into two-dimensional histograms of reflectivity from 0-50 dBZ in 1 dB intervals between heights above sea level of 1.5 and 8.0 km in 0.25 km intervals. Each CFAD is normalized by the maximum bin at any level after correcting the sample size for terrain obstruction at lower levels. The terrain correction primarily affects the four lowest bins (1.5-2.5 km) in the high terrain region, where the

ground clutter obstructs 77%, 57%, 46%, and 16% of the sample, respectively. The resultant CFADs have values ranging from 0% to 100% at each 0.25 km height interval. Difference CFADs were also generated by subtracting the ocean CFAD from the coast, windward, high terrain, and lee side CFADs. Compared with the normalization-by-level methodology employed in McMurdie et al. (2018) where each height level is an independent sample, normalizing by the overall maximum bin allows for examination of the relative difference in frequency between various heights. The CFAD heights are relative to sea level and are not adjusted for bright band height.

In addition to the CFADs, gridded maps of Ku 15 dBZ echo top height and frequency are included to supplement the CFADs by providing a more detailed spatial context of the average height and coverage of precipitating clouds using a threshold equivalent to the ~15 dBZ Ku minimum sensitivity of the Dual frequency Precipitation Radar onboard the GPM core satellite. The gridded maps were constructed in two steps. First, for each vertical profile from APR-3 within a particular 0.2 longitude x 0.2° latitude box, it was determined whether there were Ku echoes greater than 15 dBZ anywhere within that profile. If maximum reflectivity was greater than 15 dBZ, then the highest 15 dBZ bin height was recorded. After all the vertical profiles were processed, the average height of the highest 15 dBZ echo and the percent coverage of vertical profiles containing at least one 15 dBZ echo were calculated for each 0.2° by 0.2° grid box. A one sample t-test was also conducted on the average 15 dBZ echo top grid boxes to determine where the average 15 dBZ echo top height significantly differed from the mean echo top height at a 95% confidence level. Since the individual APR-3 profiles are not independent samples, the average 15 dBZ echo top height from each flight leg (within a grid box) is used in the significance testing.

3.3.2 *Precipitation data*

3.3.2.1 Precipitation gauges

Precipitation rate maps use a combination of OLYMPEX sites (Peterson et al. 2017a) and supplementary sources downloaded from the Mesowest archive (Horel et al. 2002). The OLYMPEX sites used pairs of co-located 20 cm or 30 cm diameter tipping buckets except for a high-elevation site which had a single Pluvio^2-400 weighing bucket (Peterson et al. 2017b). Similar to chapter 1, the average of the two tipping buckets was used if the measurements were within 5% of each other. Otherwise the greater of the two buckets was used since malfunctions tended to reduce the number of tips. The supplementary sources include Automated Surface Observing Sites (ASOS), Remote Automated Weather Stations (RAWS), Snow Telemetry (SNOTEL), and Cooperative Observer Network (COOP). The Hurricane Ridge precipitation measurements are from a heated tipping bucket in a protected location maintained by the Northwest Avalanche Center (NWAC 2018). We carefully monitored and maintained all precipitation measurements in real time throughout OLYMPEX and any sites with missing data during the study period were excluded from this study.

3.3.2.2 Disdrometers

Disdrometer measurements (Peterson et al. 2017c) were analyzed at the three sites displayed in Figure 3.1a and Figure 3.2. The Fishery site was located in the near-coastal lowlands approximately 30 km from the coast at an elevation of 52 m. The Prairie Creek site was on the first major windward ridge near Lake Quinault at an elevation of 542 m. The Hurricane Ridge site was within the transition zone between the interior high terrain and lee side at an elevation of 1603 m. The DC-8 flight patterns were configured to fly near or directly above all three sites. Table 3.1

shows the sample sizes and data quality statistics during the nine flights used in this study. The precipitation type was determined by the disdrometers. All rain was observed at Fishery and almost all rain at Prairie Creek except for ~15 minutes of mixed precipitation during three heavier showers on 13 December and a ~2.5 hour period of snow on 12 December. Hurricane Ridge recorded all snow during the three prefrontal and three postfrontal flights and all rain during the three warm sector flights.

Two different types of disdrometers were used in this study. All three sites had second generation Particle Size and Velocity 2 (PARSIVEL^2) disdrometers. The PARSIVEL^2 is a laser optical device that measures the size and fall velocity of hydrometeors passing through a 180 mm x 30 mm x 1 mm sheet laser. The raw output contains 32 size and velocity bins from 0.2 to 25 mm diameter with a time resolution of 10 s. The PARSIVEL^2 output assumes drops are falling straight down and corrects drops greater than 1 mm for oblateness. The Hurricane Ridge had a Particle Imaging Package (PIP) which is the successor of the Particle Video Imager (Newman et al. 2009). The PIP records high speed (380 frames per second) video of particles passing in front of a halogen lamp located 2 m downwind of the camera. The field of view is 48 mm by 64 mm. The PIP processing software detects and tracks particles as they fall through the observing volume. The software estimates the particle equivalent diameter (D_{eq}) by drawing a bounding box around the shadowed particle at each frame and fitting an ellipse around the particle within the bounding box. The equivalent diameter is the largest value of the major axis of the ellipse observed at any time that the particle is in the instrument field of view. The PIP instrument design is further described in Newman et al. (2009) and additional details and nuances of the detection software are found in von Lerber et al. (2017, 2018). The processed output contains 120 size bins from 0.2 to 26 mm diameter with 1-min time resolution. This study uses the PIP measurements at Hurricane

Ridge in lieu of the PARSIVEL^2 because the PIP operates reliably in strong winds, which occurred frequently at Hurricane Ridge.

3.3.2.3 Particle Size Distributions (PSDs)

Rain and snow particle size distributions (PSDs) are computed and analyzed separately. As in chapter 1, the rain PSDs from the PARSIVEL^2 were computed following Eq. (6) of Tokay et al. (2014) using terminal fall velocities from Atlas et al. (1973) and excluded periods when the instrument detected frozen precipitation or errors due to condensation/water splashing obstructing the laser optics (Table 3.1). The PIP rain PSDs came directly from the PIP software version 1403 described above. This study uses a time interval of 1 min and requires a minimum of at least 50 particles per minute for 1-min samples to be included. Following Thompson et al. (2015) and chapter 1 the rain PSDs are described using the median volume diameter (D_o) and normalized intercept parameter (N_w) as derived in Testud et al. (2001). This technique is particularly useful because a given PSD with an approximately gamma distribution can be characterized using only D_o and N_w. D_o is computed from the binned PSDs by determining the two drop size bins in which the cumulative liquid water content reaches 50% and linearly interpolating between those two bins (Hardin and Guy 2017). N_w is computed using D_o in Eq. (8) of Testud et al. (2001).

The irregular shape of ice particles makes PSD parameterization more difficult for snow than rain. This study considers histograms of 1-min values of D_o, particle concentration, and maximum diameter (D_{max}). D_{max} is approximated by the midpoint of the largest bin with at least one particle. Although the PIP was located on the roof of an ~2.5m tall building, the PSDs at Hurricane Ridge could still be contaminated at times by blowing snow or snow falling and blowing from nearby trees. To mitigate this problem, 1-min PSDs are only retained if the co-located K-band (24 GHz) Micro Rain Radar (MRR) measured reflectivity of > -10 dBZ at 300 m above the disdrometer.

Table 3.1 shows that the MRR most significantly reduced the sample on 4 December owing to weak shallow echo, which could have been due to tiny snowflakes, blowing snow, or a combination of both.

3.3.3 *Soundings*

A Colorado State University Sounding Unit at the NPOL site on the Pacific Coast (Figure 3.1) obtained rawinsonde soundings during all DC-8 flights. These data from these measurements were quality controlled following Ciesielski et al. (2014). At least one sounding was launched during each DC-8 flight, which averaged 4.1 hours of observing time. If multiple soundings were launched during a flight, the sounding nearest the middle of the flight was used for analysis. Vertical profiles of moist static stability (N_m^2, Durran and Klemp 1982) were created by linearly interpolating sounding data to 200 m height intervals and computing N_m^2 over each layer.

3.4 SYNOPTIC OVERVIEW AND CASE SELECTION

Maritime frontal systems have distinct cloud and precipitation features within different sectors bounded by the warm, cold, and/or occluded fronts (Nagle and Serebreny 1962; Houze et al. 1976; Matejka et al. 1980; Houze and Hobbs 1982; Medina et al. 2007; Houze et al. 2017; Zagrodnik et al. 2018). The prefrontal (or early) sector is associated with the initial period of stratiform precipitation as the warm or occluded front approaches the coast. Warm sectors are located to the south of the surface low pressure center between the warm front and cold-frontal zone. Postfrontal sectors are located behind the cold or occluded front in a region of cold advection over the relatively warm waters of the Pacific Ocean. As described below, storm sectors were classified using soundings. The classifications are consistent with PK18, with the caveat that

prefrontal periods in this study can refer to the period prior to a warm or occluded front. PK18 excluded occluded fronts including 01-02 December and 12 December.

Nine OLYMPEX APR-3 flights produced 37.1 measurement hours, which we have divided into three categories based on the storm sector in which they occurred. Eight flights were excluded because of instrumentation problems, limited sampling due to short mission length, isolated/nonexistent precipitation, or a flight pattern not over the Olympic Mountains. Figure 3.2 shows the flight tracks divided by storm sector. Colors denote five geographic regions used to subdivide the data for CFADs: ocean, coast, windward, high terrain, and lee. The DC-8 flew a remarkably consistent SW-NE orientated ovular 'racetrack' pattern covering all five regions, with occasional deviations.

Table 3.2 contains the breakdown of APR-3 observation time by geographic region for each case. An APR-3 profile is defined as a single nadir profile. The 3 December flight had the shortest flight duration and least number of profiles. The 13 November flight had a small number of profiles relative to the flight duration because some of the legs extended outside of the study domain. Eight of the nine missions sampled all five of the geographic regions, except there were no leeside measurements on 13 November. The ocean was the most sampled of the five regions, accounting for 29% of the included profiles. The lee side received the least sampling, 10% of the total. The coast, windward, and high terrain regions each accounted for about one fifth of the total profiles.

The variability among storm sectors is readily apparent in the infrared satellite images and overlaid 500 hPa contours shown in Figure 3.3 from each of the nine flights used in this study. The three subsections below describe the synoptic conditions that were used to classify the flights into prefrontal (top row of Figure 3.3), warm sector (middle row of Figure 3.3), and postfrontal (bottom row of Figure 3.3) sectors.

3.4.1 *Prefrontal*

The three prefrontal cases in the top row of Figure 3.3a-c each contained a broad shield of –40 ℃ or colder cloud tops covering Western Washington State and the near-coastal waters with embedded colder cloud tops likely associated with mesoscale elements (Houze et al. 1976; Hobbs 1978; Matejka et al. 1980). The sounding-derived parameters for each case in Table 3.3 show that the prefrontal sectors all had low-level flow veering from southeasterly at 925 hPa to southwesterly at 700 hPa and high static stability in the 950-850 hPa layer, a consequence of warm advection associated with the approaching warm or occluded front. The hodographs in Figure 3.4 and the moist static stability profiles in Figure 3.5 both confirm stable stratification during these three prefrontal periods and veering low-level flow in the 1-3 km layer, conditions which were conducive to blocked or deflected low-level flow. High values of Integrated Vapor Transport (IVT) (500-600 kg m^{-1} s^{-1}) and 20-30 m s^{-1} flow at 925 hPa (Table 3.3) indicate strong synoptic-scale forcing. The greatest variability between cases is seen in the melting level height, as the lower 500 hPa heights and more westerly flow aloft (Figure 3.3c) suggested a much lower 0°C isotherm on 12 December than in the other two prefrontal cases.

3.4.2 *Warm Sectors*

The warm sector IR satellite images (Figure 3.3d-f, middle row) show a nonuniform, broken pattern of colder cloud tops in the vicinity of the Olympic Peninsula with approaching banded clouds to the west or northwest associated with the cold frontal band. Although the soundings always resembled warm sector conditions, some precipitation associated with the approaching frontal band was sampled in this study. Consistent with the alignment of the 500 hPa geopotential height contours, the 925 hPa wind directions in Table 3.3 show that the low-level (925 hPa) flow impinged on the southern side of the Olympic Peninsula on 3 December and the

west-southwest side on 13 November and 8 December. The hodographs (Figure 3.4b) show less veering than the prefrontal sector and the moist static stability profiles (Figure 3.5b) were fairly close to moist-neutral at low-levels, especially from 1-4 km. The combination of high melting level (2-3 km), strong IVT (> 500 kg m^{-1} s^{-1}, Table 3.3), and moist-neutral stability suggest that all these of these warm sectors contained corridors of strong horizontal vapor transport commonly referred to as atmospheric rivers (e.g. Ralph et al. 2004).

3.4.3 *Postfrontal*

The postfrontal IR satellite images (Figure 3.3g-i, bottom row) all show regions of open-cellular convective elements with embedded mesoscale features located along and offshore of the Washington coast. There is considerable case-to-case variability in the amplitude and position of the upper-level trough. Variability in the large-scale synoptic environment is reflected by differences in low-level wind amplitude and direction (Figure 3.4c, Table 3.3). However, the moist static stability (Figure 3.5) profiles were nearly identical: unstable below 1.5 km and close to moist-neutral above 1.5 km. Other commonalities include relatively low melting levels (1-1.4 km, Table 3.3), weak IVT (< 400 kg m^{-1} s^{-1}, Table 3.3) and weak directional wind shear (Figure 3.4c).

3.5 RESULTS

3.5.1 *Prefrontal*

3.5.1.1 Reflectivity Structure

To illustrate examples of some of the features noted below in the statistical distributions, Figure 3.6 shows transects of APR-3 Ku-band reflectivity across the full Olympic Mountains range, one from each storm sector. The prefrontal example (Figure 3.6a) shows stratiform precipitation upstream of the mountains with relatively uniform echo height. The echo tops sloped

downward from the windward to the high terrain and there was a complete loss of reflectivity over the lee side. The near-surface reflectivity eventually recovered farther downstream to the northeast of the Olympic Mountains (Figure 3.6b).

All of the APR-3 transects from the three prefrontal periods (as described in Section 3.3.1) are aggregated into normalized Ku-band reflectivity CFADs in Figure 3.7 for the full sample (Figure 3.7a) and for the five geographic regions shown in Figure 3.2 (Figure 3.7b-e). In general, the mode of reflectivity decreases at a constant slope with height from 20-30 dBZ at 1 km to $\leq$ 10 dBZ above 6 km. The outlier contours (10%, 30%) are fairly close to the modal contours (50%, 70%, 90%), suggesting a narrow distribution that lacks temporal variability. Both of these characteristics indicate a predominance of a uniform, mature stratiform echo. The one CFAD that deviates from this pattern is the lee side which had substantially lower reflectivity below 3 km despite appearing similar to the other regions above 3 km.

Differences in reflectivity between regions are highlighted in Figure 3.8, where the coast, windward, high terrain, and lee normalized CFADs are subtracted from the normalized ocean CFAD. In general, laterally adjacent positive (red) and negative (blue) contours indicates intensification or weakening of reflectivity at a particular height level. An area of positive or negative contours without a corresponding region of the opposite sign indicates a change in the shape of the distribution as a whole, either a narrowing/broadening or a shift in the mode to a different height level. In Figure 3.8b, the rightward shift to a higher frequency of reflectivities greater than 20 dBZ and lower frequency of reflectivities below 20 dBZ at levels between 2.5 and 5.0 km indicates modest enhancement of reflectivity over the windward slopes. The high terrain pattern (Figure 3.7Figure 3.8c) is caused by a narrow increase in ~25 dBZ reflectivity below 3 km. Lee side reflectivities (Figure 3.7f, Figure 3.8d) in the 20-30 dBZ range are diminished most

prominently in the lower levels. Overall, these patterns indicate modest enhancement predominately upstream of high terrain and rapid diminishment at lower levels on the lee side.

Figure 3.9 supplements the CFADs by showing the geographic distribution of the average height of the 15 dBZ echo top and the coverage of profiles containing at least 15 dBZ reflectivity at any height in locations with sufficient aircraft coverage. Prefrontal cases experience a very slight increase in 15 dBZ echo tops over the windward slopes on the south side of the Olympic Mountains (Figure 3.9a). Incoming flow may be lifting over the stably stratified lower layer (Figure 3.5), leading to higher echo tops upstream of terrain, similar to results shown upstream of other mountain ranges by Houze et al. (2001) and James and Houze (2005). The discontinuity in the bright band along the windward slopes in Figure 3.6a could also be indicating upstream lifting or possibly blocked cold air in the Quinault Valley (Colle 2004; Smith and Barstad 2004; Minder et al. 2011). PK18 showed that terrain-induced gravity waves tilted upstream with height (Durran 1990) contributed to the apparent upstream enhancement. Echo coverage of greater than 15 dBZ was nearly 100% everywhere during the prefrontal flights except for a sharp decline to less than 25% coverage on the northeast side of the Olympic Mountains (Figure 3.9b).

3.5.1.2 Precipitation Characteristics

Figure 3.10 shows histograms of 1-min D_o and $\log(N_w)$ derived from rain PSDs measured by PARSIVEL^2 disdrometers at the Fishery site (solid lines) and Prairie Creek site (dashed lines). Each case is shown as a separate line. The rain PSDs at the Fishery and Prairie Creek are tightly clustered between $1 < D_o < 1.5$ mm and $3 < \log(N_w)$ $m^3mm^{-1} < 4$ (Figure 3.10a,b). This range is consistent with the "most frequent" PSD regime defined in chapter 2 (section 2.4.1) which was associated with synoptic conditions resembling the prefrontal sector, specifically stable stratification at low levels and southeasterly 925 hPa winds that do not impinge directly on the

southwesterly-facing terrain. The distributions of D_o and N_w show little variability between cases or sites, consistent with the nearly identical average precipitation rates at the two sites (3.4 mm h^{-1} at Fishery, 3.3 mm h^{-1} at Prairie Creek) during the prefrontal cases. Prairie Creek did favor slightly larger drops than Fishery, possibly a byproduct of the slight enhancement above the melting level on the windward side seen in Figure 3.8b. In general, the prefrontal PSDs represent characteristic stratiform precipitation dominated by drops of modest size and concentration.

The snow particle size and number histograms at Hurricane Ridge are shown Figure 3.11. The prefrontal snow PSDs (Figure 3.11, left column) show a surprising amount of case-to-case variability given the relatively uniform rain PSDs on the windward side. Large concentrations of small particles dominated on 12 December and almost no particles larger than 6-7 mm diameter were observed (Figure 3.11c,e). The other two prefrontal cases had a greater variety of particle sizes and concentrations including a longer D_{max} tail reaching values of 10-15 mm. Two possible causes of higher particle concentrations on 12 December are colder temperatures at Hurricane Ridge (Figure 3.11a) and stronger cross-barrier winds at 700 hPa (Table 3.3), both of which may lead to turbulent motions are unfavorable for observing snow aggregates at the surface (Houze 2014). The stronger cross-barrier winds on 12 December may have also advected more particles over from the windward side, as the 15 dBZ echo tops heights had less decline from windward side to the high terrain compared to the other two prefrontal cases (not pictured). As a whole, these three cases suggest that high-terrain snow PSDs tend to be more variable than rain PSDs in prefrontal sectors, although the CFADs in Figure 3.7 indicate that there are no inherent differences in reflectivity structure over the high terrain compared with the coast and windward side.

As a way to summarize the characteristics of the precipitation structure in each storm sector, Figure 3.12 provides the average hourly precipitation rate during APR-3 flights at the

various ground sites for the different storm sector cases. The corresponding rain rates at the disdrometer sites for each case are presented in Table 3.4. For the prefrontal cases, the average prefrontal precipitation rates were highest (~3-5 mm h^{-1}) on the coast and the southern side of the Olympic Mountains (Figure 12a). On the southwest side of the mountains there was minimal difference in precipitation rate between the coast and the Quinault Valley and neighboring windward slopes, consistent with the lack of appreciable enhancement in the CFADs (Figure 3.8). Precipitation rates fell off rapidly to 1 mm h^{-1} or less across the high terrain and lee side.

3.5.2 *Warm Sectors*

3.5.2.1 Reflectivity Structure

The APR-3 transect in Figure 3.6c,d nicely illustrates some of the key differences between prefrontal and warm sector reflectivity structures. This example clearly shows deep echo over the windward and high terrain regions with a secondary enhancement layer around 5 km. The echo extended to the leeside in spite of the reduction in height of the echo top. The echo on the leeside was especially pronounced within and above the bright band (3-4 km), suggesting downstream advection of ice particles that were formed over the terrain. Reduction of echo was much less than found for the prefrontal cases (Figure 3.6a). The near-surface reflectivity in Figure 3.6d confirms the reduced rain shadow relative to the prefrontal example in Figure 3.6b.

The normalized warm sector CFADs in Figure 3.13 differ markedly from the prefrontal CFADs in Figure 3.7. All of the CFADs have broader distributions then the prefrontal CFADs at any given height, suggesting a greater variety of sizes and/or concentrations of hydrometeors. Rather than a constant slope with height, both the overall modal and outlier contours (Figure 3.13a) have two rightward bulges associated with larger reflectivity: one between 2-3 km associated with the bright band and the other between 4-6 km associated with a secondary enhancement layer aloft.

A secondary enhancement in the ice layer was previously observed over coastal terrain in California by Kingsmill et al. (2006), in the Oregon Cascades by Medina et al. (2007), and in OLYMEX by McMurdie et al. (2018). Co-located APR-3 and in situ Citation aircraft observations in the 3 December 2015 case (Chase et al. 2018) showed spherical ice particles and rimed aggregates within a region of enhanced reflectivity at 4 km elevation. Figure 3.14 shows that this secondary enhancement is most pronounced over the windward slopes and high terrain above the bright band in the 3-6 km layer.

Another noteworthy feature in the warm sector normalized CFADs is the relatively low height of the modal contours, especially over land (Figure 3.13c,d,e,f). The increased frequency of lower-level reflectivities without accompanying increases at upper-levels suggests the importance of low-level enhancement processes over terrain. The low-level mode in reflectivity (>50% contours below 2 km) tends to be relatively weak over the ocean (mode of 10-25 dBZ) but increases slightly at the coast and especially over terrain. In the windward and high terrain regions (Figure 3.14b,c) the enhancement signature is present throughout the precipitating cloud, suggesting a juxtaposition of enhancement in both the ice and liquid portions of the precipitating cloud. The varying role of these precipitation-generating processes was explored in chapter 1 and is further described with disdrometer observations in the next section.

Unlike the prefrontal sector, the warm sector enhancement signature reaches farther downstream to the lee side (Figure 3.13f, Figure 3.14d), where more frequent occurrence of stronger reflectivities relative to the ocean are seen more prominently below 3 km. The progressive lowering of the ice enhancement layer from the windward to high terrain to lee regions in Figure 3.14b,c,d are indicative of the advection of ice particles by strong cross-barrier winds (Table 3.3, Figure 3.4) originating from the deeper layer of clouds over the windward and high terrain regions.

Two of the three warm sector cases had 700 hPa winds in excess of 30 m s^{-1} (Table 3.3). It is possible that enhanced microphysical growth within the secondary enhancement in the ice layer at 4—6 km previously discussed could be contributing to the increased downstream spillover in warm sectors, a postulation supported by the bright band enhancement signature at 2-2.5 km in Figure 3.14d. Spillover may also be fostered by reduced lee side descent in warm sectors (PK18).

Maps of 15 dBZ height and coverage corroborate the precipitation processes described above (Figure 3.9c, d). Precipitating clouds have relatively low average height and only about 50% spatial coverage over the ocean and coast in the warm sectors. The maximum height and coverage of 15 dBZ echo was over 5.5 km and located directly over the Olympic Mountains range. In warm sectors, complex terrain is responsible for both the enhancement of pre-existing precipitation as well as the generation of additional and/or stronger precipitating clouds to reach 100% coverage. The precipitating cloud decreases in height downstream of the highest terrain, but precipitation is advected to the lee side, resulting in 80-100% coverage of >15 dBZ echo over most of the northeast side of the Olympic Peninsula (Figure 3.9b).

3.5.2.2 Precipitation Characteristics

Compared to the prefrontal sector, the warm sector rain parameter histograms in Figure 3.10c,d have broader distributions within individual cases, greater case-to-case variability, and more significant differences between the Fishery and Prairie Creek sites. The 3 December case bears the closest resemblance to the prefrontal histograms with relatively similar distributions at Fishery and Prairie Creek peaking at similar D_o and N_w values. In contrast, 13 November and 8 December have broad distributions of D_o and N_w with greater differences between Fishery and Prairie Creek. Table 3.4 shows that these two cases also featured considerably higher rain rates at Prairie Creek (14 mm h^{-1}) than Fishery (5 mm h^{-1}) while on 3 December the rain rate at Prairie

Creek was nearly identical to Fishery (~3 mm h^{-1} at both sites). The main synoptic difference was the southerly direction of the low-level winds on 3 December (Table 3.3, Figure 3.4b), which does not favor enhancement of precipitation on the southwest (Quinault) side of the Olympic Mountains where the ground sites were located. Previous studies show that the direction of the low-level flow and IVT vector strongly influences the location of heavy precipitation within atmospheric river events (Neiman et al. 2011, Hecht and Cordeira 2017), by favoring warm precipitation processes over the low- to mid-elevation windward slopes that are directly impinged on by the low-level flow (Zagrodnik et al. 2018).

Figure 3.15 shows the warm sector rain D_o and N_w distributions over the high terrain at Hurricane Ridge. Figure 3.10 andFigure 3.15 should not be quantitatively compared because the PIP and PARSIVEL^2 have different sensitivities to small particles. The relative shapes of the distributions at Hurricane Ridge are narrower than Fishery and Prairie Creek. Also, the 3 December case is not a much of an outlier. Instead all of the distributions closely resemble the prefrontal rain PSDs on the windward side (Figure 3.10a,b). In a three-dimensional (dome-shaped) mountain range like the Olympic Mountains, the low-level flow orientation appears to have a lesser influence over the high terrain than the windward slopes, thus reducing the difference in PSD between 3 December and 8 December at Hurricane Ridge. Presumably most of the high terrain precipitation originated from ice processes above the bright band. The Hurricane Ridge PSDs may also be reflecting microphysical changes occurring within the spillover process. Two possibilities are particle segregation as larger particles preferentially fall out upwind of Hurricane Ridge and particle breakup as a consequence of the strong cross-barrier flow (Table 3.3).

The map of average warm sector precipitation rates (Figure 3.12b) shows a sharp increase in precipitation rates from 1-2 mm h^{-1} at the coast to a maximum of 8-11 mm h^{-1} (Figure 3.12b)

on the low-to-mid elevation windward slopes. These low rain rates at the coast imply that the overwhelming majority of warm sector precipitation occurs as a consequence of flow modification by the Olympic Mountains (Zagrodnik et al. 2018). The variety of PSDs associated with windward side precipitation implies that, consistent with the CFADs (Figure 3.13Figure 3.14), orographically enhanced precipitation may originate from particles generated in the ice layer, liquid layer, or a combination of both.

Modest precipitation rates of 0.4-2.4 mm h^{-1} were observed on the lee side. While these precipitation rates are objectively unimpressive, they may contribute an appreciable fraction of the modest seasonal precipitation totals in the drier lee side. Given the presumed advection and fallout timescales of ice particles and the progressively lower height of the upper-level enhancement over the windward, high terrain, and lee side (Figure 3.14b-d), ice particles produced within the secondary enhancement layer are likely falling out farther downstream over the high terrain and lee side. This often results in equal or greater precipitation rates on the lee slopes than upstream at the coast (Figure 3.12b). Although the PSDs varied by case, the precipitation rate at Hurricane Ridge was close to 3 mm h^{-1} in all three warm sectors (Table 3.4). While some case-to-case variability exists in PSDs at Hurricane Ridge, the degree of variability is far less than the windward locations that appear to be more strongly influenced by warm precipitation processes.

Another notable feature of Figure 3.10c,d and Figure 3.15 are the smaller D_o and remarkably high N_w on 13 November that is present to an extent at all three ground sites, suggesting large concentrations of small raindrops that were likely produced by warm precipitation processes (Zagrodnik et al. 2018). Several pieces of evidence suggest that warm precipitation processes were dominant in this case. The consistently small D_o and high N_w at the Fishery site (Figure 3.10c,d), indicates a lack of contribution from stratiform rain forced by the synoptic system, which produces

PSDs closer to those observed in the prefrontal sector (Figure 3.10a,b). Additionally, the 15 dBZ echo top height was the lowest of the three warm sector cases over the ocean, coast, windward side, and high terrain (not shown)[6]. Despite the apparent lack of ice processes, this case experienced the highest precipitation rates of any case in this study (Table 3.4).

3.5.3 *Postfrontal*

3.5.3.1 Reflectivity Structure

Figure 3.6e shows an example of how the postfrontal precipitation structures differ from the other storm sectors. Over the ocean the aircraft observed a shallow, isolated convective cell with a convective core extending only to about 3 km height. The PPI image (Figure 3.6f) shows that this cell was near the edge of a broad region of isolated convective showers. At the coast, the precipitation was more stratiform in nature with a well-defined bright band and stronger echoes remaining relatively shallow. Over terrain, the echoes were broader and somewhat deeper but also horizontally heterogeneous, suggesting a mix of convective and stratiform type precipitation with some embedded updrafts.

The postfrontal CFADs in Figure 3.16 also have different shapes than both the prefrontal and warm sector CFADs. The concentration of the modal contours in the lower levels indicates that postfrontal precipitation is generally shallower and more convective in nature than other storm sectors. Postfrontal echo over the ocean was generally weak, 10-20 dBZ, although it occasionally reached 30-40 dBZ in isolated convective cores below 2 km.

As the postfrontal precipitation moved from ocean to coast to the windward to the high terrain (Figure 3.16b-e), the modal distribution in the CFADs narrowed and shifted downward and

[6] The DC-8 did not fly over the lee side on 13 November.

to the right. The high terrain distribution in particular was dominated by 20-30 dBZ echo below 4 km and very little corresponding echo at higher levels. Compared to the stratiform-dominated prefrontal CFADs (Figure 3.7), the postfrontal high terrain CFAD had a much higher occurrence of echoes > 20 dBZ above the bright band (located below the 1.5 km bottom of the postfrontal CFADs, Table 3.3), suggesting strong but shallow upward motion and robust ice production. Figure 3.9e,f confirm that the precipitation broadens in coverage but does not appreciably deepen over terrain. The 15 dBZ echo tops reached a similar height on average over the ocean, coast, windward, and high terrain, while the 15 dBZ echo coverage more than doubled from the ocean to the high terrain.

These statistics suggest that isolated postfrontal convective showers undergo a transition to broader, more stratiform-like nature as they move from the ocean to the high terrain of the Olympic Mountains. There are several potential reasons why postfrontal precipitation changes in character over land: (1) different surface sensible and latent heat fluxes between ocean and land (Bond and Fleagle 1988, Sikora et al. 2011); (2) the widespread release of conditional instability as the cells encounter complex terrain (Figure 3.5); (3) widespread orographic lifting of near moist neutral air following release of instability produces stratiform cloud and precipitation between active convective elements (Cannon et al. 2012). The moist static stability profiles in Figure 3.5 show that conditional instability is concentrated in the lowest 1.5 km and the profiles are nearly moist-neutral above 1.5 km. In this environment it is not surprising that the postfrontal enhancement of reflectivity over terrain (Figure 3.17a-c) occurs mostly below 3 km. The slightly deeper enhancement at the coast (Figure 3.17a) may be a sampling artifact due to the more isolated nature of postfrontal cells upstream of terrain.

As in other storm sectors, precipitation intensity declines over the lee side in the postfrontal sector. The leeside CFAD (Figure 3.16f) and difference CFAD (Figure 3.17d) shows weakened echo above 3 km relative to the ocean. Figure 3.9e-f show a corresponding reduction in 15 dBZ echo height and reduced coverage on the north and northeast portion of the Olympic Mountains. Some of the precipitation in the leeside CFAD is a result of westerly-component large-scale flow (Figure 3.4c) during two of the three postfrontal cases. In those cases, the northern side of the Olympic Mountains was not the truly the lee side. Westerly flow allowed shallow postfrontal cells to move eastward through the Strait of Juan de Fuca rather than transecting the Olympic Mountains. Still, the reduced precipitation rates on the northern and northeastern side of the high terrain including at Hurricane Ridge (Figure 3.12c) indicates that postfrontal precipitation that does transect the mountains eventually weakens as it approaches the lee side, where downward motion occurs aloft.

3.5.3.2 Precipitation Characteristics

Figure 3.10e,f show that all three of the postfrontal cases exhibited broad histograms of D_o and N_w at both Fishery and Prairie Creek, although N_w did not reach as high as two of the warm sector cases. The similarity between the two sites is unsurprising given the postfrontal rain rate was only 1 mm h^{-1} higher at Prairie Creek than Fishery (Figure 3.12c). Most of the enhancement between Fishery and Prairie Creek occurred on 13 December (Table 3.4) and it was mostly a result of larger D_o. The broad distributions are a consequence of the convective nature of postfrontal precipitation, a property that is mostly retained at the windward Prairie Creek site despite a somewhat narrower CFAD distribution in Figure 3.16d.

The Hurricane Ridge snow parameter histograms in Figure 3.11b,d,f are also fairly broad, although not appreciably more so than for the prefrontal sector. The 4 December case had some

very light precipitation that may have included blowing snow (discussed in section 3.3.2). The D_o modes were all around 2.5-3.0 mm. Particle concentrations were fairly high but not beyond what was observed in the prefrontal sector (Figure 3.10f). The most notable aspect of the postfrontal disdrometer measurements is that all three cases recorded numerous 10-15+ mm diameter aggregates, especially 13 December which had a mode above 10 mm. Figure 3.12c shows that the average postfrontal precipitation rates increased from < 1 mm h^{-1} at the coast to 2-4 mm h^{-1} over the windward slopes and gradually decreased down to 0-2 mm h^{-1} over the high terrain and lee side. While the precipitation rates over the high terrain were modest, the low melting levels and the long duration of some of the postfrontal periods resulted in significant snow accumulation over the high terrain during OLYMPEX.

3.6 CONCLUSIONS

This study has examined airborne precipitation radar data, surface precipitation measurements, and particle size distributions from nine storms passing over the three-dimensional (dome-shaped) Olympic Mountain range during the OLYMPEX field campaign. The prefrontal, warm sectors, and postfrontal events had distinct synoptic-scale environmental conditions as reflected in sounding-derived wind and moist static stability profiles (see Sec. 3 and Figure 3.4Figure 3.5). Consistent with Zagrodnik et al. 2018 and PK18, the differing synoptic-scale conditions were related to storm sectors. The degree of windward enhancement and leeside diminishment of precipitation, though always present, varied considerably from case to case. The dynamical and microphysical mechanisms by which the pre-existing precipitation was modified by terrain depended on the airflow and stability properties of the incoming air mass and nature of the preexisting precipitation forced by the frontal cyclone prior to landfall. We documented the following processes in each storm sector:

3.6.1 *Prefrontal*

Prefrontal precipitation contained a predominance of a uniform, mature stratiform echo both over ocean and over terrain with little time variance in reflectivity and particle size distributions on the windward side of the barrier. Deeper echoes and modest enhancement of mid-level reflectivity were observed over the windward slopes along with a corresponding slight increase in precipitation totals. The stably stratified prefrontal storm environment encouraged mid-level lifting upstream of the barrier near then coast and suppressed low-level lift on the windward slopes. Echo tops declined beginning over the high terrain and low-level reflectivity diminished considerably in the lee, resulting in a near-complete rain shadow on the northeast side of the Olympic Mountains.

3.6.2 *Warm sectors*

Warm sectors featured deep and intense enhancement of reflectivity above, within, and below the melting level over both the windward slopes and high terrain. The composition and intensity of warm sector precipitation was not uniform but rather was highly variable in both in the upstream clouds over the ocean and on the windward slopes. The two cases where the low-level flow aligned with the southwest-facing Quinault valley resulted in the greatest enhancement of precipitation on the lower-windward slopes, consistent with descriptions of atmospheric rivers by Neiman et al. (2017) and Chapter 1. Warm precipitation processes made an appreciable contribution to the enhancement, as evidenced by PSDs favoring high drop concentrations (high N_w) in the two cases with southwesterly flow. In contrast to prefrontal periods, even the leeside precipitation was enhanced within and below the bright band, suggesting a spillover of frozen hydrometeors from higher levels over the windward side and high terrain. The spillover was facilitated by strong cross-barrier winds advecting ice particles that were produced upstream over terrain possibly from

enhanced ice particle growth within the secondary reflectivity maximum at 4-5 km. Particle size data at Hurricane Ridge showed that the advected precipitation was rather homogeneous and lacked the undulations in particle size and concentration that occurred at the windward sites.

3.6.3 *Postfrontal*

Postfrontal precipitation was predominantly isolated and convective in nature over the ocean. Over land, it transitioned to a broader and more widespread stratiform echo while retaining intense cores, characteristic of embedded convection. The surface rain and snow particle size distributions were correspondingly variable, consistent with the precipitation being a mixture of convective and stratiform. Precipitation totals were enhanced on the windward side and over the high terrain and diminished on the lee side, although moisture flowing from west to east through the Strait of Juan de Fuca appeared to reduce the degree to which the echo was diminished below 3 km.

3.6.4 *Implications*

The enhancement of rain on the windward sides of west coastal mountain ranges and drying on leesides is of utmost importance for hydrologic, climatic, and weather forecasting applications. The results of this study show how the processes controlling the pattern of enhancement and diminishment of precipitation over a nearly circular three-dimensional coastal mountain barrier is highly sensitive to synoptic-scale properties of landfalling frontal cyclones. The OLYMPEX cases described in this study and in PK18 exhibit stronger rain shadows in the prefrontal period and weaker rain shadows in warm sectors. The dome shape of the Olympic Mountains is not conductive to prefrontal cold air trapping in the lee, allowing for descent and corresponding diminishment of echo in the lower levels of the lee (Figure 3.6a and Figure 3.7a). This study suggests that outside

of the postfrontal sector, an important mechanism producing leeside precipitation is downstream spillover of ice particles formed in deep clouds directly over the Olympic Mountains. The degree of diminishment on the leeside of the three-dimensional range is thus partially controlled by the synoptic-scale microphysical processes conducive to producing such spillover.

On the windward side, OLYMPEX data show that varying contributions of liquid and ice-phase microphysical processes between storm sectors and geographic regions are responsible for the observed precipitation patterns (Zagrodnik et al. 2018). Model simulations in PK18 required 'seeding' by background precipitation of at least 0.5 mm h^{-1} to sufficiently enhance precipitation over the windward slopes. OLYMPEX ground-based data in warm sectors show that upstream precipitation at the coast largely exceeded this rate (Figure 3.12b). However, the relatively small median particle sizes observed during warm sectors (Figure 3.10c) indicate that growth by collection of cloud water by ice particles is not necessarily the dominant enhancement mechanism. Rather, the consistently high drop concentrations on the lower-windward slopes (Figure 3.10d) suggest that warm rain processes make a significant contribution to the high precipitation rates observed upstream of the interior high terrain. It follows that the complexity and variability of precipitation over the Olympic Mountains is not adequately explained by paradigms such as the "seeder-feeder" mechanism (Bergeron 1968) or bifurcation into brightband and nonbrightband rain (White et al. 2003). Lifting over complex terrain modifies both the lower-level warm processes and the upper-level ice processes, often concurrently. The lifting over the terrain moreover varies with the differences in synoptic/dynamic conditions in different storm sectors. Different precipitation patterns result depending on which processes are dominant in the portion of the synoptic scale storm passing over the mountains.

3.7 TABLES AND FIGURES

Table 3.1. Sample sizes and data quality statistics from the three disdrometer sites used in this study. At Fishery and Prairie Creek (PARSIVEL^2 sites), good data includes minutes where the disdrometer was functional and reporting rain with no error codes. For Hurricane Ridge (PIP and MRR site), snow is considered good data and the rightmost column additionally constrains the dataset to minutes when the MRR reflectivity at 300 m above the site was > -10 dBZ. The MRR was not functioning during the 2015 Nov 13 event.

			Fishery		Prairie Creek		Hurricane Ridge		
Case	Category	Sample size (min)	% Good data	% > 50 particles/ min	% Good data	% > 50 particles/ min	% Good data	% > 50 particles/ min	% MRR > -10 dBZ
2015 Dec 01-02	Prefrontal	239	100	100	100	100	99	81	79
2015 Dec 05	Prefrontal	238	100	100	100	100	100	98	95
2015 Dec 12	Prefrontal	309	100	100	47	47	99	94	85
2015 Nov 13	Warm Sector	305	75	73	100	100	94	86	n/a
2015 Dec 03	Warm Sector	127	100	90	100	92	100	100	100
2015 Dec 08	Warm Sector	292	100	93	100	100	100	98	98
2015 Dec 04	Postfrontal	201	61	46	71	50	84	71	43
2015 Dec 10	Postfrontal	257	92	63	89	62	100	100	98
2015 Dec 13	Postfrontal	243	82	53	97	89	100	100	89

Table 3.2. Characteristics of each of the 9 cases included in this study, including storm sector, flight times, the number of APR-3 vertical profiles, and the percent of profiles observed in each geographic sector. The percent values are computed with respect to the full sample in each geographic sector so that the columns add up to 100%.

Case	Category	APR-3 Start Time (UTC)	APR-3 End Time (UTC)	# APR-3 Profiles	% Ocean	% Coast	% Windward	% High Terrain	% Lee
2015 Dec 1-2	Prefrontal	2126	0124	7426	13.6	12.2	10.6	15.8	12.3
2015 Dec 5	Prefrontal	1421	1818	6873	8.6	10.8	13.4	13.8	19.0
2015 Dec 12	Prefrontal	1611	2119	7653	13.1	16.3	11.2	11.2	17.2
2015 Nov 13	Warm Sector	1417	1921	5179	12.3	10.3	12.7	4.6	0.0
2015 Dec 3	Warm Sector	1443	1649	3027	2.9	5.6	6.0	7.4	6.2
2015 Dec 8	Warm Sector	1333	1824	6356	10.9	9.7	12.0	12.0	11.9
2015 Dec 4	Postfrontal	1330	1650	6471	12.3	12.7	12.1	9.9	7.7
2015 Dec 10	Postfrontal	1513	1929	7017	15.3	11.5	10.7	11.7	9.9
2015 Dec 13	Postfrontal	1413	1815	6845	10.9	10.8	11.2	13.7	15.9

Table 3.3. Synoptic parameters derived from soundings launched at the NPOL radar site shown in Figure 3.1a for each case.

Case	Category	NPOL Sounding (UTC)	IVT (kg m^{-1} s^{-1})	Melting Level (m)	925 hPa speed (m s^{-1})	925 direction (deg)	700 hPa speed (m s^{-1})	700 hPa direction (deg)	950-850 hPa N_m^2 x 10^{-4}
2015 Dec 1-2	Prefrontal	2317	500	2103	23.3	166	17.6	218	1.06
2015 Dec 5	Prefrontal	1514	560	2031	30.3	160	18.3	216	0.98
2015 Dec 12	Prefrontal	1914	529	879	21.1	158	28.1	234	1.31
2015 Nov 13	Warm Sector	1632	575	2583	22.0	240	19.0	250	0.19
2015 Dec 3	Warm Sector	1516	784	2150	26.2	172	33.3	203	-0.21
2015 Dec 8	Warm Sector	1515	815	2769	52.2	214	32.3	231	0.64
2015 Dec 4	Postfrontal	1517	99	1219	8.8	235	11.5	256	-0.68
2015 Dec 10	Postfrontal	1736	393	1344	24.8	233	23.1	233	-0.82
2015 Dec 13	Postfrontal	1516	187	1027	15.1	289	17.0	265	-0.47

Table 3.4. Average precipitation rate (mm h^{-1}) at the three disdrometer sites (see Figure 3.2 for locations) for the nine cases described in this study.

Case	Category	Fishery rain rate (mm h^{-1})	Prairie Creek rain rate (mm h^{-1})	Hurricane Ridge rain rate (mm h^{-1})
2015 Dec 1-2	Prefrontal	1.5	3.3	0.2
2015 Dec 5	Prefrontal	3.5	3.1	1.0
2015 Dec 12	Prefrontal	3.6	3.6	0.7
2015 Nov 13	Warm Sector	6.2	14.1	3.1
2015 Dec 3	Warm Sector	2.7	3.0	3.3
2015 Dec 8	Warm Sector	4.0	13.1	3.1
2015 Dec 4	Postfrontal	0.6	0.5	0.1
2015 Dec 10	Postfrontal	2.7	2.7	1.8
2015 Dec 13	Postfrontal	1.7	3.7	1.1

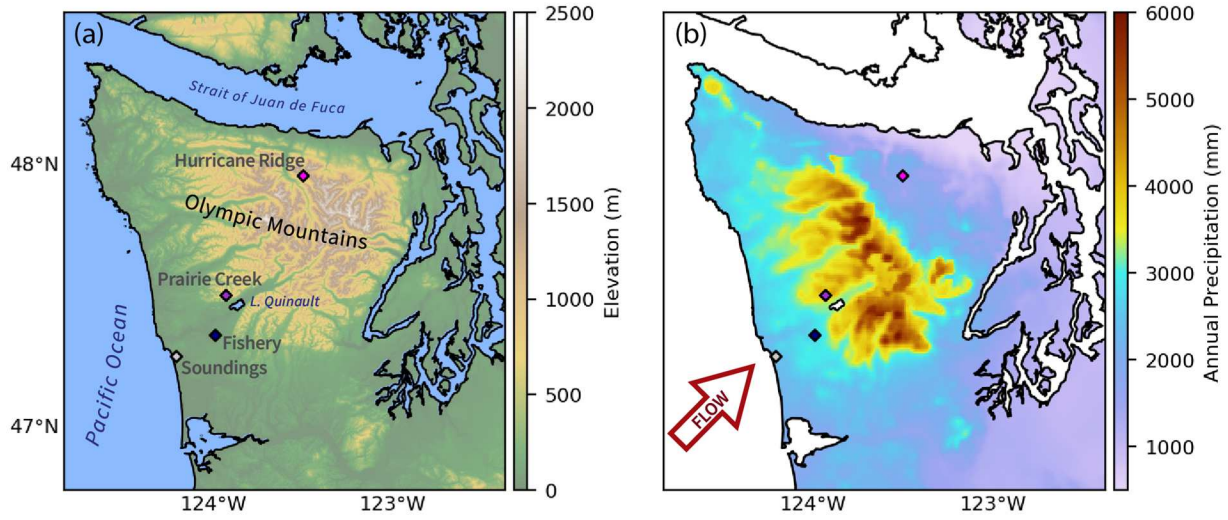

Figure 3.1: Terrain and annual precipitation of the Olympic Peninsula: (a) Topographic map; (b) Estimated annual precipitation (mm) from the PRISM model (Daly et al. 2008) over the 1981-2010 time period. Disdrometer and sounding site locations used in this study are indicated with diamonds in both panels and named in (a).

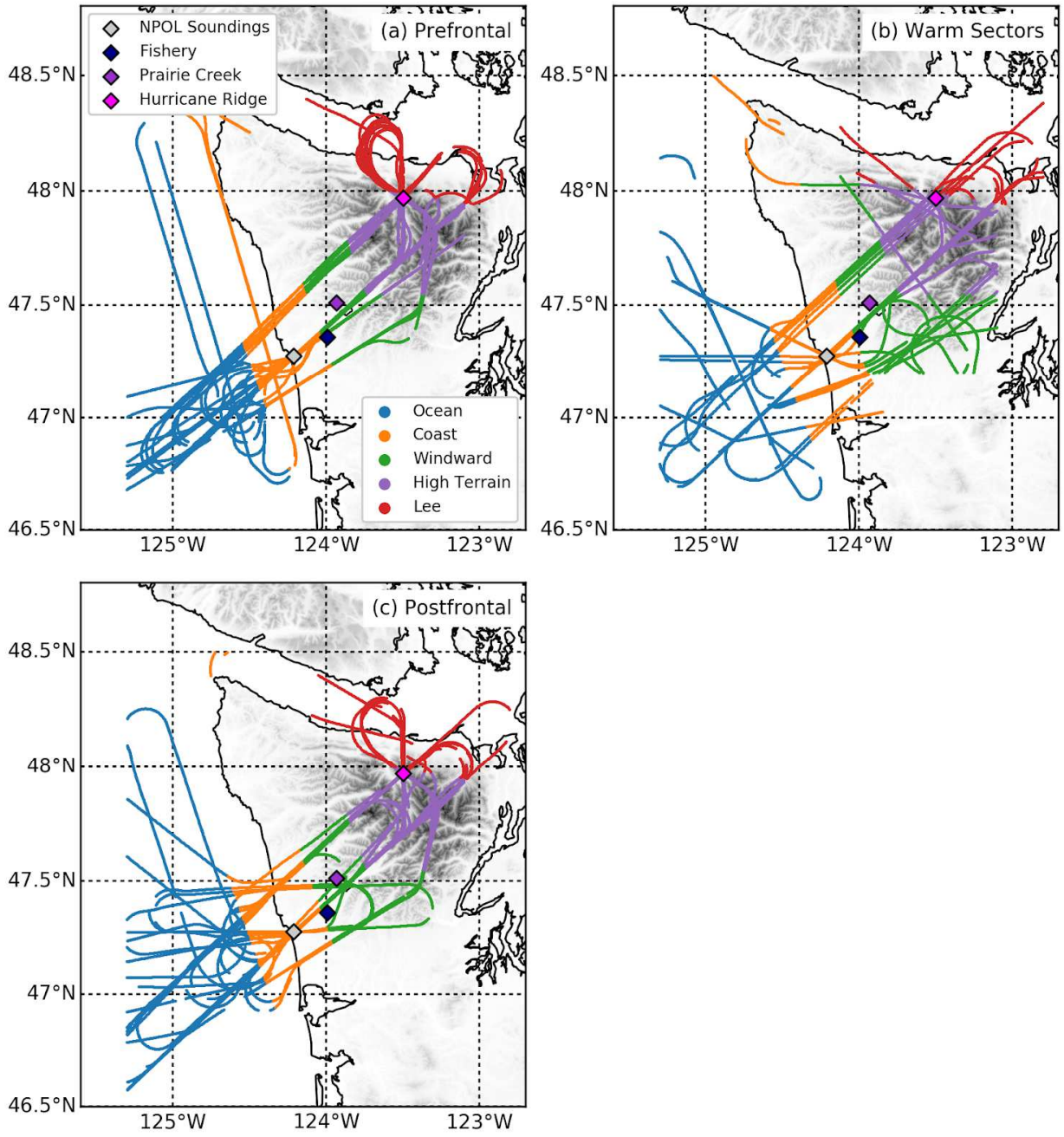

Figure 3.2: Maps of DC-8 flight tracks colored by geographic region for (a) prefrontal, (b) warm sectors, and (c) postfrontal cases. Diamonds denote the locations of the NPOL sounding launches and the three disdrometer sites used in this study.

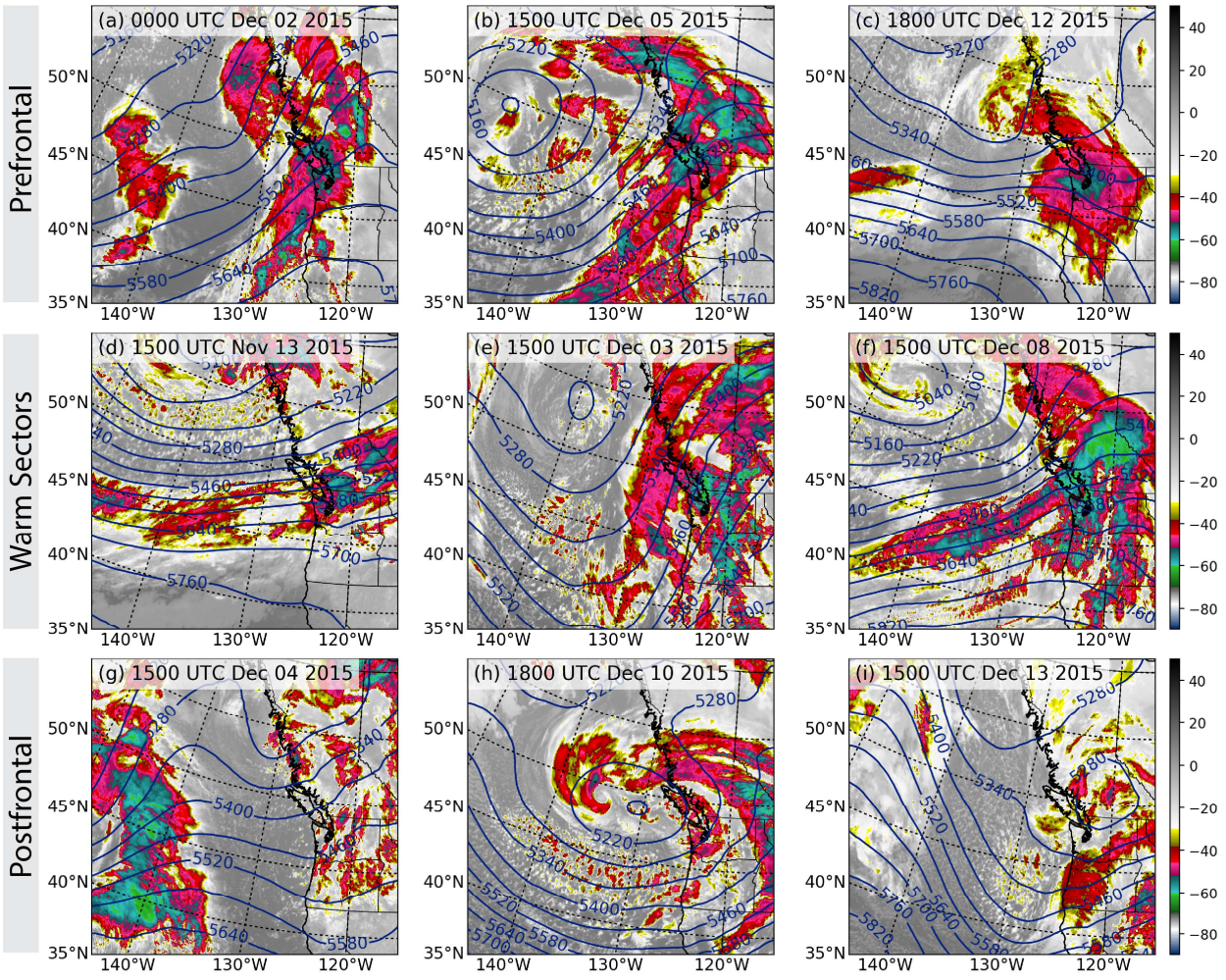

Figure 3.3: GOES West infrared imagery (filled contours, ℃) and North American Regional Reanalysis (NARR) 500 hPa heights (m, blue contours) for the closest NARR analysis time for the nine cases listed in Table 3.2: (a) 0000 UTC 02 December 2015; (b) 1500 UTC 05 December 2015; (c) 1800 UTC 12 December 2015; (d) 1500 UTC 13 November 2015; (e) 1500 UTC 03 December 2015; (f) 1500 UTC 08 December 2015; (g) 1500 UTC 04 December 2015; (h) 1800 UTC 10 December 2015; (i) 1500 UTC 13 December 2015.

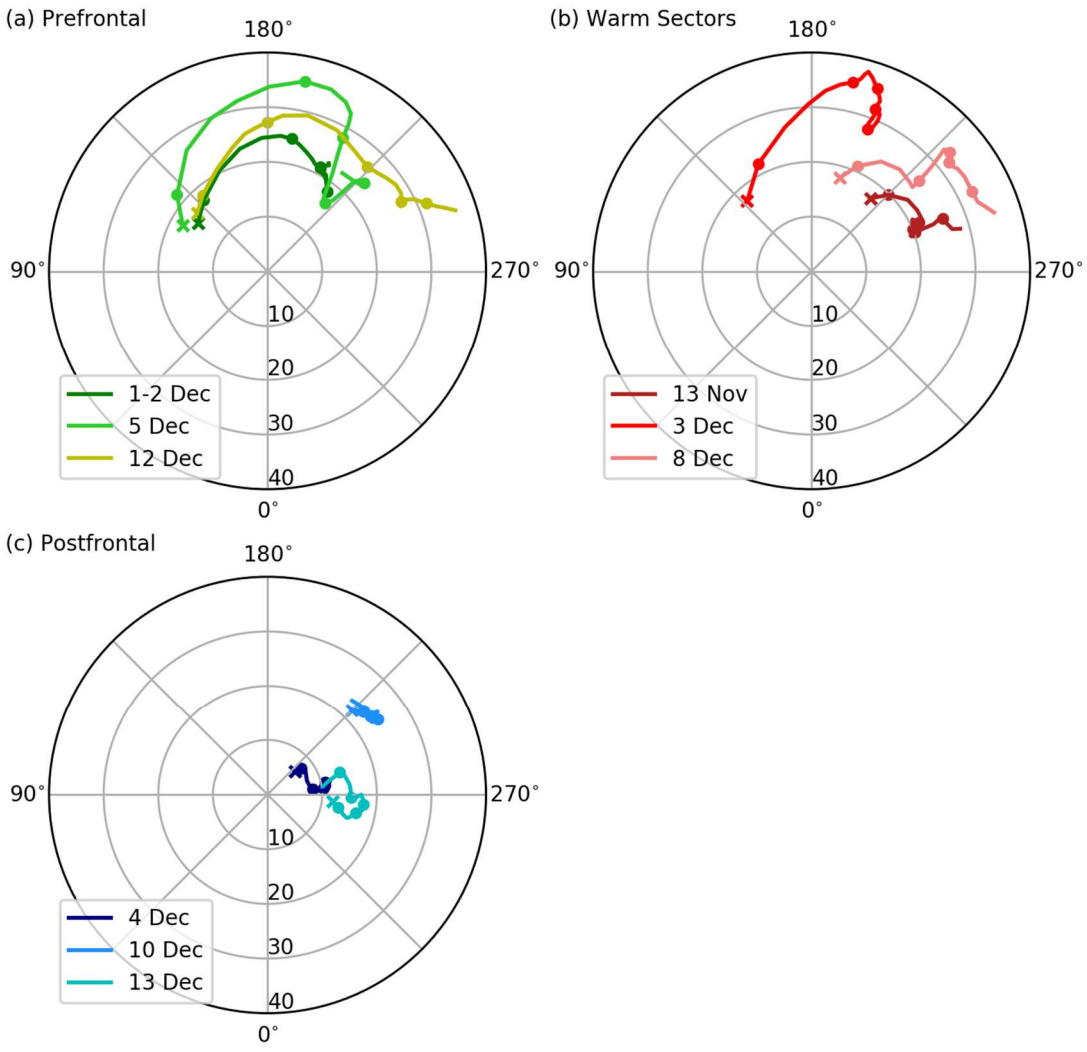

Figure 3.4: Hodographs of the (a) prefrontal, (b) warm sectors, and (c) postfrontal cases from the NPOL soundings in Table 3.3. Rings are in increments of 10 m s^{-1}. X's indicate the lowest level and dots are placed at 1 km height intervals from 1-5 km.

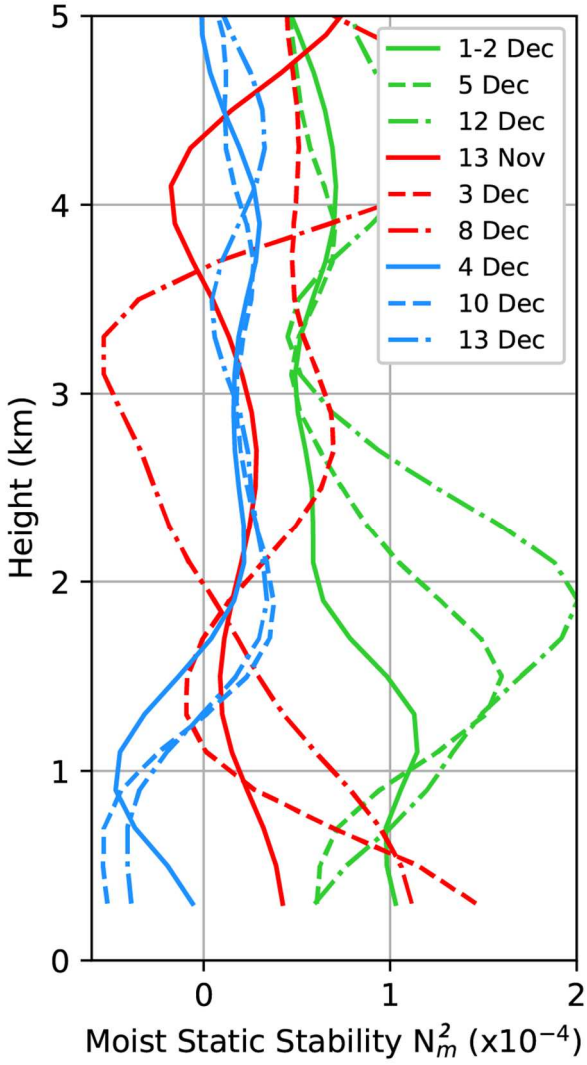

Figure 3.5: Vertical profiles of moist static stability (N_m^2 x 10^{-4}) derived from the NPOL soundings for each of the 9 cases detailed in Table 3.3. The green profiles are for the prefrontal cases, red for the warm sector cases and blue for the postfrontal cases.

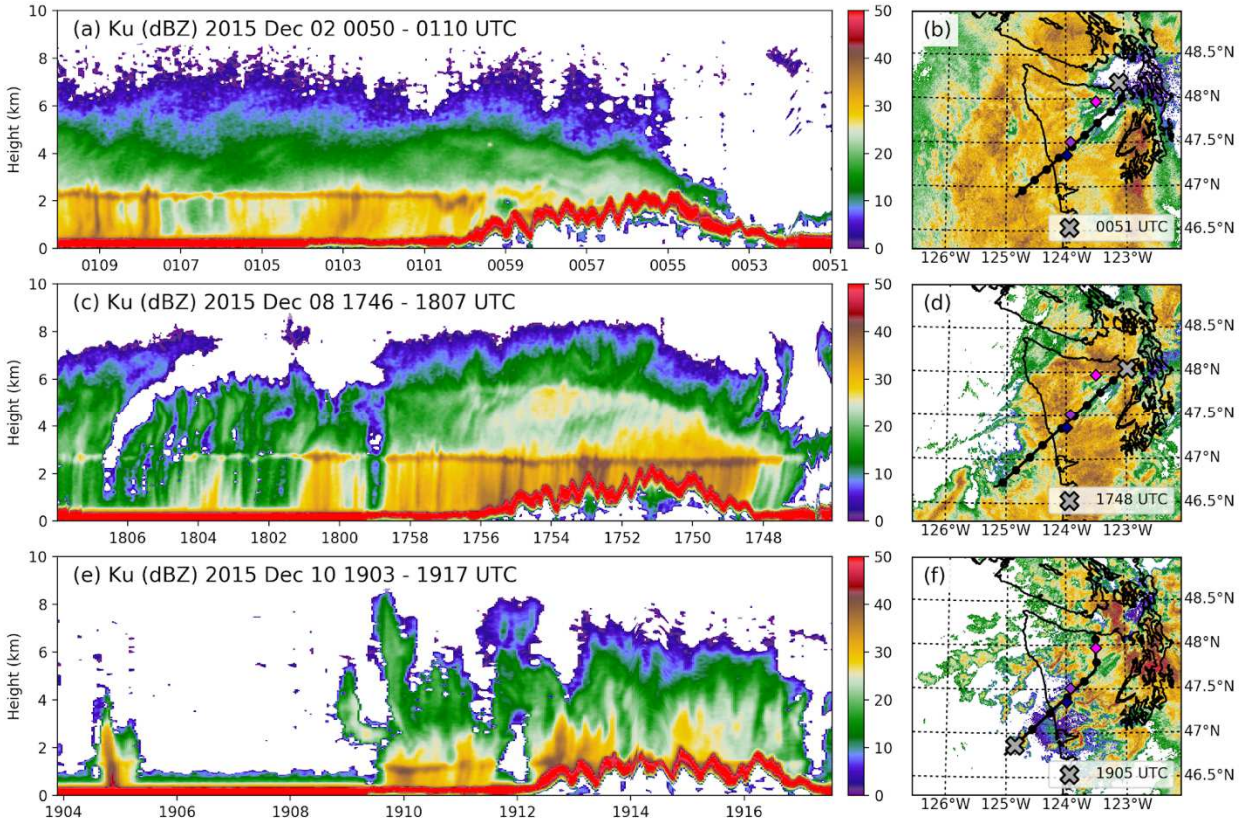

Figure 3.6: Time-height cross sections of APR-3 Ku reflectivity (left column) and flight track maps (right column) for (a-b) 2015 December 02, (c-d) 2015 December 08, and (e-f) 2015 December 10. Composited Plan Position Indicator (PPI) scans of reflectivity at 0.5° azimuth from the Langley Hill (KLGX) and Whidbey Island (KATX) radars are included in the right column. The times in the left column match the black dots in the right column with the "X" denoting the starting time of the cross-section. Colored diamonds denote the disdrometer site locations as in Figure 3.1.

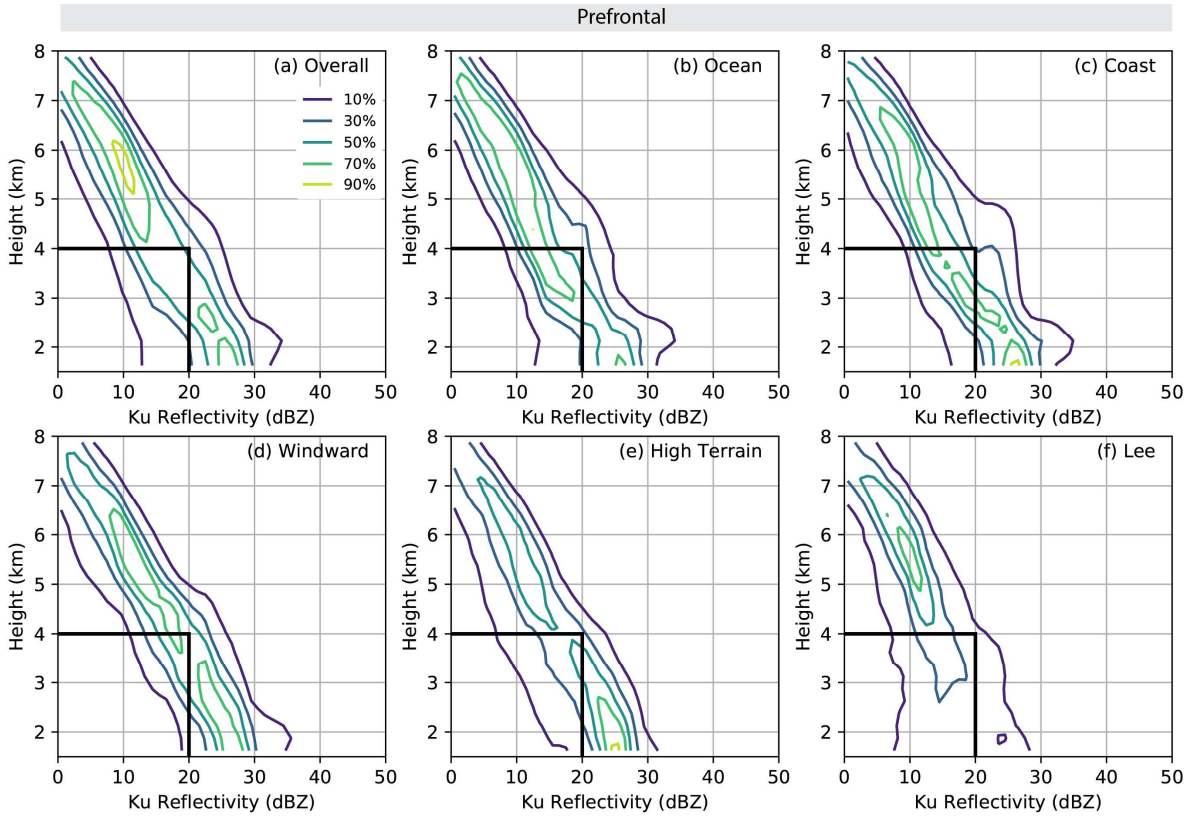

Figure 3.7: Prefrontal contoured Frequency by Altitude Diagrams (CFADs) of APR-3 Ku-band reflectivity for all geographic regions (a) and the five geographic regions (b-f) denoted in Figure 3.2. The CFADs are normalized where each frequency is divided by the maximum overall frequency and contours represent the frequency of occurrence relative to the maximum absolute frequency. Thick black lines at 4 km and 20 dBZ are for reference. Heights are relative to sea level.

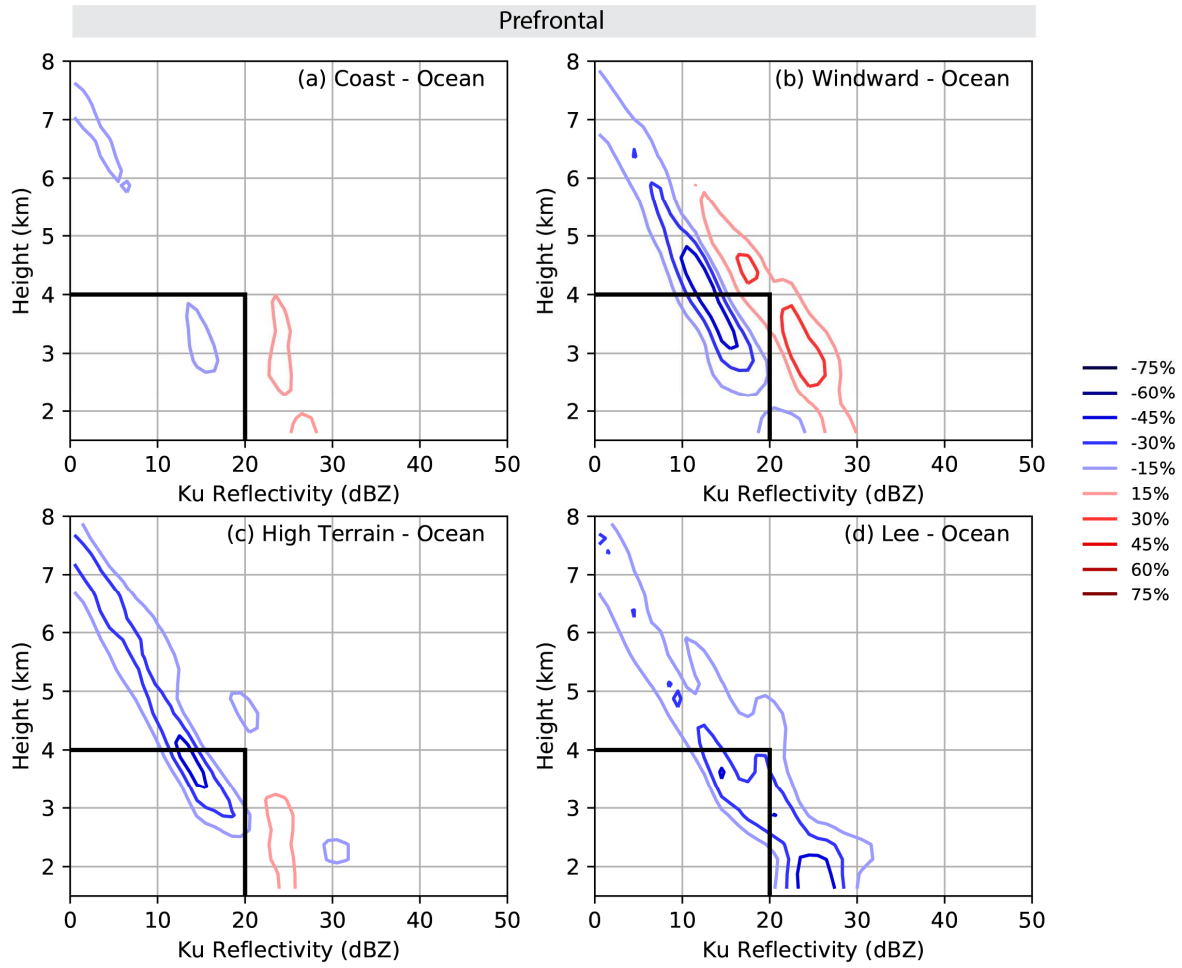

Figure 3.8: Prefrontal difference CFADs computed by subtracting the ocean CFAD in Figure 3.7b from the (a) coast, (b) windward, (c) high terrain, and (d) lee side CFADs. Contours represent the frequency difference between the two geographic regions. Thick lines at 4 km and 20 dBZ are for reference.

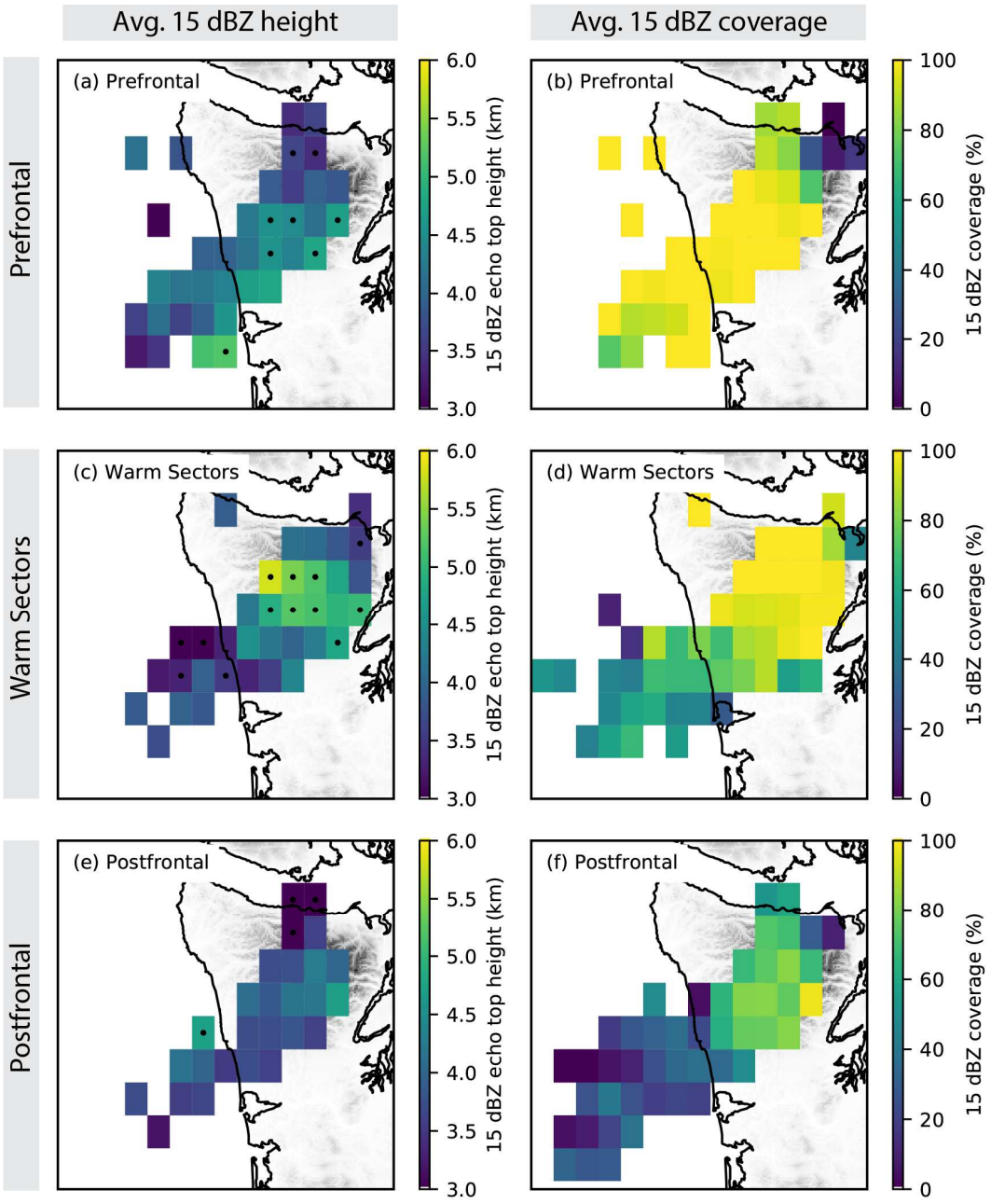

Figure 3.9: Gridded maps (0.2° x 0.2°) of APR-3 Ku-band average 15 dBZ echo top height (km, left column) and frequency of greater than 15 dBZ reflectivity at any height level (percent, right column) for (a-b) prefrontal, (c-d) warm sectors, and (e-f) postfrontal cases. The dots in the left column represent grid boxes with statistically different means than the average (one-sample t-test, 95% confidence interval).

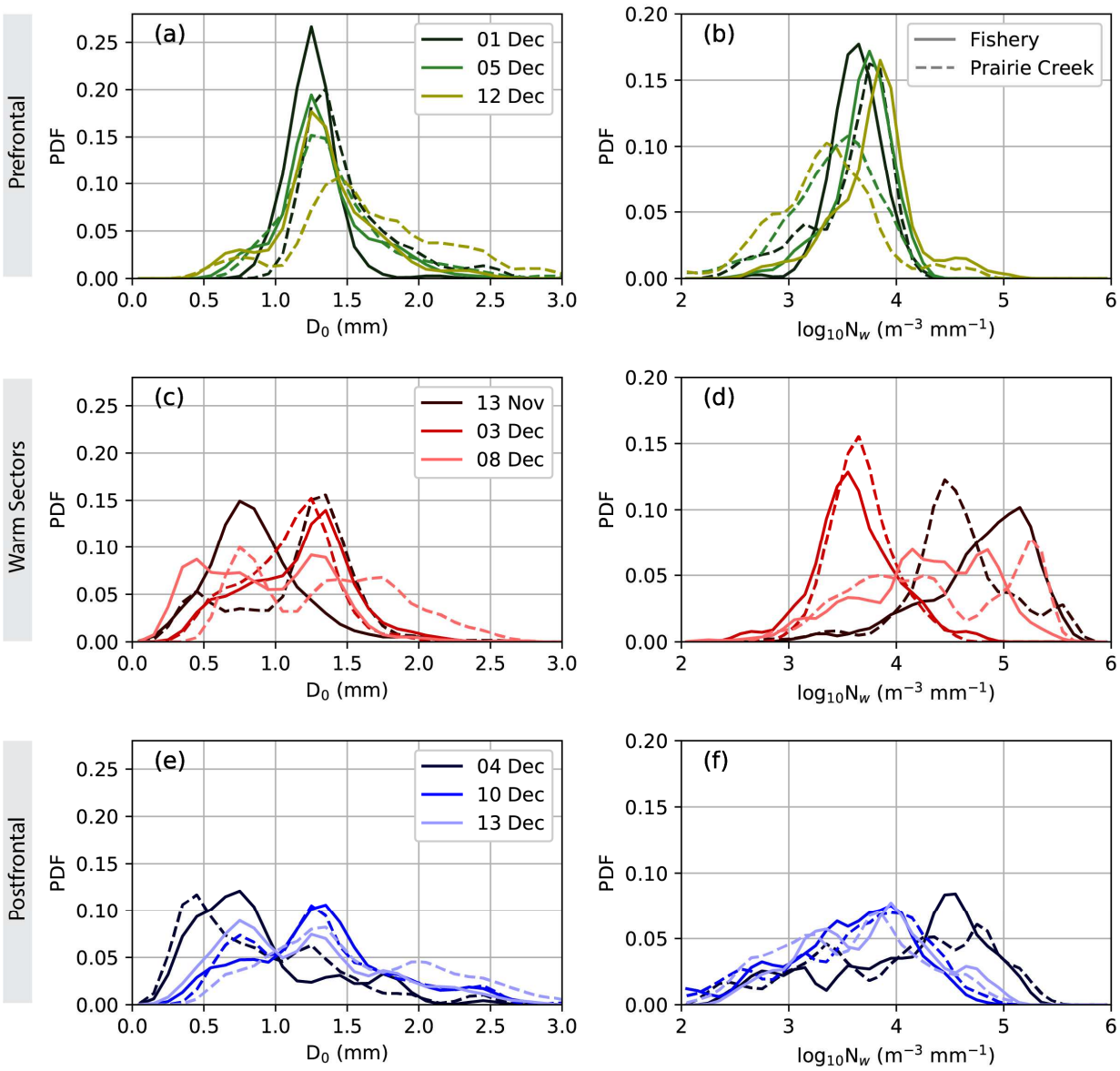

Figure 3.10: Histograms of 1-min D_o (left column) and N_w (right column) measured by PARSIVEL^2 disdrometers at Fishery (solid lines) and Prairie Creek (dashed lines) for (a-b) prefrontal, (c-d) warm sectors, and (e-f) postfrontal cases.

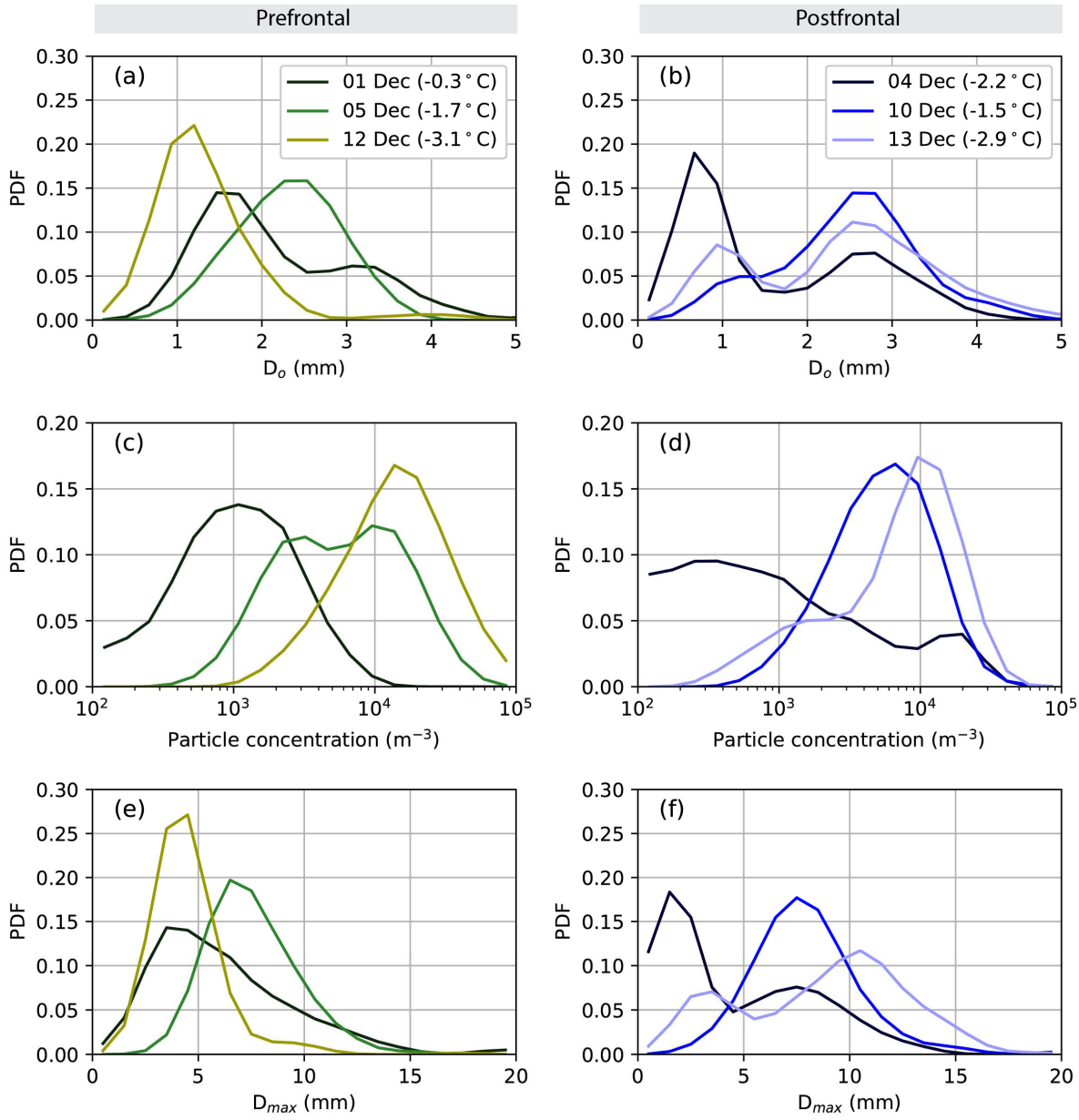

Figure 3.11: Histograms of 1-min D_o (top row), particle concentration (middle row), and D_{max} (bottom row) measured by a PIP disdrometer at Hurricane Ridge for snowing events during prefrontal (left column) and postfrontal (right column) cases.

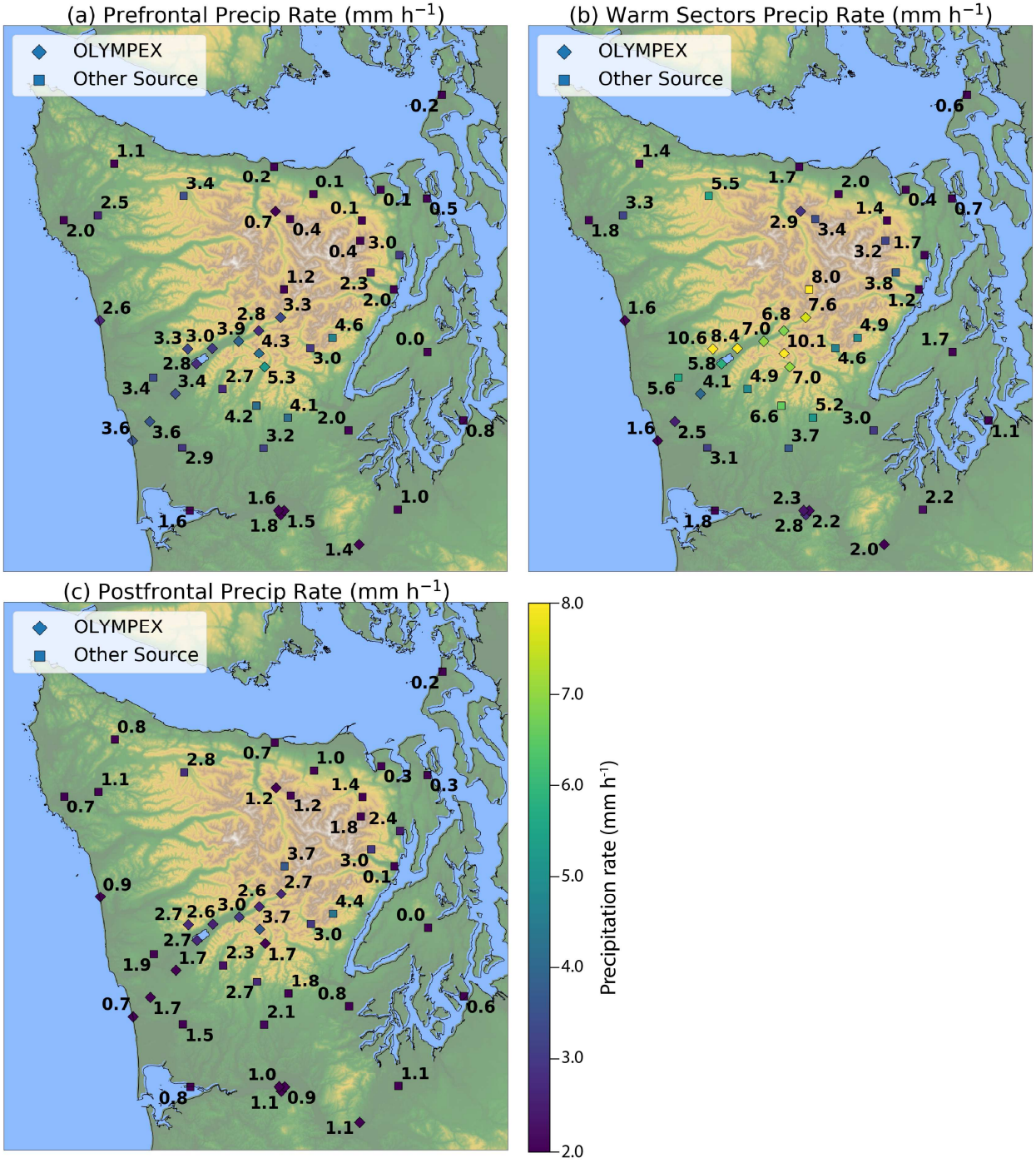

Figure 3.12: Average precipitation rate (mm h^{-1}) at various ground sites during the (a) prefrontal, (b) warm sectors, and (c) postfrontal cases.

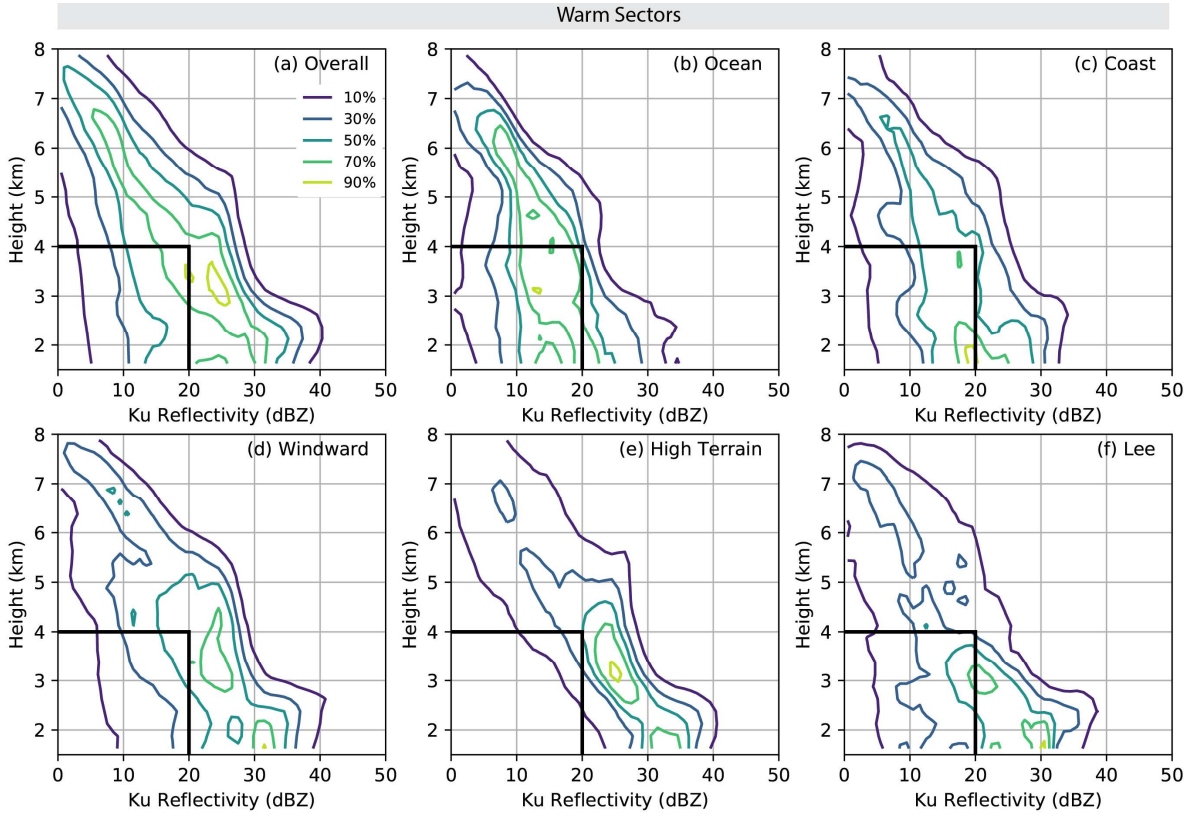

Figure 3.13: As in Figure 3.7 except for warm sectors.

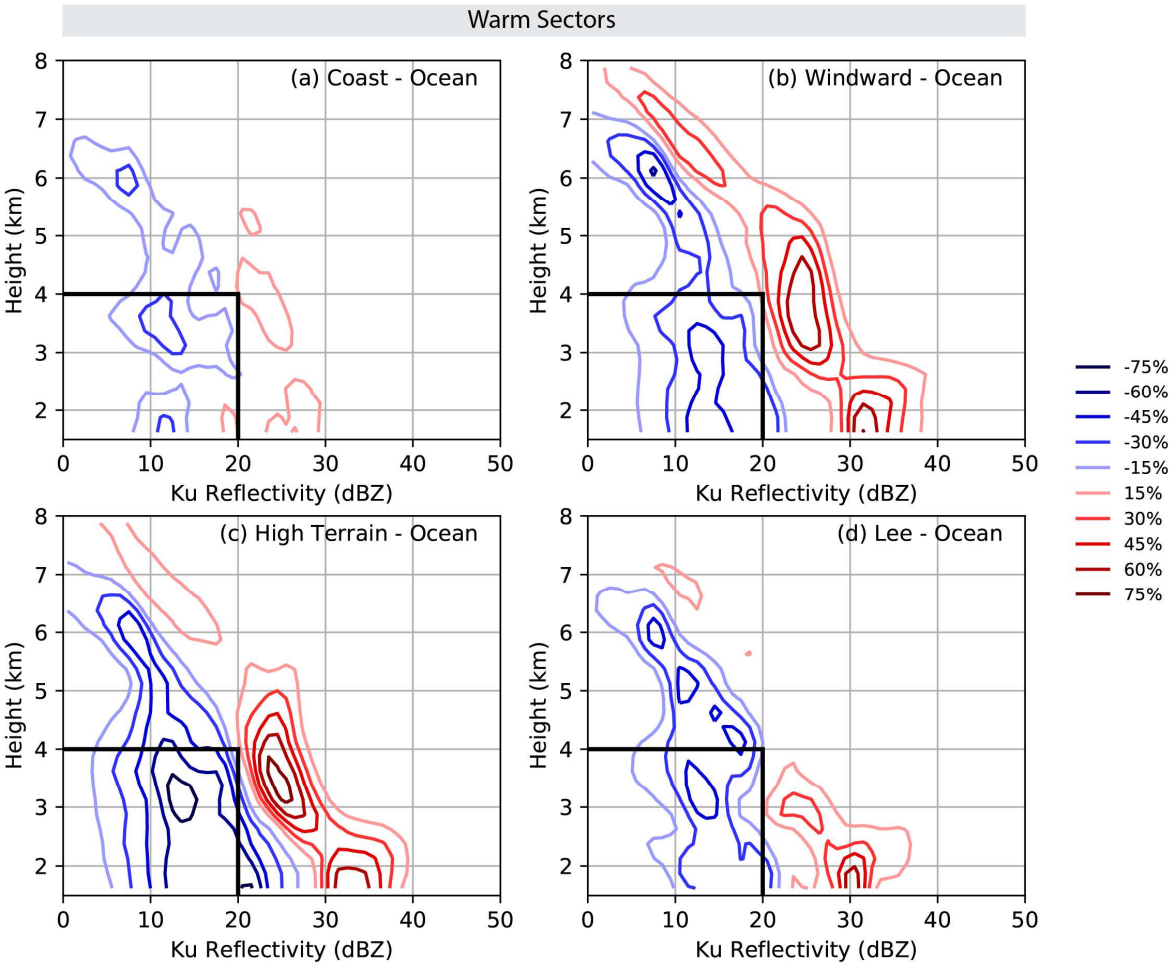

Figure 3.14: As in Figure 3.8 except for warm sectors.

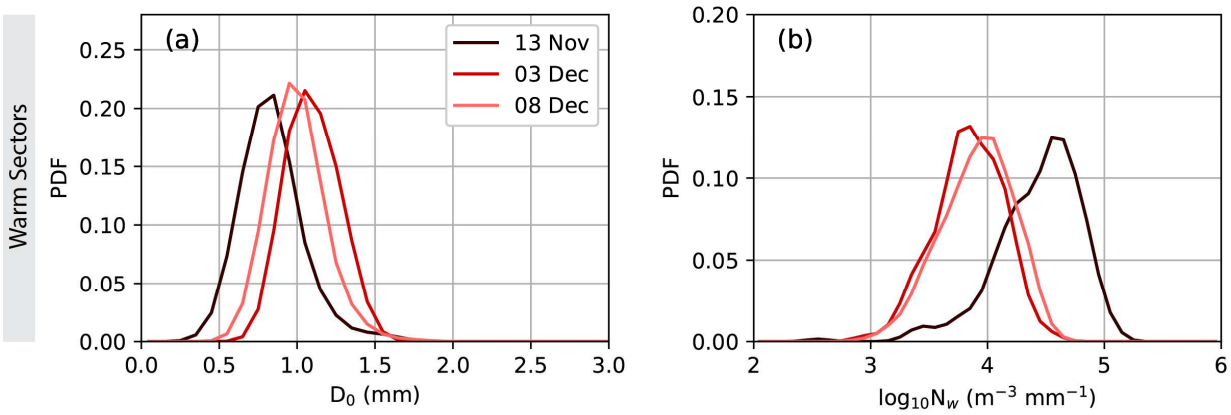

Figure 3.15: Histograms of 1-min D_o (left column) and N_w (right column) measured at Hurricane Ridge during raining events for warm sector cases.

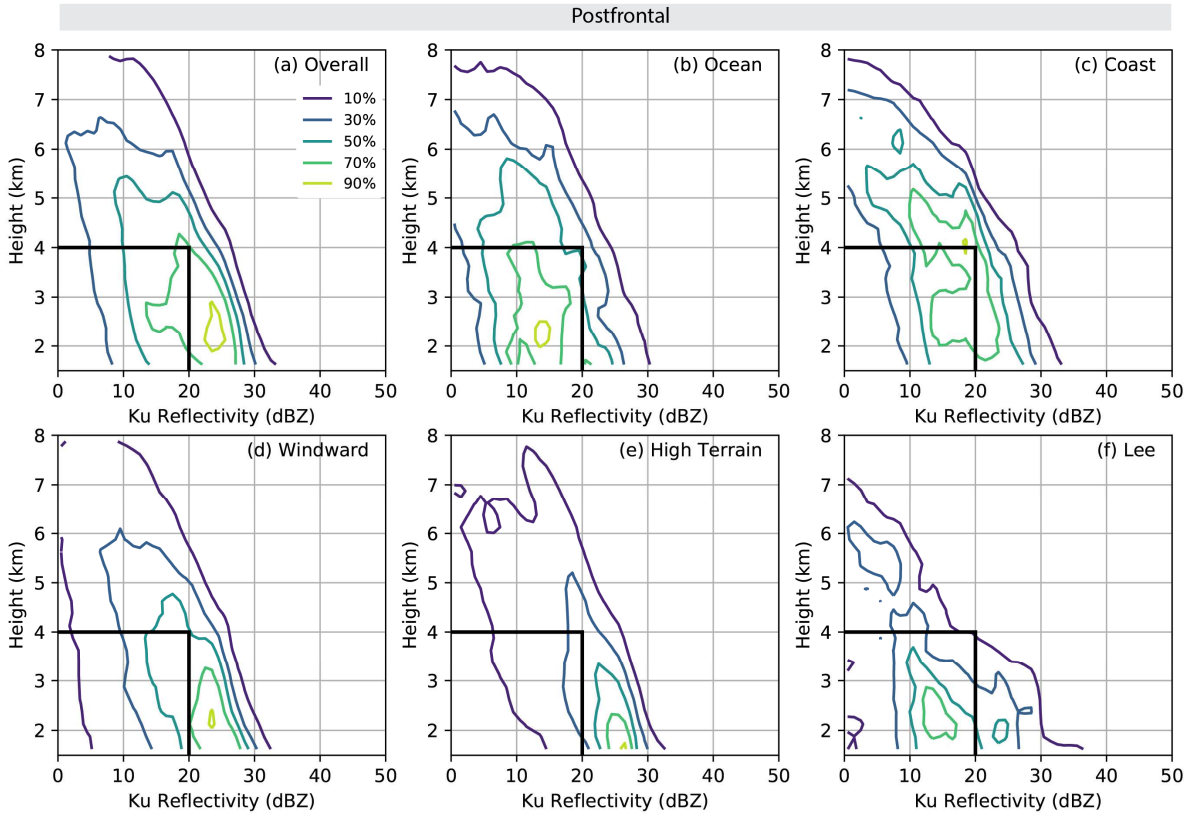

Figure 3.16: As in Figure 3.7 except for postfrontal cases.

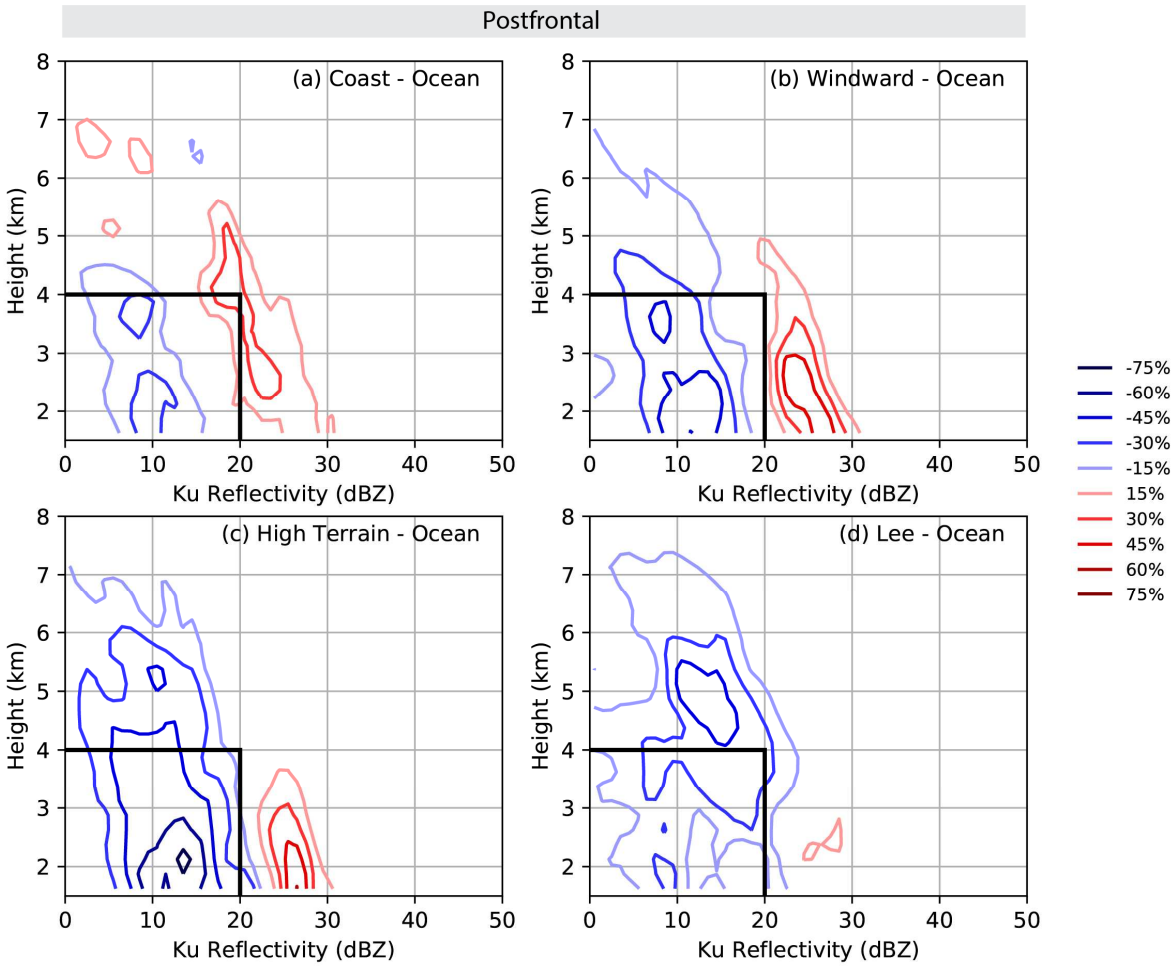

Figure 3.17: As in Figure 3.8 except for postfrontal cases.

Chapter 4. MULTISCALE PRECIPITATION PROCESSES IN STRATIFORM PRECIPITATION PASSING OVER A COASTAL MOUNTAIN RANGE

4.1 ABSTRACT

The degree to which mid-latitude cyclones modify precipitation patterns over a coastal mountain range is strongly dependent on the synoptic environment dictated by a cyclones' frontal structures. High-resolution numerical model simulations within different storm sector cases occurring during the 2015-16 Olympic Mountains Experiment (OLYMPEX) are used to examine dynamic and microphysical precipitation processes on both the larger barrier-scale and smaller sub-barrier scale ridges and valleys. Consistent with observations from the 2015-16 Olympic Mountains Experiment (OLYMPEX), differences in upstream static stability between prefrontal and warm sector cases resulted in remarkably different vertical distributions of simulated reflectivity and resultant precipitation patterns over complex terrain. In prefrontal sectors, barrier-scale ascent over stably stratified flow resulted in enhanced ice production at the coast and generally upstream of higher terrain. Small-scale mountain waves over windward ridges failed to produce enough cloud water to appreciably enhance precipitation on the scale of the windward ridges. In moist-neutral warm sectors, the upstream side of the barrier contained broad ascent with minimal downward motion. Significant quantities of cloud water were produced over coastal foothills with further enhancement of cloud water on the lower-windward slopes. Enhancement in the ice layer occurred directly over the barrier where the ice particles were further advected downstream by cross-barrier winds and spilled over into the lee.

It is hypothesized that in warm sectors, the production and maintenance of cloud water upstream of the primary topographic barrier allowed additional time for autoconversion and self-

collection to generate precipitation-sized hydrometeors that fell out on the lower-windward slopes, often without the assistance of collection by larger drops generated in the ice layer. In contrast, the couplets of ascent and descent over sub-barrier scales and ridges in prefrontal sectors result in evaporation before the cloud water can grow to precipitation size or be collected by ice-generated hydrometeors.

4.2 INTRODUCTION

As mid-latitude cyclones approach mountain ranges on the west coasts of continents, their precipitating structures are modified by changes to the three-dimensional flow field occurring on the scale of the barrier as a whole and localized perturbations over smaller-scale ridges and valleys (James and Houze 2005; Medina et al. 2007; Garvert et al. 2007; Minder et al. 2008; McMurdie et al. 2018). To the first order, patterns of precipitation over complex terrain can be approximated by a steady-state mountain wave response to a uniform, moist, and stably stratified upstream flow (Smith and Barstad 2004). Reasonable patterns of ridge-valley precipitation enhancement can be achieved by parameterizing time scales of microphysical growth, particle fallout, and advection (Anders et al. 2007). Over realistic mountains, nonlinear wave dynamics and microphysical growth processes are required to explain the rapid conversion of condensate to precipitation before it is advected over the ridge or evaporates on the lee side.

Accelerated microphysical processes are especially important on smaller-scale ridges where any condensate formed by ascent on the windward side has a small amount of time to reach precipitation size and fall out. Many studies have observed or modeled processes resembling the "seeder-feeder" effect (Bergeron 1968) which refers to the enhancement of precipitation on a small ridge when raindrops falling from a pre-existing higher cloud collect cloud drops from a separate, lower-level cloud that would otherwise fail to precipitate. In frontal cyclones approaching coastal

mountain ranges, a broader interpretation of Bergeron's framework refers to precipitation formed in the upper portion of a deep layer of nimbostratus cloud associated with a landfalling frontal system collecting cloud water in the lower levels that is enhanced by local ascent over windward mountain ridges (White et al. 2003; Minder et al. 2008; Kingsmill et al. 2016; Massmann et al. 2017; Purnell and Kirschbaum 2018). The upper and lower cloud layers are not necessarily separate, and the ice processes in the upper levels of the larger scale stratiform cloud may also be modified by terrain (Kingsmill et al. 2006; McMurdie et al. 2018). The precipitation efficiency or fallout (Jiang and Smith 2003) is improved by the collection process, ultimately leading to higher precipitation rates on the windward slopes.

An important assumption of the seeder-feeder framework is that the lower-level warm processes are inefficient because of slow autoconversion rates between cloud and rain water. Several studies over the coastal California mountains (White et al. 2003; Kingsmill et al. 2006; Martner et al. 2008) used the presence of a bright band in vertically-profiling radar to separate periods of exclusively warm (nonbrightband) rain from periods when ice-generated particles might be collecting cloud or rain water. Surprisingly, the warm rain periods, characterized by large concentrations of small rain drops, were found to produce rain rates up to 20 mm h^{-1} (White et al. 2003). While periods containing bright bands did have higher rain rates overall, these studies demonstrated that the traditional seeder-feeder interpretation was not necessary to appreciably enhance precipitation under certain conditions.

The 2015-16 Olympic Mountains Experiment (OLYMPEX, Houze et al. 2017), deployed numerous radars, rain gauges, and disdrometers at a large number of ground sites. Chapter 2 (Zagrodnik et al. 2018) used gauge and particle size data to show that the greatest precipitation enhancement occurred at lower windward elevations during strongly-forced warm sector periods

containing environmental conditions favorable for warm rain processes. The precipitation rate on the lower-windward slopes was remarkably steady during a warm sector case study despite variations in the drop size distribution caused by the passage of a deeper feature that temporarily enhanced ice processes. Lower-elevation precipitation enhancement was absent when stably stratified low levels rendered the synoptic environment unfavorable for warm rain. This observational study disagreed to an extent with semi-idealized experiments over the Olympic Mountains performed by Purnell and Kirshbaum (2018). They found significant decreases in windward precipitation efficiency in both warm frontal and warm sector simulations when the pre-existing stratiform precipitation was removed. Precipitation efficiency was appreciably improved by adding only a small amount of pre-existing precipitation (0.5 mm h^{-1}).

The above studies leave significant open questions about the relative roles of warm and ice precipitation processes in enhancing precipitation on coastal mountain ranges. OLYMPEX observations (Zagrodnik et al. 2018; McMurdie et al. 2018; Purnell and Kirschbaum 2018, Zagrodnik et al. 2019) point to the importance of warm processes in warm sector periods characterized by moist-neutral onshore flow, high melting levels, and high quantities of horizontal vapor transport. In contrast, warm processes were nearly absent during prefrontal periods containing a stably stratified environment, low melting levels, and an offshore component to the low-level wind. However, these conclusions are drawn from a limited number of ground sites, which could be affected by localized variability over small-scale ridges (Minder et al. 2008). This study evaluates the importance of warm and cold precipitation processes on the full barrier scale as well as localized ridge and valley scales using realistic Weather Research and Forecasting (WRF) simulations. The model setup and evaluation is guided by the OLYMPEX observations

detailed in Chapter 3. Model runs from several prefrontal and warm sector cases are used to determine the key processes of enhancement on different spatial scales.

4.3 Data and Methods

4.3.1 *Model Configuration*

The model runs in this study were conducted using the Advanced Research version of the Weather Research and Forecasting Model (WRF-ARW; Skamarock et al. 2005) version 3.8.1. The model setup was similar to previous OLYMPEX studies that were found to be generally consistent with observations (Conrick et al. 2018, Conrick and Mass 2019). Figure 4.1 shows the 36-12-4-1.33 km model configuration with 51 vertical levels. The innermost 1.33 km domain is centered over the Olympic Peninsula. Model initialization and boundary conditions were driven by the 0.25° Global Forecast System (GFS) gridded dataset. The 36-km grid boundaries were nudged every 3 hours using either the GFS initialization (00, 06, 12, and 18 UTC) or the 3-hour forecast (03, 09, 15, and 21 UTC). Table 4.5 contains additional parameterization choices. The most noteworthy choice is the use of the bulk Thompson microphysics scheme (Thompson et al. 2008) which was chosen because it was shown to most accurately predict liquid water content (LWC) during OLYMPEX (Conrick and Mass 2019).

4.3.2 *Case Selection*

To facilitate interpretation of OLYMPEX surface and radar observations from Chapter 3, this study uses cases from the same set of DC-8 aircraft missions detailed in section 3.3. Table 4.6 shows the cases, model initialization times, and model analysis times for the 6 cases in this study. Three prefrontal and three postfrontal cases are considered. The 3 December case was sampled for a shorter period than the other cases and is therefore slightly underrepresented in the analysis. The

storm sector paradigm and the rationale for examining the sectors separately is described in Medina and Houze (2007) and Chapter 1. Postfrontal cases were poorly resolved by the model and are not included. The analysis start and end times were set according to the OLYMPEX DC-8 flight times (Table 3.2). The WRF model output was saved every hour and output from the 1.33 km domain was composited to generate Contoured Frequency by Altitude Diagrams (CFADs) of simulated radar reflectivity and maps of various dynamic and microphysical parameters.

4.4 Model Evaluation using Aircraft and Surface Observations

4.4.1 *Reflectivity CFADs*

Before evaluating model microphysical output, it is important to verify that the model is producing precipitation structures that are consistent with observations. In Chapter 3, CFADs of radar reflectivity from the Airborne Precipitation and Cloud Radar Third Generation (APR-3) were created by dividing the flight legs into five geographic regions: ocean, coast, windward, high terrain, and lee side. Figure 4.2 shows the corresponding geographic regions used to partition the WRF CFADs. These regions are nearly identical to the APR-3 regions but have the advantage of uniform sampling at 1.33 km horizontal resolution instead of being preferentially biased along the typical APR-3 flight pattern (Figure 3.2). To allow quantitative comparison between the APR-3 and WRF, the WRF CFADs were constructed as in Section 3.2.1 with the same bin spacing and normalization by maximum bin. The shaded terrain outline in Figure 4.2 also illustrates the pattern of smaller, sub-barrier scale ridges and valleys that are superimposed on the broader barrier-scale dome shape of the Olympic Mountains. Figure 4.2

Figure 4.3 shows a comparison between the APR-3 and WRF CFADs for the windward region only. The APR-3 panels (top row) are reproduced from Figures 3.7d and 3.13d. Many of the key

features in the observations are reproduced by the model. Both prefrontal CFADs show a narrow range of reflectivities corresponding to homogeneous stratiform precipitation. However, simulated reflectivity is overestimated by 5-10 dB, a behavior that was also noted in atmospheric river-type storms in California (Jankov et al. 2009). The observed and simulated warm sector CFADs are both broader than the prefrontal sector, although the WRF CFAD is smoother as a consequence of the larger sample size. The WRF CFAD also locates the warm sector mode in the lower levels, a reflection of low-to-mid level enhancement of precipitation. The observations also suggest a stronger brightband and stronger below-brightband precipitation than the simulated reflectivity suggests, an indication that WRF is identifying but underestimating low-level warm processes.

Figure 4.4 examines the nature of windward precipitation enhancement by taking the CFAD difference between the windward side (Figure 4.3) and the ocean (not pictured). The APR-3 panels (top row) are reproduced from Figures 3.8b and 3.14b. WRF captures the area of mid-level ice enhancement in both prefrontal and warm sectors, although it is somewhat underestimated in prefrontal sectors. The greatest disagreement is the lack of WRF low-level enhancement in warm sectors below the melting level. In general, the qualitative agreement in precipitation structures between WRF and observation is quite impressive given the complexity of terrain-induced enhancement processes.

4.4.2 *Surface Precipitation Rate*

Figure 4.5 shows the average WRF surface precipitation rate in the prefrontal and warm sector cases. These maps are computed over the same time period as the rain gauge observations in Figure 3.12a-b. WRF correctly resolves the major differences in precipitation patterns between prefrontal and warm sectors. Prefrontal precipitation rates are generally light, < 5 mm h^{-1}, with slight enhancement over the coast and windward side. Warm sectors have lighter precipitation rates at

the coast than the prefrontal sector and a rapid increase to > 10 mm h^{-1} rain rates over the windward ridges and southwestern part of the high terrain. Lee side precipitation rates are greater in the warm sector than the prefrontal sector. The fine scale ridge-valley gradients in precipitation rate simulated by WRF are also consistent with the dense network of gauge observations around Lake Quinault in Figure 3.12b.

The gridded model output was also compared to the point observations in Figure 3.12a-b. A few general trends are relevant for interpreting the WRF output in the rest of this chapter. In prefrontal sectors, WRF generally overestimates precipitation rates by 0.5-2 mm h^{-1} over terrain, possibly due to the excessive ice production noted in the CFADs (Figure 4.3). In warm sectors, WRF differed from gauge observations by up to ±3 mm h^{-1} at a few low-to-mid elevation windward sites. Even small differences in precipitation rate can become significant when considering the long duration of these storm systems. The source of these disagreements is uncertain but possibly related to the model having difficulty resolving the complexity and greater intensity of warm sector precipitation. The overall consistency of WRF-observation precipitation patterns adds confidence that WRF dynamical and microphysical fields described in the following sections depict an accurate representation of these storms.

4.5 Synoptic and Dynamical Composites

4.5.1 *Flow and Stability*

Figure 4.6 shows model composite surface and 500 hPa maps and Figure 4.7 shows model composite moist static stability (N_m^2). All model composites in this study are generated by averaging the hourly WRF output at the times in Table 4.6. The moist static stability was calculated by determining N_m^2 following Durran and Klemp (1982) over interpolated vertical layers at 0.25

km spacing and averaging over the 0.5 – 2.0 km layer. As in previous chapters, we found that N_m^2 was the best indicator of whether flow would ascend over the dome-shaped Olympic Mountains or be prone to low-level blocking or deflection upstream of the barrier.

The 500 hPa composites (Figure 4.6a,b) show that on average the cross-barrier flow was from the west-southwest in both prefrontal and warm sectors. The composites obscure some case-to-case variability (see Section 3.4), as both sectors can contain more southerly or westerly mid-level flow (Figure 3.3). The 500 hPa flow speed over terrain was slightly stronger (5-10 kt) in warm sectors and the heights were lower on average in prefrontal sectors. The surface maps (Figure 4.6c,d) show more significant differences between the two sectors. Prefrontal sectors had more southerly flow with an offshore-directed pressure gradient. There is also strong evidence of flow deflection on the south and southwest sides of the Olympic Mountains where the 10-m winds were east to southeasterly. Warm sectors had a weak onshore pressure gradient and southwesterly 10-m winds at the coast and over the windward slopes. There is no indication of flow blocking or deflection in surface flow upstream of the barrier.

Figure 4.7a shows stably stratified low levels upstream of the Olympic Mountains in the prefrontal sector, especially over land. Similar to the 10-m flow, the 925 hPa flow shows indications of deflection around the barrier on the southwest side corresponding to the region of greatest stable stratification. Warm sectors (Figure 4.7b) are closer to moist-neutral as N_m^2 was between 0 and 0.25 x $10^{-4}\ s^{-2}$ upstream of the Olympic Mountains. The 925 hPa flow is nearly uniform from the southwest with no indication of flow deflection on the windward side.

4.5.2 *Vertical Velocity and Relative Humidity*

Given the considerable differences in low-level flow and stability between different storm sectors detailed in the previous section, it is expected that regions of ascent and descent will differ

in location and magnitude between prefrontal and warm sectors. Figure 4.8 shows the average vertical velocity in the lowest 1.0 km above terrain. Similar results were obtained using deeper layers. Prefrontal sectors (Figure 4.8a) had couplets of ascent and descent on windward ridges. The couplets correspond to the low-level flow which was aligned normal to the ridges (Figure 4.6). These mountain waves were excited by forced ascent across a series of windward ridges in a stably stratified environment. A second set of mountain waves is apparent over the high terrain with lee waves extending downstream of terrain. These waves were aligned with the cross-barrier flow (700 hPa), perpendicular to the waves over the windward ridges. This wave pattern is similar to the waves over the Oregon Cascades detailed in Fig. 19 of Garvert et al. (2007). Minder et al. (2008) studied similar small-scale waves on the windward side of the Olympic Mountains. Examination of each model timestep (not shown) revealed that this stationary wave pattern was observed throughout the three prefrontal cases with only minor variations.

Warm sector vertical velocities (Figure 4.8b) show much less indication of small-scale waves associated with ridges on the windward side. Ascent was widespread across both the coastal foothills and windward ridges. There were no corresponding regions of descent. The southwesterly low-level flow was orientated along the windward ridges, allowing for broader ascent compared with the ascent/descent couplets that occur when the flow is oriented across the ridges. Additionally, the moist-neutral upstream environment further favored broad lifting over the barrier, with enhanced regions of ascent on windward ridges. The wave response over the high terrain-lee side is similar to prefrontal sectors, consistent with the similar direction and velocity of the cross-barrier flow in Figure 4.6b. In general, the high terrain contained descent on the lee of the higher ridges and localized forced ascent over a few ridges and lee waves downstream of the barrier.

Figure 4.9 shows the composite WRF relative humidity (RH) over the same 1.0 km layer above terrain as the vertical velocities. With widespread precipitation ongoing, the low levels upstream of the barrier tended to be nearly saturated (>95% RH) in both prefrontal and warm sectors. Prefrontal sectors have a pattern of saturation and drying on the smaller-scale windward ridges that corresponds with the regions of ascent and descent in Figure 4.8a. Areas of near 100% RH were confined to the ridges. In contrast, warm sectors were nearly saturated everywhere on the coast and windward slopes, except for a few isolated pockets such as the interior Quinault Valley. In the next section, we demonstrate that these profound differences in low-level vertical motions and moisture have major implications for the microphysical precipitation processes in these regions.

4.6 MICROPHYSICAL COMPOSITES

Figure 4.10 shows composites of the 0-5 km average cloud water mixing ratio and Figure 4.11 shows composites of the 0-8 km average precipitation-sized hydrometeor (rain + graupel + snow) mixing ratio. The pattern of small-scale mountain waves in prefrontal sector (Figure 4.8a) appears to have been responsible for only a minor increase in cloud water on windward ridges (Figure 4.10a). The regions of descent and drying on the lee of windward ridges are responsible for local reductions in cloud water, preventing any net progressive increase in precipitation as flow moves over successive ridges. Figure 4.11a does not show any increase in precipitation-sized hydrometeors on the windward ridges. Instead, the precipitation-sized hydrometeor mixing ratio was broadly elevated on the southern (i.e. windward) side of the Olympic Mountains. Because of lower melting levels in prefrontal cases, snow was the dominant precipitation-sized species in prefrontal cases with low melting levels. The lack of localized increases in mixing ratios suggests that barrier-scale lift was controlling the precipitation enhancement in these prefrontal cases. The

greatest precipitation-sized hydrometeor mixing ratios were displaced upstream of the barrier, likely a consequence of broader ascent over low-level stable air (Figure 4.7, Houze et al. 2001, James and Houze 2005). Precipitation rates were broadly enhanced over the windward slopes as a consequence of these ice-dominated processes (Figure 4.5a) with a negligible contribution from processes over localized small-scale ridges.

The distribution of cloud water is remarkably different in warm sectors (Figure 4.10b). The greatest cloud water enhancement was located on the upstream side of all major windward ridges, but cloud water was also elevated at lower elevations at the front of windward valleys (except in the interior Quinault valley). Additionally, enhanced cloud water was widespread over the coastal foothills upstream of the main barrier. The quantity of cloud water produced was impressive given the foothills are generally less than 200 m high. Figure 4.11b shows that the maximum in precipitation-sized hydrometeors occurred over the high terrain, downstream of the maximum in cloud water on the lower-windward slopes. The production of precipitation-sized hydrometeors (predominantly snow) was tied to the barrier as a whole. Maxima in cloud water were closely tied to small-scale terrain features, but a broader increase in cloud water was apparent across the entire coast and windward regions.

The initial formation of cloud water along the coastal foothills did not result in an immediate increase in precipitation rate at the coast (Figure 4.5b). Instead, the model depicts a smooth gradient of increasing precipitation rate up to the windward slopes, with a significant increase in precipitation rate over the lower-windward ridges. Areas of high precipitation rates on the lower-windward slopes were always associated with high concentrations of cloud water, but the presence of elevated cloud water alone was not a sufficient condition for enhanced precipitation rates. Disdrometer and gauge observations on the lower-windward slope (Prairie Creek, Figures 2.13

and 3.10c-d) found a prevalence of large concentrations of small drops, suggesting that the cloud drops are capable of self-collecting to precipitation size and falling out. The extent to which collection by ice-initiated drops assists in producing precipitation is difficult to assess in realistic model simulations. Given the tendency of various WRF microphysical schemes to overestimate median drop sizes (D_o) and underestimate the normalized intercept parameter (N_w) in two warm OLYMPEX cases (Conrick et al. 2018), it is hypothesized that warm precipitation processes are more important than WRF implies.

4.7 Vertical Cross-Sections

Figure 4.12 and Figure 4.13 show representative cross-sections from a prefrontal case (1100 UTC 02 December 2015) and a warm sector case (1700 UTC 08 December 2015). These times were chosen to be within one hour of the representative APR-3 cross-sections from Chapter 3 (Figure 3.6a,c). The cross section is taken southwest-northeast along the red line in Figure 4.2, bisecting the Quinault Valley directly over Lake Quinault. The cross-sections are useful for assessing the vertical depth of the terrain-induced vertical velocity and hydrometeor perturbations. The prefrontal reflectivity field (Figure 4.12b) is remarkably consistent with the APR-3 cross-section. The prefrontal vertical velocity field shows a broad area of ascent upstream of the barrier with corresponding enhancement to both cloud water and precipitation-sized hydrometeors. The cross-section is also cutting through the stronger ascent associated with the small-scale mountain wave in the Quinault Valley (Figure 4.8a). The small-scale mountain wave response over terrain resulted in small perturbations in cloud water that appear to be inconsequential relative to the barrier-scale enhancement upstream. The “rain shadow” region in the lee is a consequence of an impressive downslope winds and lee wave formation which resulted in drying throughout the depth of the precipitating cloud.

The warm sector example reflectivity field (Figure 4.13b) is also consistent with the APR-3 cross-section. Broad lift over the coast was responsible for a significant increase in cloud water in the lowest 2 km. Because the incoming air contains more water vapor and is closer to saturation than the prefrontal sector (Figure 4.9b), only modest ascent is required to produce considerable quantities of cloud water. Over the Quinault Valley and windward slopes, there was a deeper cloud water perturbation extending above the ~2.5 km melting level, with a corresponding increase in rain water below the bright band. It is likely that WRF is underestimating the rate that this cloud water is being converted to rain water (Conrick et al. 2018), but it is clear that warm precipitation processes are the dominant enhancement signal on the lower-windward slopes. The high terrain (60-80 km along the cross-section) has a better juxtaposition of enhanced ice and cloud water, suggesting that collection of cloud water by ice-generated hydrometeors may be more prevalent than the lower-windward slopes. A deep region of descent was located directly over the high terrain with lee waves extending downstream of the barrier. The reflectivity and hydrometeor mixing ratio in the ice layer remained elevated well downstream of the descent, confirming that spillover of the deep ice layer formed upwind is the primary mechanism for precipitation reaching the lee side in warm sectors.

4.8 Discussion and Conclusions

This chapter builds on previous observational studies (Chapters 2 and 3) by using realistic WRF simulations of three prefrontal and three warm sector cases to gain additional insights into the dynamical and microphysical processes that modify precipitation over a coastal mountain range. Simulated reflectivity and microphysics fields successfully replicated key features from the observations, allowing the model to be confidently used to examine additional features of terrain-induced precipitation modification.

The main finding of this study was the predominance of barrier-scale processes in producing the observed pattern of precipitation enhancement. In prefrontal sectors, the modest increase precipitation rate was ultimately driven by ascent over a stably stratified layer upstream of the barrier, enhancing mid-level ice processes. A pronounced pattern of standing mountain waves over the windward slopes was ultimately inconsequential in enhancing precipitation on the scale of individual ridges. A similar lack of enhancement on windward ridges under low-Froude number (blocked) conditions was observed by Medina and Houze (2003) and shown in idealized models by Colle (2008). In this study, the modest condensation/deposition and subsequent leeside evaporation on small-scale ridges occurred on too short of spatial scales to appreciably increase precipitation. In warm sectors, widespread ascent of moist air produced a broad region of enhanced cloud water across the coast and windward regions. The heaviest precipitation rates were closely tied to further ascent over the windward ridges and additional localized condensation. Ice production did not appear to be affected by the small-scale windward ridges and was instead enhanced broadly on the barrier-scale over the interior high terrain.

A second major finding of this study was the importance of the coastal foothills in producing cloud water upstream of the main topographic barrier. In warm sectors with moist-neutral upstream stability, broad ascent over the coastal region may give the cloud water additional time to self-collect and form into precipitation-sized hydrometeors. Particle size observations in Chapter 3 show that these cloud drops are capable of reaching precipitation size and falling out at the Fishery site located in the near-coastal lowlands. While the lower-windward site Prairie Creek site experienced a larger median drop size and higher precipitation rate, the normalized drop concentrations were still much higher than the prefrontal sector, which was dominated by ice processes. In addition to the moist-neutral static stability, the high melting level, high moisture

content environment undoubtedly assisted in promoting warm rain processes, which have been shown to be especially efficient at enhancing precipitation on small-scale windward ridges (Minder et al. 2008; Colle 2008).

In order to isolate the prefrontal and warm sector processes and avoid the inexact model timing of frontal passages, this study considered a limited set of cases that corresponded to surface and aircraft observations. While the realistic model simulations are helpful for interpreting field campaign observations, model sensitivity tests of various kinematic and thermodynamic parameters would help broaden the applicability of this study. The transitional period between prefrontal and warm sectors and the difference between warm and occluded front passages both deserve additional attention. Chapter 2 demonstrated in a case study that warm precipitation processes gradually increase in importance as warm fronts approach and Purnell and Kirschbaum (2018) conducted sensitivity experiments relating the degree of blocking to the height of the frontal inversion layer. Further examination of warm and occluded frontal passes from a microphysics perspective may lend additional insight into means by which warm and ice microphysics processes combine to produce the observed patterns of precipitation enhancement.

4.9 TABLES AND FIGURES

Table 4.5. WRF parameterization choices used in this study.

Parameterization	**Configuration**	**Reference**
Microphysics	Thompson	Thompson et al. (2008)
Land Surface	Noah-MP	Niu et al. (2011)
Radiative Transfer	RRTMG	Iacono et al. (2008)
Cumulus	Grell-Freitas	Grell and Freitas (2014)
Boundary Layer	Yonsei University	Hong et al. (2006)

Table 4.6. Cases, model initialization times, and model analysis times used in this study.

Case	Category	WRF Initialization time	Analysis Start	Analysis End	# WRF hourly timesteps used
2015 Dec 1	Prefrontal	1200 UTC Dec 1	2100 UTC Dec 1	0200 UTC Dec 2	6
2015 Dec 5	Prefrontal	0000 UTC Dec 3	1400 UTC	1900 UTC	6
2015 Dec 12	Prefrontal	0000 UTC Dec 12	1600 UTC	2200 UTC	7
2015 Nov 13	Warm Sector	1200 UTC Nov 12	1400 UTC	2000 UTC	7
2015 Dec 3	Warm Sector	0000 UTC Dec 3	1400 UTC	1700 UTC	4
2015 Dec 8	Warm Sector	0000 UTC Dec 8	1300 UTC	1900 UTC	7

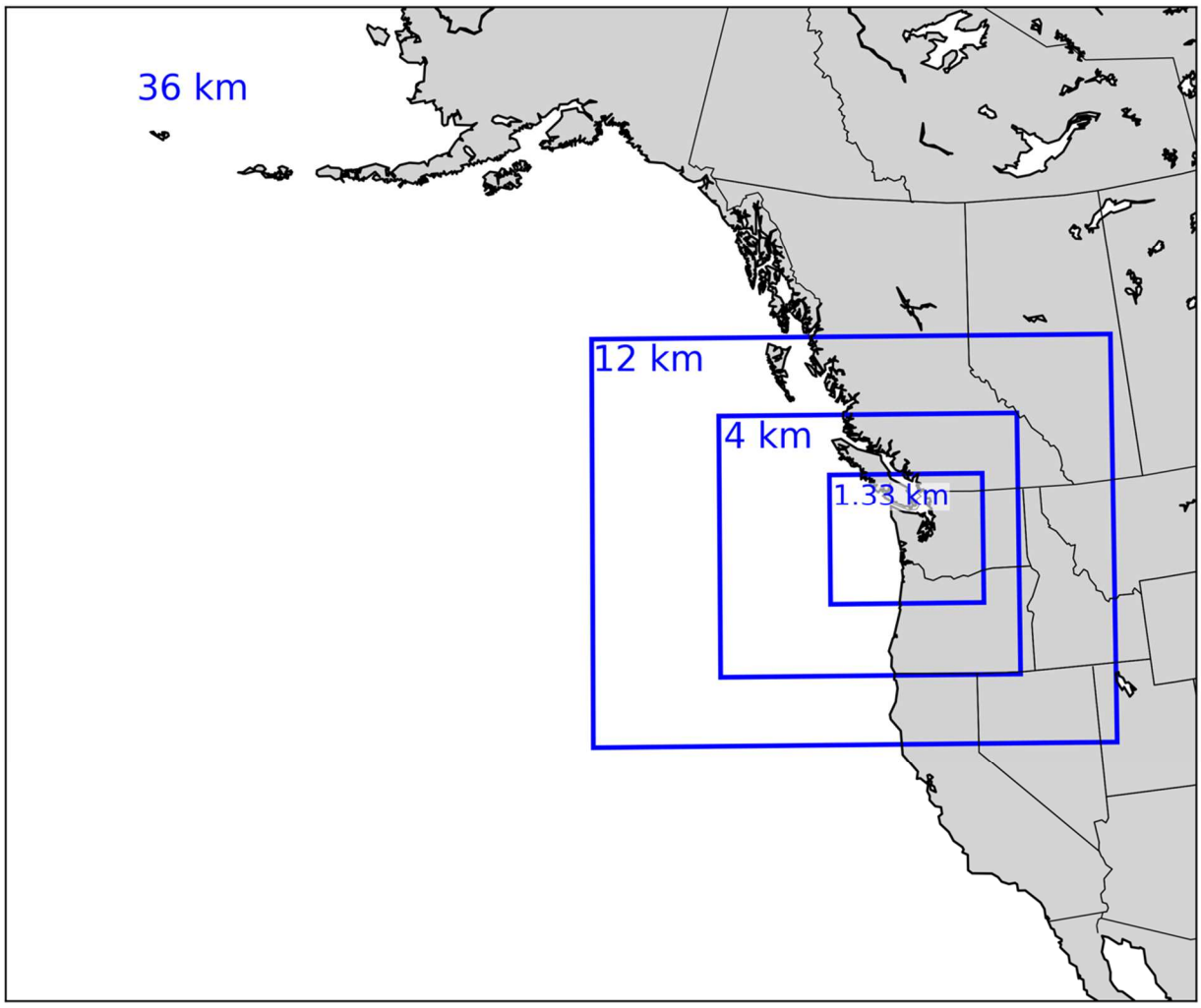

Figure 4.1. Map of the nested WRF-ARW domains used in this study. Labels indicate the resolution of the four domains.

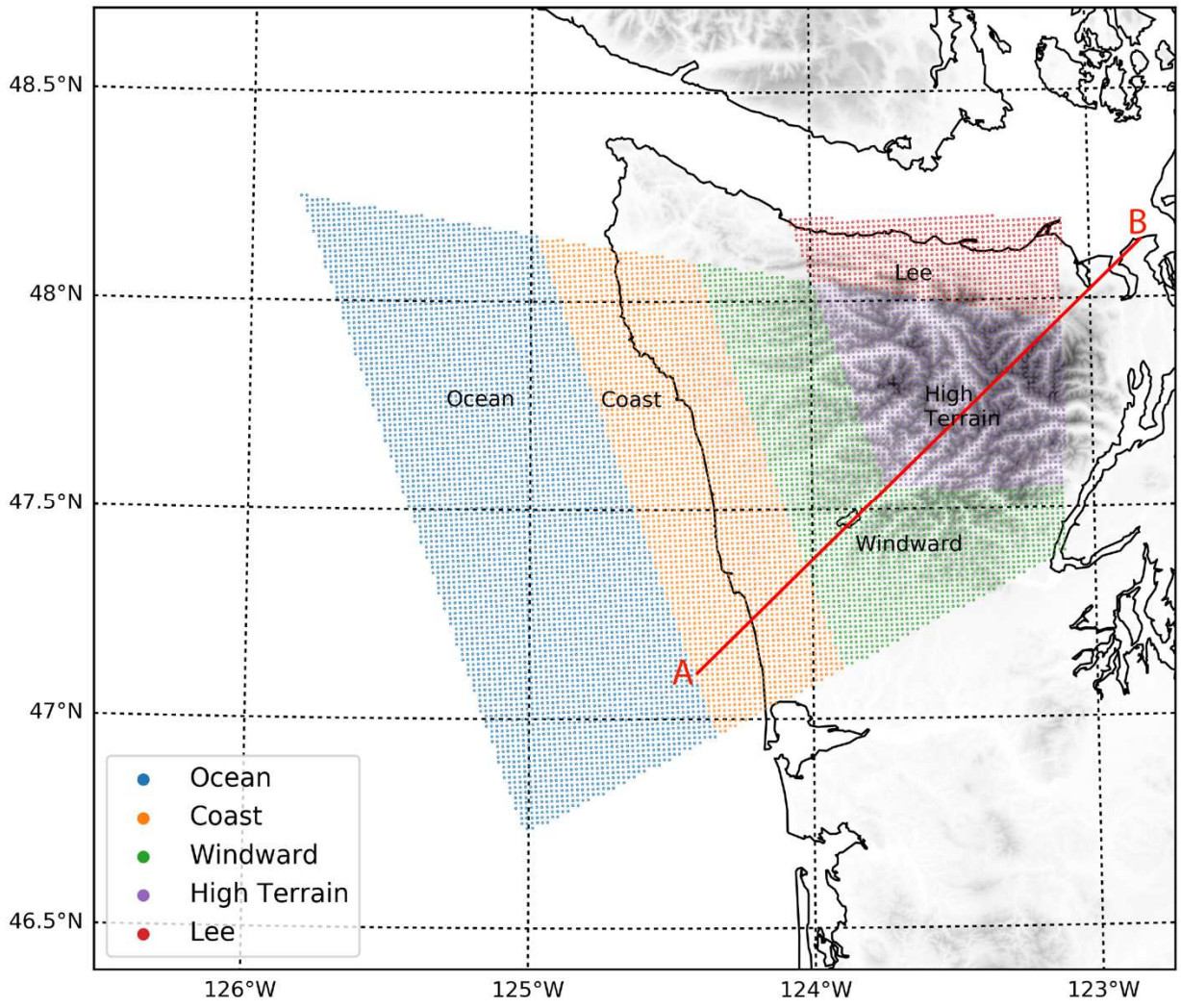

Figure 4.2. Map of the five geographic regions used in this study. The red line denotes a cross section used in Figure 4.12 and Figure 4.13.

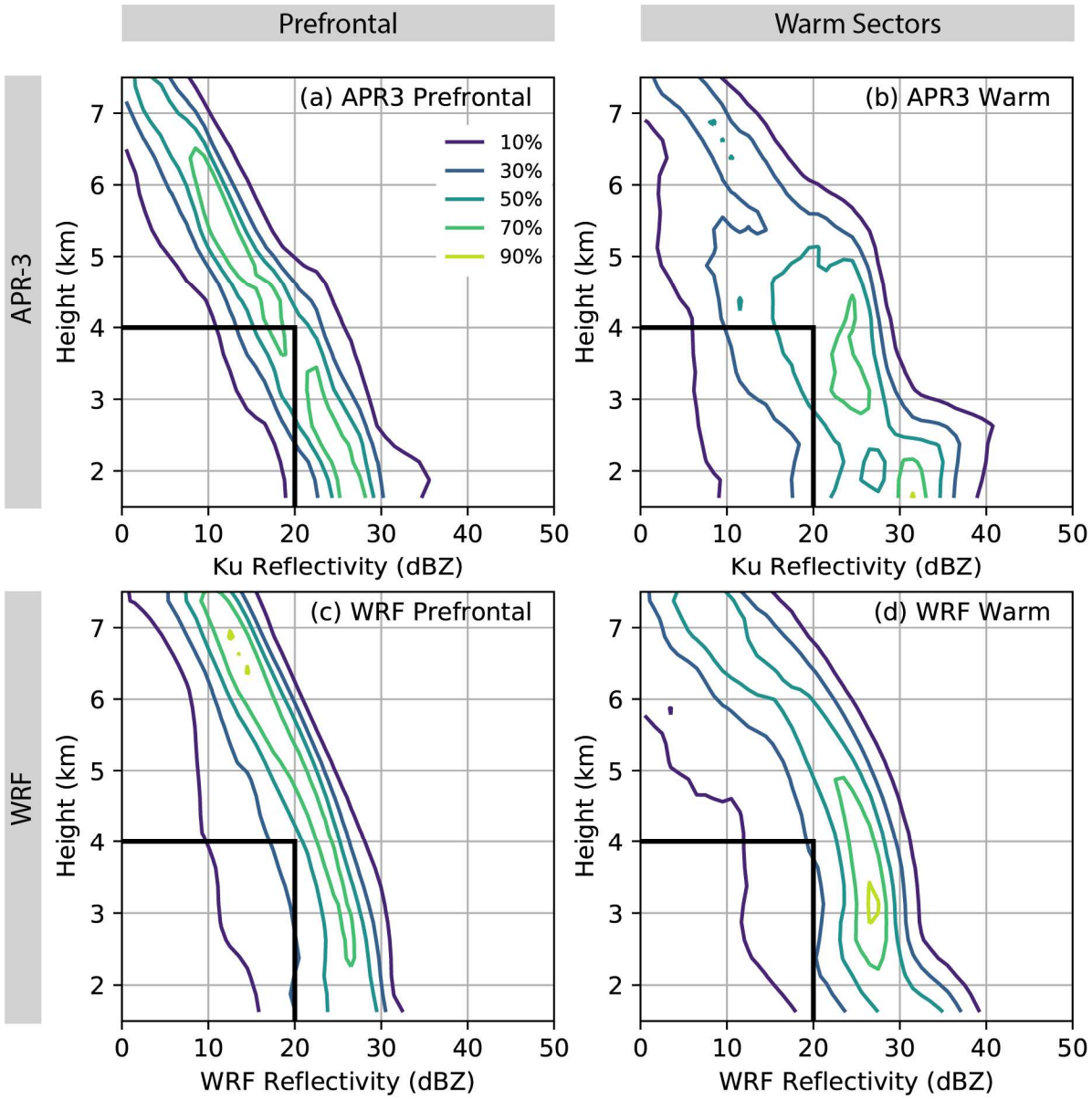

Figure 4.3. Normalized Contoured Frequency by Altitude Diagrams (CFADs) for the windward region (a) APR-3 prefrontal cases, (b) APR-3 warm sector cases, (c) WRF prefrontal cases, (d) WRF warm sector cases.

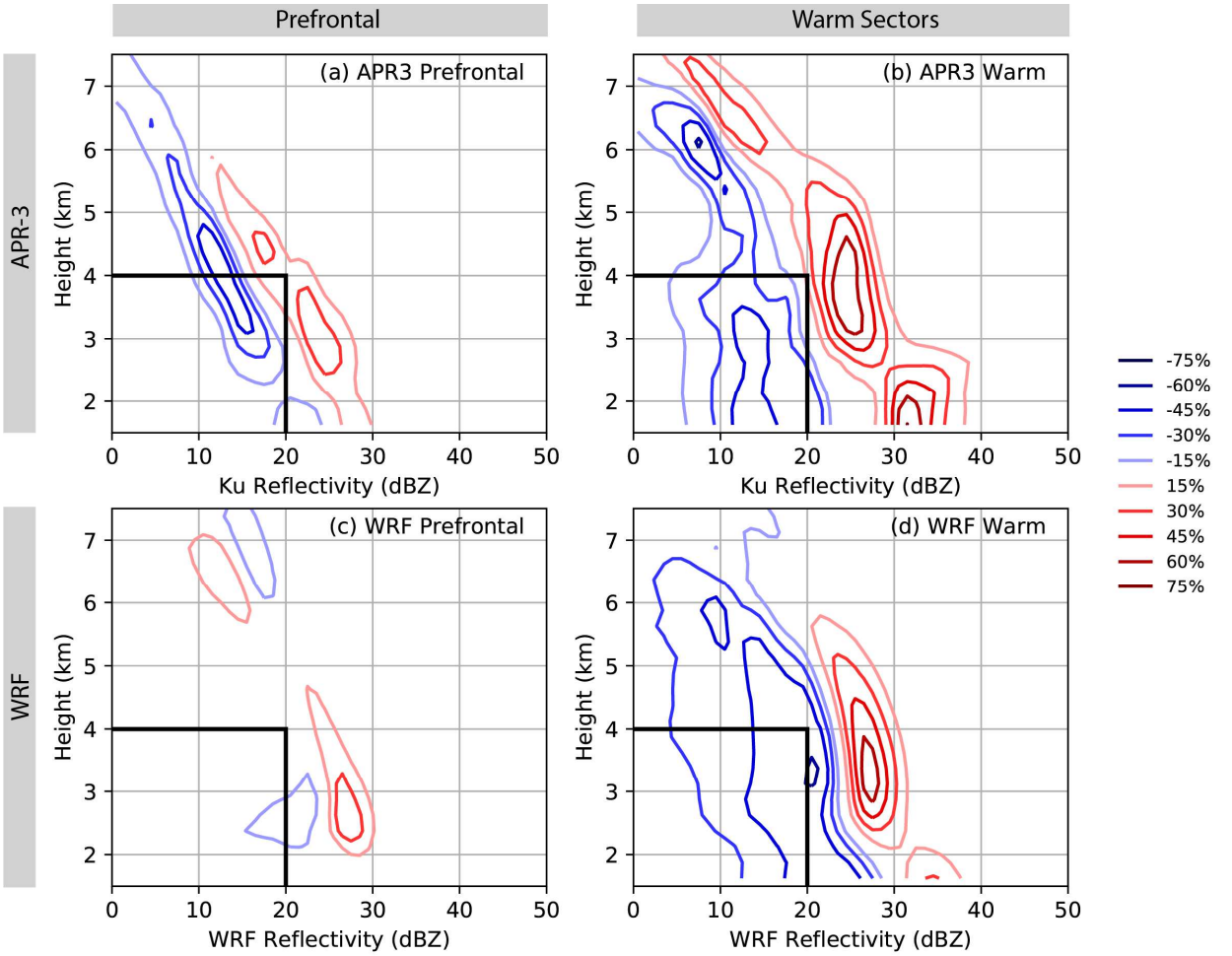

Figure 4.4. Difference CFADs computed by subtracting the ocean region from the windward region for (a) APR-3 prefrontal cases, (b) APR-3 warm sector cases, (c) WRF prefrontal cases, and (d) WRF warm sector cases.

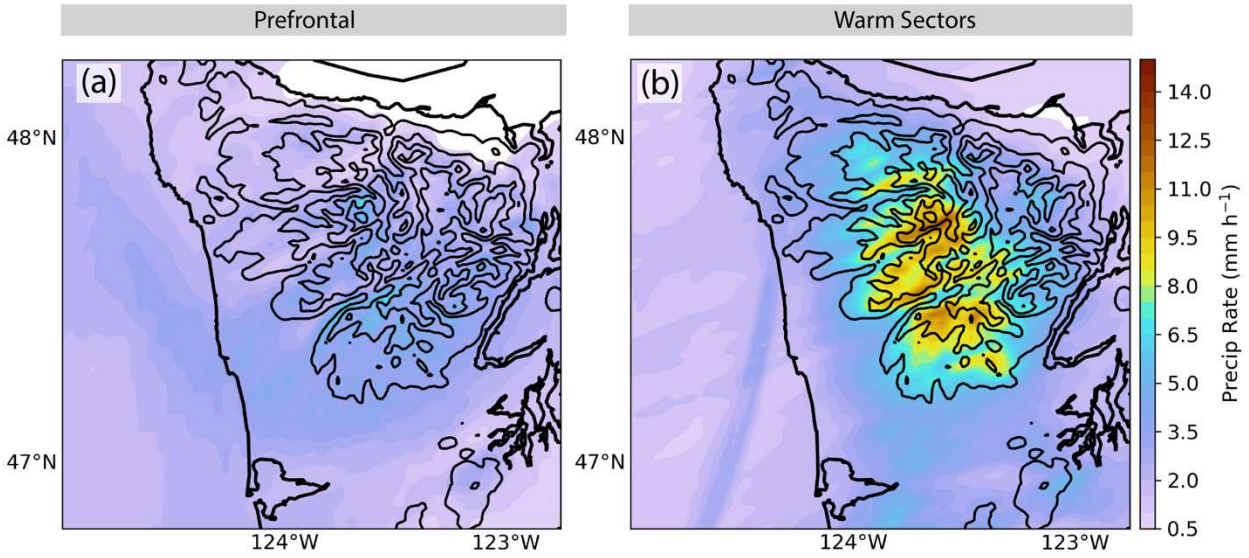

Figure 4.5. Average WRF surface precipitation rate (mm h^{-1}) in (a) prefrontal and (b) warm sector events.

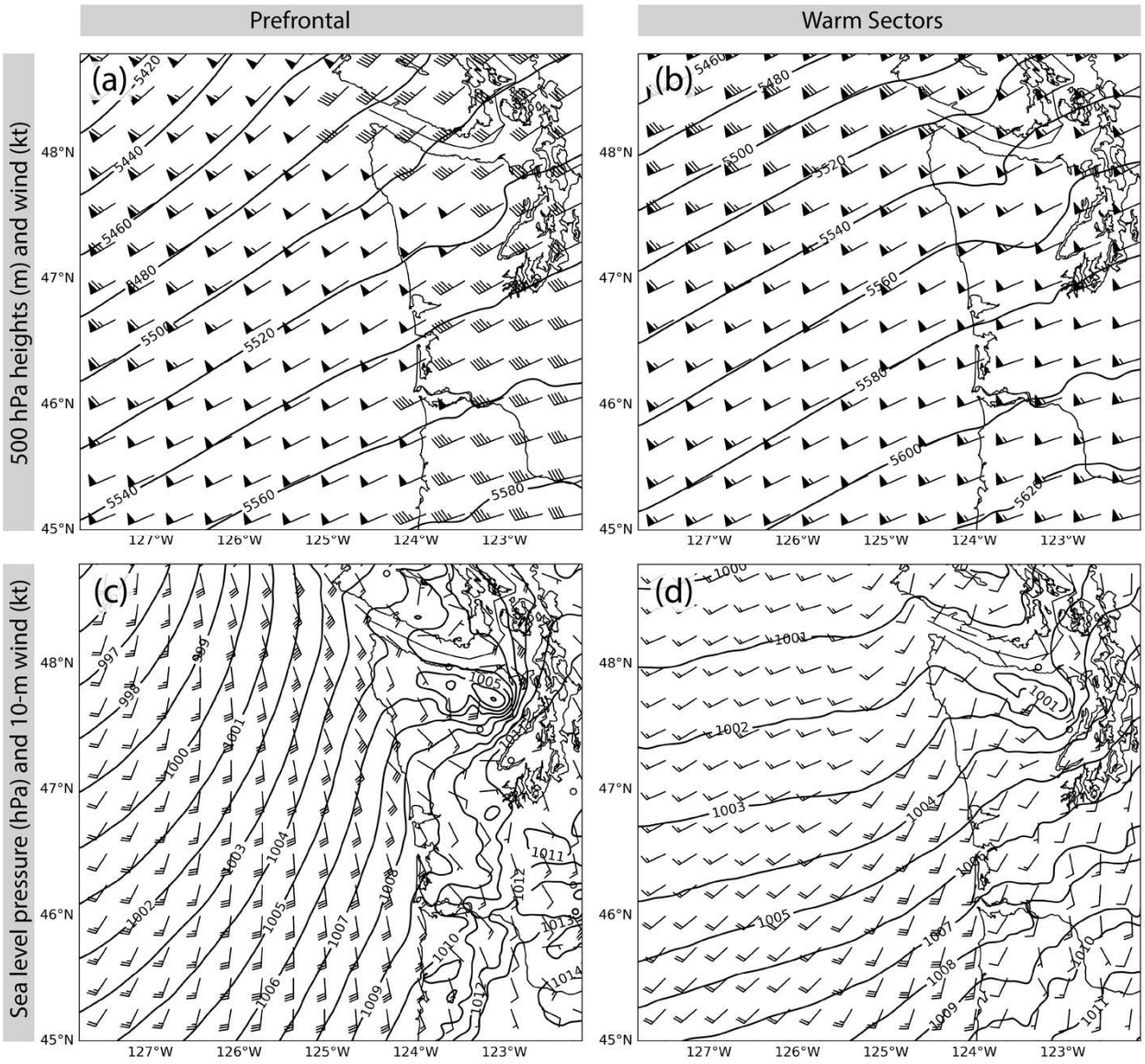

Figure 4.6. Top row: composite WRF 500 hPa height (m, contours) and wind (kt, barbs) for (a) prefrontal and (b) warm sectors. Bottom row: composite WRF sea level pressure (hPa, contours) and 10-m wind (kt, barbs) for (c) prefrontal and (d) warm sectors.

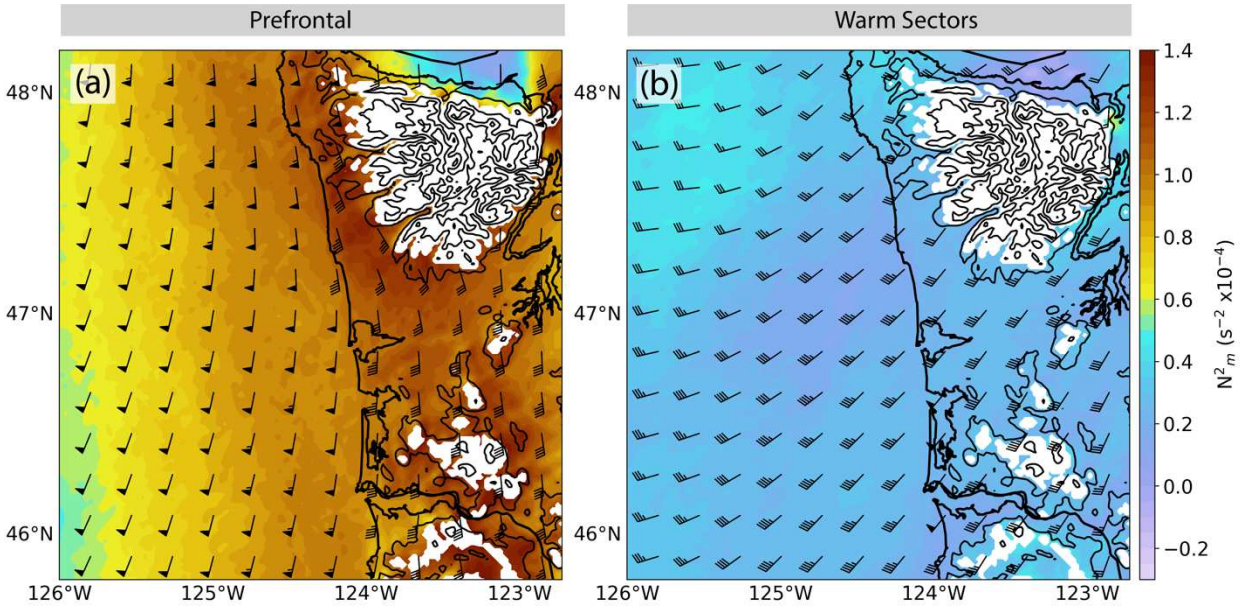

Figure 4.7. Composite WRF 0.5-2.0 km moist static stability (N_m^2 x 10^{-4}, contours) and 925 hPa wind (kt, barbs) for (a) prefrontal and (b) warm sectors.

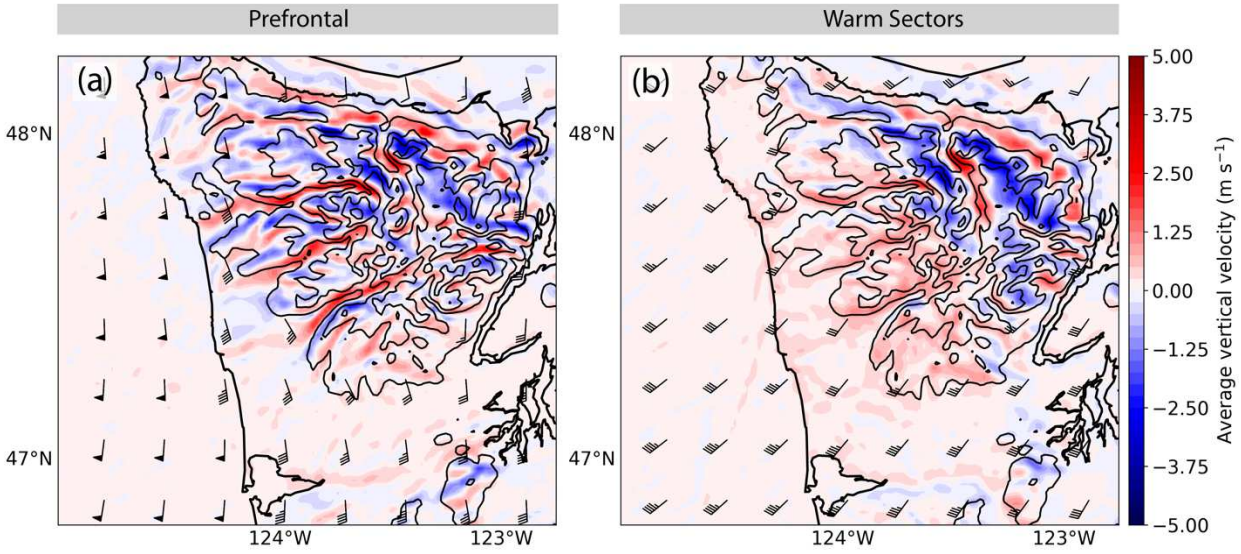

Figure 4.8. Composite WRF vertical velocity (m s^{-1}) averaged in the 1.0 km layer above terrain and 925 hPa wind (kt, barbs) for (a) prefrontal and (b) warm sectors.

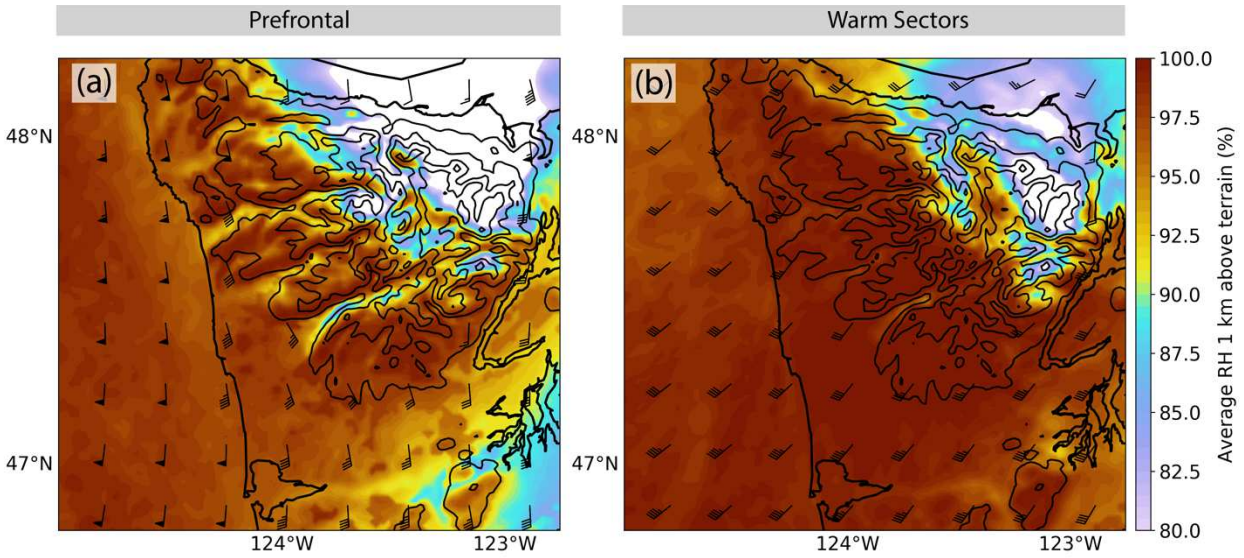

Figure 4.9. Composite WRF relative humidity (%) averaged in the 1.0 km layer above terrain and 925 hPa wind (kt, barbs) for (a) prefrontal and (b) warm sectors.

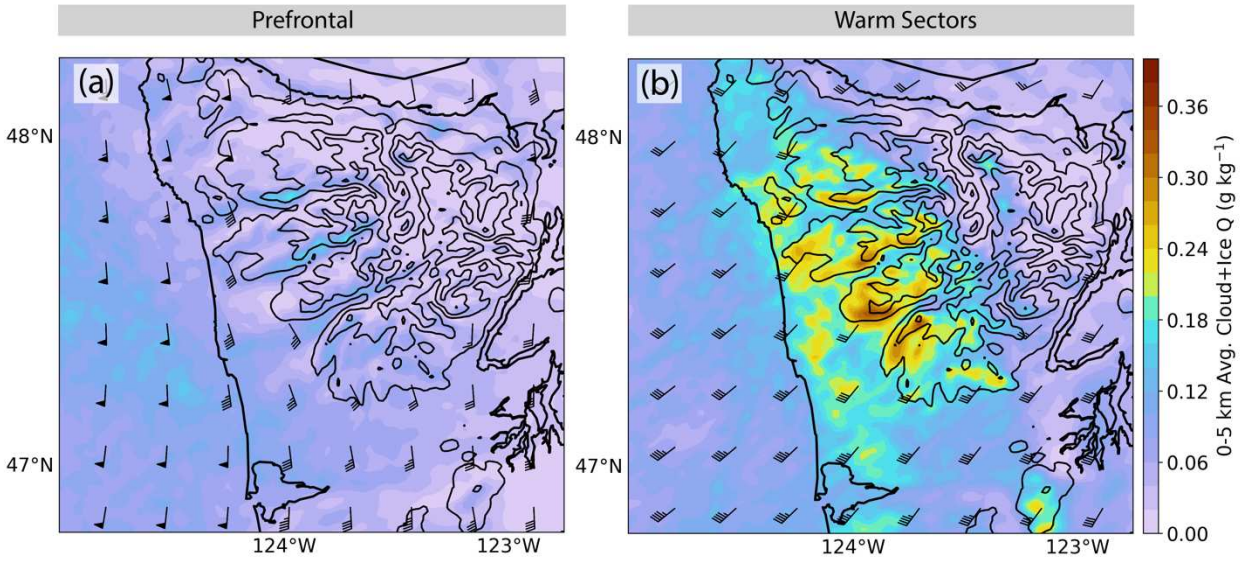

Figure 4.10. Composite WRF cloud water mixing ratio (kg kg^{-1}) averaged in the 0-5 km layer and 925 hPa wind (kt, barbs) for (a) prefrontal and (b) warm sectors.

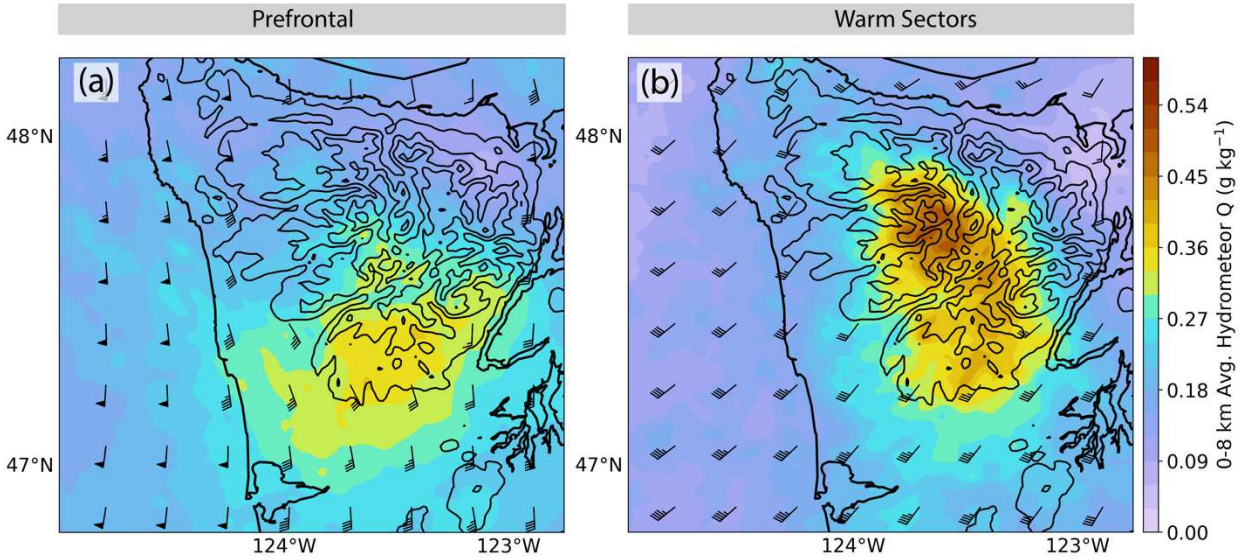

Figure 4.11. Composite WRF precipitation-sized hydrometeor (rain + graupel + snow) mixing ratio (kg kg^{-1}) averaged in the 0-8 km layer and 925 hPa wind (kt, barbs) for (a) prefrontal and (b) warm sectors.

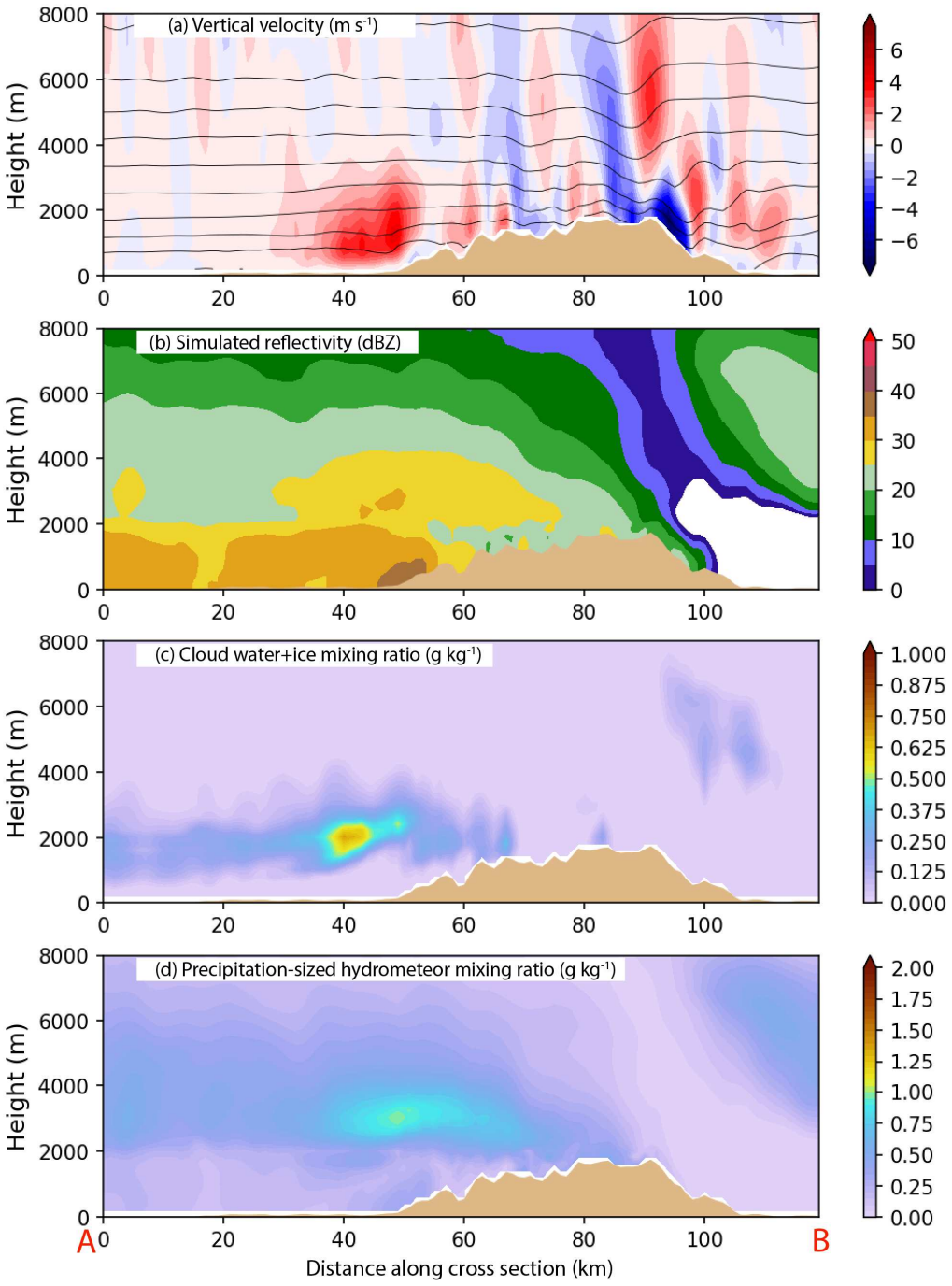

Figure 4.12. Representative prefrontal WRF vertical cross section taken SW to NE along the red line in Figure 4.2 taken at 1100 UTC 02 December 2015. (a) vertical velocity (m s^{-1}, color contours) and potential temperature (K, black contours), (b) simulated reflectivity (dBZ), (c) cloud water mixing ratio (kg kg^{-1}) and (d) precipitation-sized hydrometeor mixing ratio (rain + graupel + snow, kg kg^{-1}).

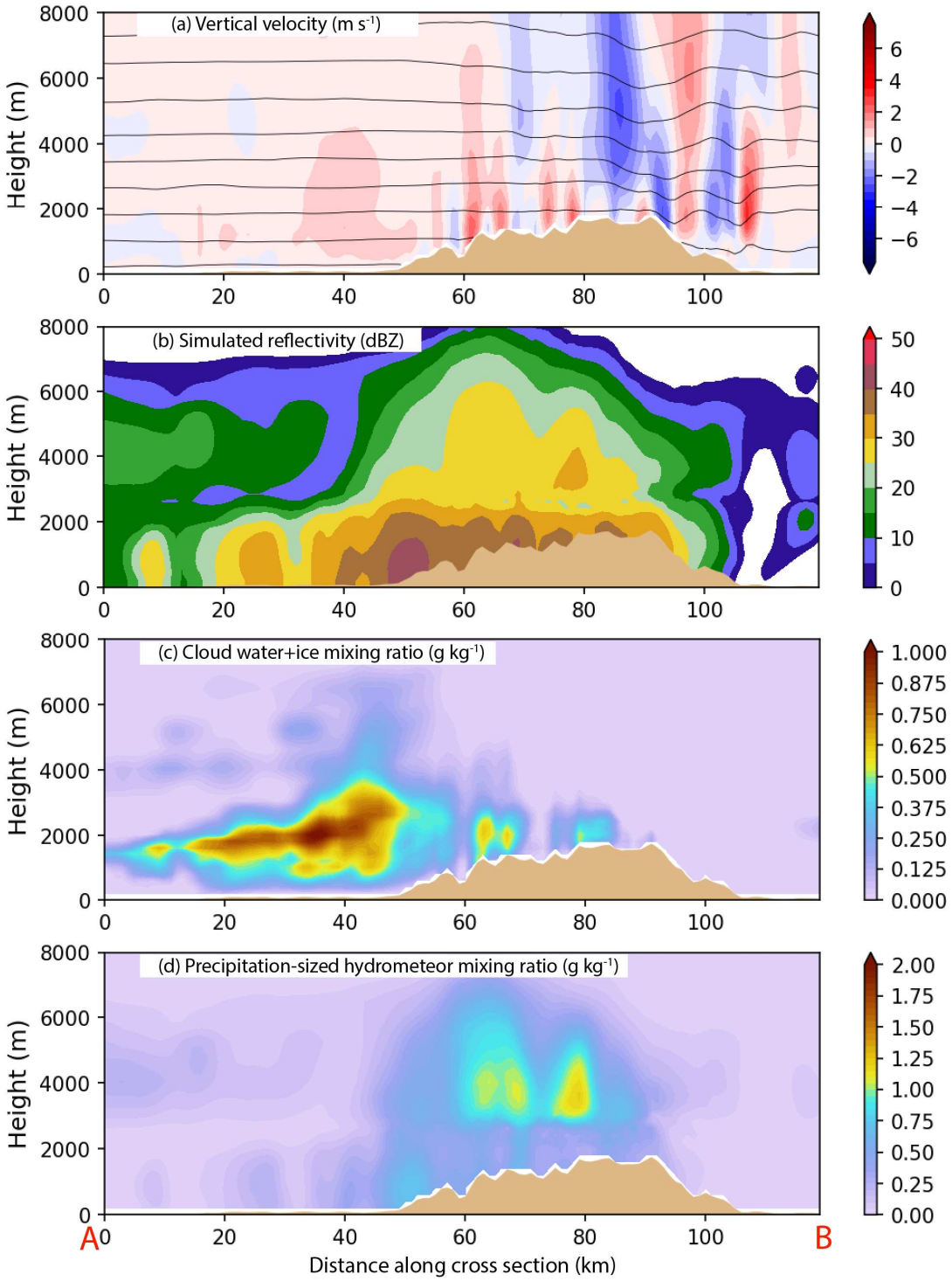

Figure 4.13. Representative warm sector WRF vertical cross section taken SW to NE along the red line in Figure 4.2 taken at 1700 UTC 08 December 2015. Panels as in Figure 4.12.

Chapter 5. OVERALL CONCLUSIONS

This study examined the relative roles of liquid and ice microphysical processes in modifying precipitation over west coastal mountain ranges. The OLYMPEX field campaign and realistic, high-resolution WRF runs provided complimentary perspectives on the key factors associated with terrain-induced precipitation processes. Structuring the analysis using a synoptic "storm sector" approach (Figure 1.1) proved to be a highly effective way of determining the likely modes of precipitation enhancement or lack thereof. The prefrontal, warm sectors, and postfrontal events had distinct synoptic-scale environmental conditions (flow, stability, and temperature) which were shown to exert significant controls over the flow response upon encountering complex terrain.

Figure 5.1 illustrates many of the key findings of Chapters 2, 3, and 4. This figure builds on the simpler version presented earlier to describe the findings of Chapter 2 (Figure 2.14). Figure 5.1a depicts precipitation structures during prefrontal conditions. These periods contain stably stratified low levels, low melting levels, and low-level flow that does not impinge directly on the Olympic Mountains barrier. A moderately deep stratiform cloud layer from the approaching storm is present over the Olympic Mountains with primary precipitation production in the ice layer above the melting level. The ice layer is slightly enhanced upstream of terrain due to lift over the stably stratified lower layer. Relatively small concentrations of larger drops fall from the stratiform cloud with minimal variance in space and time. There is modest enhancement of precipitation on the low- to middle-elevation windward slopes because there is minimal generation of cloud water or small raindrops at low elevations. Stationary mountain waves aligned across the smaller-scale windward ridges have a minimal impact on the overall precipitation pattern. Precipitation diminishes abruptly on the high terrain with a complete rain shadow in the lee.

The bottom panel (Fig. 15b) depicts precipitation structures during warm sectors when heavy precipitation is falling. These periods contain moist-neutral stratification at low levels and high melting levels. The unblocked large-scale flow is directed onshore at both upper and lower levels. The high moisture content of the onshore flow results in the rapid generation of cloud water as soon as the low-level flow begins lifting over the coastal foothills. Large quantities of small drops are formed by condensation and collision-coalescence as the flow continues to ascend moist-neutrally over the lower-elevation windward slopes, especially where lift is locally enhanced along windward ridges. Ice-initiated drops fall in variable quantities upstream of terrain. Directly over terrain the ice layer experiences deep enhancement. The strong cross-barrier winds advect some of these ice particles downstream to the lee side.

As a whole, this study demonstrates that the microphysical aspects of precipitation enhancement over the Olympic Mountains depends on a complex mix of warm low-level rain processes and upper level ice processes. The relative importance of these processes depends in turn on both the sector of the parent synoptic system and the location relative to the barrier. The greatest precipitation enhancement occurs on the windward slopes when both warm and ice processes are superimposed during the warm sectors of atmospheric river-type storms. The warm processes are aided by lift over the coastal foothills, granting additional time for cloud water to self-collect prior to reaching the windward slopes. The least precipitation enhancement occurs when the warm processes are absent. Processes on the scale of individual ridges are of secondary importance to the larger barrier-scale processes.

Lee side precipitation must overcome persistent descent on the downstream side of the higher windward ridges. Precipitation amounts in the lee were greater during warm sectors when there was a deep layer of ice-layer enhancement to advect downstream.

Several broad areas of future study can be identified from Figure 5.1. First, the postfrontal sector received relatively brief treatment in this dissertation and therefore is not included in the conceptual figure. The transformation that postfrontal convective cells undergo between ocean and the windward slopes is especially of interest (Section 3.5.3). The dynamic and microphysical origins of the deeper ice-layer enhancement over the high terrain in Figure 5.1b is also not well understood. Based on preliminary work (McMurdie et al. 2018; Chase et al. 2018), it is believed that the layer is sometimes but not always tied to terrain and that riming and aggregation are both enhancing ice processes. Further evaluation of triple-frequency APR-3 retrievals and dual-polarimetric radar data will be required to better understand this interesting feature. Finally, this study raises several interesting follow-up questions related to the efficiency of warm microphysical process rates. The observational results suggest that the enhancement of precipitation on the windward slopes is less dependent on ice processes than model-based studies (e.g. Purnell and Kirshbaum 2018) have suggested. Recent model verification studies (Conrick et al. 2018; Conrick and Mass 2019) further point to an underestimation of warm processes and overemphasis on ice processes in WRF microphysics schemes. Finally, terrain-modification numerical experiments could test the role of the coastal foothills in accelerating warm rain production over the windward slopes as hypothesized in Chapter 4.

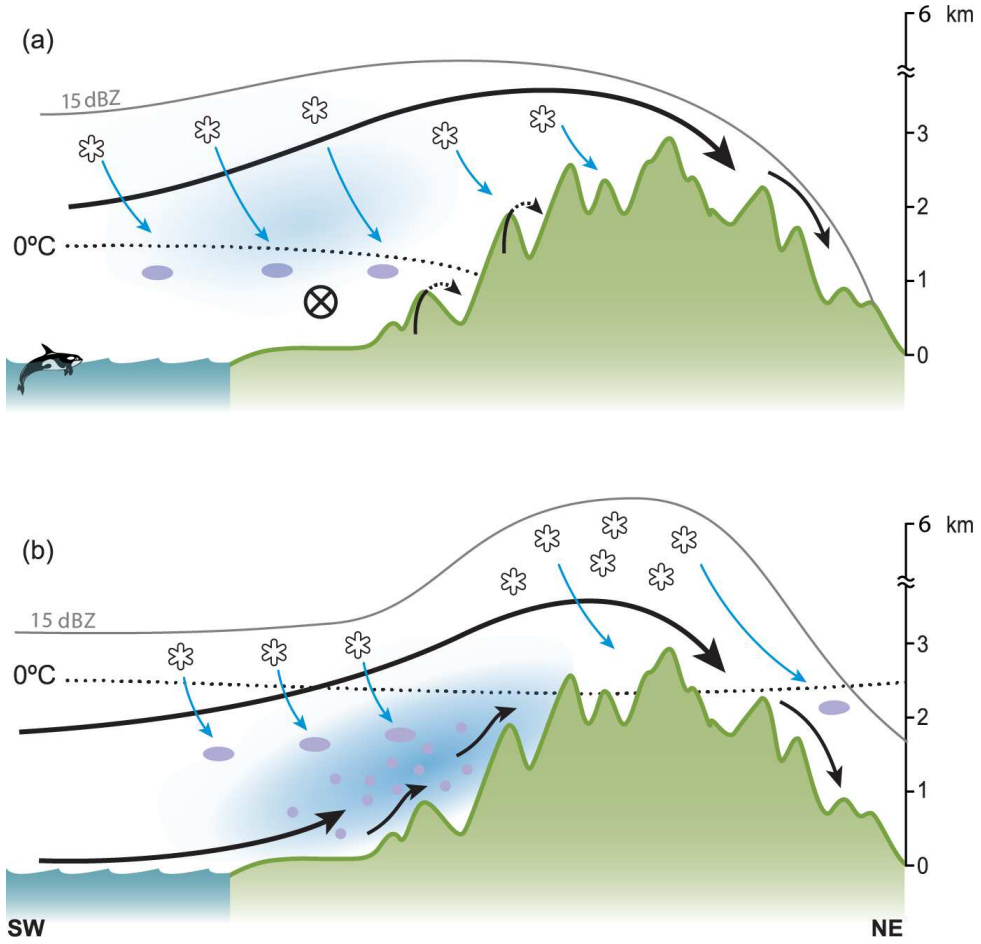

Figure 5.1. Conceptual cross-section diagrams depicting the two primary modes of precipitation enhancement the Olympic Mountains from southwest to northeast for (a) prefrontal and (b) warm sectors. Large black arrows represent the flow on the scale of the barrier. The circled X in panel (a) represents southeasterly flow perpendicular to the cross-section. Small black arrows represent flow across small-scale (~10 km) ridges in (a) and along small-scale ridges in (b). Blue arrows represent frozen hydrometeor trajectories. The gray line represents the average height of the 15 dBZ reflectivity contour (Figure 3.9). The blue shading represents regions of elevated cloud liquid water. Ellipses represent large raindrops formed from melted ice particles. Circles represent small raindrops formed by condensation and collision/coalescence. Snowflakes represent frozen condensate (mostly snow. The whale represents the author's excitement at reaching the end of dissertation writing.

BIBLIOGRAPHY

[1] Anders, A. M., G. H. Roe, D. R. Durran, and J. R. Minder, 2007: Small-Scale Spatial Gradients in Climatological Precipitation on the Olympic Peninsula. *J. Hydrometeor*., 8, 1068–1081.

[2] Asencio, N., Stein J., 2006: Origins of the reverse flow over the windward Alpine foothills of the MAP IOP 3 and IOP 8. *Q. J. R. Meteorol. Soc*. 132, 297–316.

[3] Atlas, D., R. C. Srivastava, and R. S. Sekhon, 1973: Doppler radar characteristics of precipitation at vertical incidence. *Rev. Geophys.*, **11**, 1–35.

[4] Barrett, B. S., R. Garreaud, and M. Falvey, 2009: Effect of the Andes Cordillera on Precipitation from a Midlatitude Cold Front. *Mon. Wea. Rev.*, 137, 3092–3109.

[5] Bergeron, T., 1968: Studies of the orogenic effect on the areal fine structure of rainfall distribution. Meteorological Institute, Uppsala University, Rep. 6, 42 pp.

[6] Bond, N. A., and R. G. Fleagle, 1988: Prefrontal and Postfrontal Boundary Layer Processes over the Ocean. *Mon. Wea. Rev*., 116, 1257–1273.

[7] Bond, N. A., and Coauthors, 1997: The Coastal Observation and Simulation with Topography (COAST) Experiment. *Bull. Amer. Meteor. Soc.*, 78, 1941–1955.

[8] Bougeault, P., and Coauthors, 2001: The MAP Special Observing Period. *Bull Amer. Meteor. Soc*., 82, 433-462.

[9] Bringi, V. N., G.-J. Huang, V. Chandrasekar, and E. Gorgucci, 2002: A methodology for estimating the parameters of a gamma raindrop size distribution model from polarimetric radar data: Application to a squall-line event from the TRMM/Brazil campaign. *J. Atmos. Oceanic Technol.*, **19**, 633–645.

[10] Bringi, V. N., C. R. Williams, M. Thurai, and P. T. May, 2009: Using Dual-Polarized Radar and Dual-Frequency Profiler for DSD Characterization: A Case Study from Darwin, Australia. *J. Atmos. Oceanic Technol.*, 26, 2107–2122.

[11] Browning, K. A., 1974: Mesoscale structure of rain systems in the British Isles. J. Meteor. Soc. Japan, 50, 314-327.

[12] Cannon, D. J., D. J. Kirshbaum, and S. L. Gray, 2012: Under what conditions does embedded convection enhance orographic precipitation? *Quart. J. Roy. Meteor. Soc*., 138, 391–406.

[13] Chase, R. J., and coauthors, 2018: Evaluation of Triple-Frequency Radar Retrieval of Snowfall Properties using Coincident Airborne In-Situ Observations during OLYMPEX. *Geophys. Res. Lett.*, 45, 5752-5760.

[14] Ciesielski, P. E., and Coauthors, 2014: Quality-Controlled Upper-Air Sounding Dataset for DYNAMO/CINDY/AMIE: Development and Corrections. J. *Atmos. Oceanic Technol*., 31, 741–764.

[15] Colle, B. A., and C. F. Mass, 1996: An Observational and Modeling Study of the Interaction of Low-Level Southwesterly Flow with the Olympic Mountains during COAST IOP 4. *Mon. Wea. Rev*., 124, 2152–2175.

[16] Colle, B. A., 2004: Sensitivity of orographic precipitation to changing ambient conditions and terrain geometries: An idealized modeling perspective. *J. Atmos. Sci*., 61, 588–606.

[17] Colle, B. A., 2008: Two-Dimensional Idealized Simulations of the Impact of Multiple Windward Ridges on Orographic Precipitation. *J. Atmos. Sci*. 65, 509-523.

[18] Conrick, R. J., C. F. Mass and Q. Zhong, 2018: Simulated Kelvin_Helmholtz Waves Over Terrain and Their Microphysical Implications. *J. Atmos. Sci*, 75, 2787-2800.

[19] Conrick, R. J., and C. F. Mass, 2019: Evaluating simulated microphysics during OLYMPEX using GPM satellite observations. *J. Hydrometeor.*, in press.

[20] Currier, W. R., T. Thorson and J. D. Lundquist, 2017: Independent Evaluation of Frozen Precipitation from WRF and PRISM in the Olympic Mountains, WA, USA. *J. Hydrometeor.* 18, 2681-2703.

[21] Daly, C., M. Halbleib, J. I. Smith, W. P. Gibson, M. K. Doggett, G. H. Taylor, J. Curtis, and P. P. Pasteris, 2008: Physiographically sensitive mapping of climatological temperature and precipitation across the conterminous United States. Intl. *J. Climatol.*, 28, 2031–2064.

[22] Durden, S. L. and S. Tanelli. 2018. GPM Ground Validation Airborne Precipitation Radar 3rd Generation (APR-3) OLYMPEX V2. NASA Global Hydrology Center DAAC, accessed 8 May 2018.

[23] Durran, D. R., and J. B. Klemp, 1982: On the Effects of Moisture on the Brunt-Väisälä Frequency. *J. Atmos. Sci.*, 39, 2152–2158, doi:10.1175/1520-0469(1982)039<2152:OTEOMO>2.0.CO;2.

[24] Durran, D. R., 1990: Mountain Waves and Downslope Winds. Atmospheric Processes over Complex Terrain, W. Blumen, Ed., American Meteorological Society, Boston, MA, 59–81 http://link.springer.com/10.1007/978-1-935704-25-6_4.

[25] Ferraro, R. R., E. A. Smith, W. Berg, and G. J. Huffman, 1998: A Screening Methodology for Passive Microwave Precipitation Retrieval Algorithms. *J. Atmos. Sci.*, 55, 1583–1600.

[26] Fraser, A. B., R. C. Easter and P. V. Hobbs, 1973: A theoretical study of the flow of air and fallout of solid precipitation over mountainous terrain. Part I: Airflow model. *J. Atmos. Sci*., 30, 801–812.

[27] Frei, C., and C. Schär, 1998: A precipitation climatology of the Alps from high-resolution rain-gauge observations. Int. J. Climatol., 18, 873–900.

[28] Garreaud, R., M. Falvey, and A. Montecinos, 2016: Orographic Precipitation in Coastal Southern Chile: Mean Distribution, Temporal Variability, and Linear Contribution. *J. Hydrometeor.*, 17, 1185–1202.

[29] Garvert, M. F., B. A. Colle, and C. F. Mass, 2005: The 13–14 December 2001 IMPROVE-2 event. Part I: Synoptic and mesoscale evolution and comparison with a mesoscale model simulation. J. *Atmos. Sci.,* 62, 3474–3492.

[30] Grell, G. A., and S. R. Freitas, 2014: A scale and aerosol aware stochastic convective parameterization for weather and air quality modeling. *Atmos. Chem. Phys*., 14, 5233–5250, https:// doi.org/10.5194/acp-14-5233-2014.

[31] Hardin, J. and N. Guy, 2017: PyDisdrometer: Python Library for Working with Disdrometer Data, doi: http://doi.org/10.5281/zenodo.9991.

[32] Hecht, C. W., and J. M. Cordeira, 2017: Characterizing the influence of atmospheric river orientation and intensity on precipitation distributions over North Coastal California: ARs and Precipitation Over North Coastal CA. *Geophys. Res. Lett*. 44, 9048–9058.

[33] Helmus, J., and S. Collis, 2016: The Python ARM Radar Toolkit (Py-ART), a Library for Working with Weather Radar Data in the Python Programming Language. *Journal of Open Research Software*, **4**, doi:10.5334/jors.119. http://openresearchsoftware.metajnl.com/articles/10.5334/jors.119/ (Accessed April 3, 2017).

[34] Hobbs, P. V., 1978: Organization and structure of clouds and precipitation on the mesoscale and microscale in cyclonic storms. *Rev. Geophys.*, 16, 741–755.

[35] Hobbs, P. V., R. C. Easter, and A. B. Fraser, 1973: A Theoretical Study of the Flow of Air and Fallout of Solid Precipitation Over Mountainous Terrain: Part II. Microphysics. *J. Atmos. Sci*., 30, 813–823.

[36] Hobbs, P. V., L. F. Radke, A. B. Fraser, J. D. Locatelli, C. E. Robertson, D. G. Atkinson, R. J. Farver, R. R. Weiss, and R. C. Easter, 1971: Studies of winter cyclonic storms over the Cascade Mountains (1970-71), *Res. Rep*. 6, 306 pp., Cloud Phys. Group, Univ. of Wash., Seattle. [Available online at: http://carg.atmos.washington.edu/sys/research/archive/winter_cyclonic.pdf]

[37] Hong, S.-Y., Y. Noh, and J. Dudhia, 2006: A new vertical diffusion package with an explicit treatment of entrainment processes. *Mon. Wea. Rev*., 134, 2318–2341.

[38] Horel, J., and Coauthors, 2002: Mesowest: Cooperative Mesonets in the Western United States. *Bull. Amer. Meteor. Soc.*, 83, 211–225.

[39] Houze, R. A., Jr., J. D. Locatelli, and P. V. Hobbs, 1976: Dynamics and Cloud Microphysies of the Rainbands in an Occluded Frontal System1. *J. Atmos. Sci.*, 33, 1921–1936.

[40] Houze, R. A., Jr., 1981: Structures of atmospheric precipitation systems–A global survey. *Radio Science*, 16, 671-689.

[41] Houze, R. A., C. N. James, and S. Medina, 2001: Radar observations of precipitation and airflow on the Mediterranean side of the Alps: Autumn 1998 and 1999. *Quart. J. Roy. Meteor. Soc*., 127, 2537–2558.

[42] Houze, R. A., Jr., and S. Medina, 2005: Turbulence as a Mechanism for Orographic Precipitation Enhancement. *J. Atmos. Sci.*, 62, 3599–3623.

[43] Houze, R. A., Jr., 2012: Orographic effects on precipitating clouds. *Rev. Geophys*., 50, RG1001, 47pp.

[44] Houze, R. A., Jr., 2014: Cloud Dynamics, 2nd Ed., Elsevier/Academic Press, Oxford, 432 pp.

[45] Houze, R. A., Jr., and Coauthors, 2017: The Olympic Mountains Experiment (OLYMPEX). *Bull. Amer. Meteor. Soc.*, 98, 2167-2188.

[46] Iacono, M. J., J. S. Delamere, E. J. Mlawer, M. W. Shephard, S. A. Clough, and W. D. Collins, 2008: Radiative forcing by longlived greenhouse gases: Calculations with the AER radiative transfer models. *J. Geophys. Res*., 113, D13103.

[47] Iguchi, T., and R. Meneghini, 1994: Intercomparison of Single-Frequency Methods for Retrieving a Vertical Rain Profile from Airborne or Spaceborne Radar Data. *J. Atmos. Oceanic Technol.*, **11**, 1507–1516.

[48] James, C. N., and R. A. Houze, 2005: Modification of Precipitation by Coastal Orography in Storms Crossing Northern California. *Mon. Wea. Rev.*, 133, 3110–3131.

[49] Jankov, I., J.-W. Bao, P. J. Neiman, P. J. Schultz, H. Yuan, and A. B. White, 2009: Evaluation and comparison of microphysical algorithms in ARW-WRF model simulations of atmospheric river events affecting the California coast. J. Hydrometeor., 10, 847–870.

[50] Jiang Q. and Smith, R. B. 2003: Cloud timescales and orographic precipitation. *J. Atmos. Sci*. 60, 1543–1559.

[51] Kingsmill, D. E., P. J. Neiman, F. M. Ralph, and A. B. White, 2006: Synoptic and topographic variability of Northern California precipitation characteristics in landfalling winter storms observed during CALJET. *Mon. Wea. Rev.*, 134, 2072–2094.

[52] Kingsmill, D. E., P. J. Neiman, and A. B. White, 2016: Microphysics Regime Impacts on the Relationship between Orographic Rain and Orographic Forcing in the Coastal Mountains of Northern California. *J. Hydrometeor.*, 17, 2905–2922.

[53] Kreitzberg, C. W., and H. A. Brown, 1970: Mesoscale weather systems within an occlusion. *J. Appl. Meteor*., 9,417-432.

[54] Kumjian, M. R., S. A. Rutledge, R. M. Rasumssen, P. C. Kennedy, and M. Dixon, 2014: High-resolution polarimetric radar observations of snow-generating cells*, J. Appl. Metor. Climatol*., 53, 1636-1658.

[55] Kummerow, C. D., S. Ringerud, J. Crook, D. Randel and W. Berg, 2010. An observationally generated *A-Priori* database for microwave rainfall retrievals, *J. Atmos. and Oceanic Tech*., 28(2), 113-130.

[56] Kummerow, Christian D., David L. Randel, Mark Kulie, Nai-Yu Wang, Ralph Ferraro, S. Joseph Munchak, and Veljko Petkovic, 2015: The evolution of the goddard profiling algorithm to a fully parametric scheme. *J. Atmos. Oceanic Technol.*, 32, 2265–2280.

[57] von Lerber, A., D. Moisseev, L. F. Bliven, W. Petersen, A.-M. Harri, and V. Chandrasekar, 2017: Microphysical Properties of Snow and Their Link to Ze – S Relations during BAECC 2014. *J. Appl. Meteor.*, 56, 1561–1582.

[58] von Lerber, A. D., D. Moisseev, D. A. Marks, W. Petersen, A.-M. Harri, and V. Chandrasekar, 2018: Validation of GMI Snowfall Observations by Using a Combination of Weather Radar and Surface Measurements. *J. Appl. Meteor.*, 57, 797–820.

[59] Locatelli, J. D., and P. V. Hobbs, 1987: The mesoscale and microscale structure and organization of clouds and precipitation in midlatitude cyclones. XIII: Structure of a warm front. *J. Atmos. Sci.*, 44, 2290–2309.

[60] Markowski, P. and Y. Richardson, 2010: Mesoscale Meteorology in Midlatitudes, Wiley-Blackwell, 430pp.

[61] Martner, B. E., S. E. Yuter, A. B. White, S. Y. Matrosov, D. E. Kingsmill, and F. M. Ralph, 2008: Raindrop Size Distributions and Rain Characteristics in California Coastal Rainfall for Periods with and without a Radar Bright Band. *J. Hydrometeor.*, **9**, 408–425.

[62] Mass, C. F., and G. K. Ferber, 1990: Surface Pressure Perturbations Produced by an Isolated Mesoscale Topographic Barrier. Part I: General Characteristics and Dynamics. *Mon. Wea. Rev.*, 118, 2579–2596.

[63] Mass, C., N. Johnson, M. Warner, and R. Vargas, 2015: Synoptic Control of Cross-Barrier Precipitation Ratios for the Cascade Mountains. *J. Hydrometeor.*, 16, 1014–1028.

[64] Massman, A. K., J. R. Minder, R. D. Garreaud, D. E. Kingsmill, R. A. Valenzuela, A. Montecinos, S. L. Fults, and J. R. Snider, 2017: The Chilean Coastal Orographic Precipitation Experiment: Observing the influence of microphysical rain regime on coastal orographic precipitation, *J. Hydrometeor.*, 18, 2723–2743.

[65] Matejka, T. J., R. A. Houze, and P. V. Hobbs, 1980: Microphysics and dynamics of clouds associated with mesoscale rainbands in extratropical cyclones. *Q.J.R. Meteorol. Soc.*, 106, 29–56.

[66] McMurdie, L. A., A. K. Rowe, R. A. Houze, Jr., S. R. Brodzik, J. P. Zagrodnik and T. M. Schuldt, 2018: Terrain-Enhanced Precipitation Processes above the Melting Layer; Results from OLYMPEX. *J. Geo. Res*., 123.

[67] Medina, S., E. Sukovich, and R. A. Houze, 2007: Vertical Structures of Precipitation in Cyclones Crossing the Oregon Cascades. *Mon. Wea. Rev.*, 135, 3565–3586.

[68] Medina, S., and R. A. Houze, Jr., 2003: Air motions and precipitation growth in Alpine storms. *Quart. J. Roy. Meteor. Soc*., special MAP issue, 129, 345-371.

[69] Medina, S., B. F. Smull, R. A. Houze, Jr., and M. Steiner, 2005: Cross-barrier flow during orographic precipitation events: Results from MAP and IMPROVE. *J. Atmos. Sci*., 62, 3580-3598.

[70] Medina, S., and R. A. Houze, Jr., 2015: Small-Scale Precipitation Elements in Midlatitude Cyclones Crossing the California Sierra Nevada. *Mon. Wea. Rev.*, 143, 2842–2870.

[71] Mesinger, F., and Coauthors, 2006: North American Regional Reanalysis. *Bull. Amer. Meteor. Soc.*, 87, 343–360.

[72] Minder, J. R., D. R. Durran, G. H. Roe, and A. M. Anders, 2008: The climatology of small-scale orographic precipitation over the Olympic Mountains: Patterns and processes. *Q.J.R. Meteorol. Soc.*, 134, 817–839.

[73] Minder, J. R., D. R. Durran, and G. H. Roe, 2011: Mesoscale Controls on the Mountainside Snow Line. *J. Atmos. Sci.*, 68, 2107-2127.

[74] Nagle, R. E., and S. M. Serebreny, 1962: Radar Precipitation Echo and Satellite Cloud Observations of a Maritime Cyclone1. *J. Appl. Meteor.*, **1**, 279–295.

[75] NOAA/OAR/ESRL PSD, 2004: North American Regional Reanalysis Data from NCEP Global Reanalysis, accessed 24 August 2016. [Data available online at: https://www.esrl.noaa.gov/psd/data/gridded/data.narr.html]

[76] Neiman, P. J., F. M. Ralph, A. B. White, D. E. Kingsmill, and P. O. G. Persson, 2002: The Statistical Relationship between Upslope Flow and Rainfall in California's Coastal Mountains: Observations during CALJET. *Mon. Wea. Rev.*, 130, 1468–1492.

[77] Neiman, P. J., F. M. Ralph, G. A. Wick, J. D. Lundquist, and M. D. Dettinger, 2008: Meteorological Characteristics and Overland Precipitation Impacts of Atmospheric Rivers Affecting the West Coast of North America Based on Eight Years of SSM/I Satellite Observations. *J. Hydrometeor.*, **9**, 22–47.

[78] Neiman, P. J., and Coauthors, 2016: An Airborne and Ground-Based Study of a a Long-Lived and Intense Atmospheric River with Mesoscale Frontal Waves Impacting California during CalWater-2014, *Mon. Wea. Rev.*, 144, 1115-1144.

[79] Nešpor, V., and B. Sevruk, 1999: Estimation of Wind-Induced Error of Rainfall Gauge Measurements Using a Numerical Simulation. *J. Atmos. Oceanic Technol.*, **16**, 450–464.

[80] Newman, A. J., P. A. Kucera, and L. F. Bliven, 2009: Presenting the Snowflake Video Imager (SVI). *J. Atmos. Oceanic Technol*., 26, 167–179.

[81] Newell, R. E., N. E. Newell, Y. Zhu, and C. Scott, 1992: Tropospheric rivers? – A pilot study. *Geophys. Res. Lett.*, 19, 2401–2404.

[82] Niu, Guo–Yue and Coauthors, 2011: The community Noah land surface model with multiparameterization options (Noah–MP): 1. Model description and evaluation with local–scale measurements. *J. Geophys. Res*., 116, D12109.

[83] NWAC, 2018: Northwest Avalanche Center Weather Station Data Portal—Olympics Region, continuing from 2014 (updated daily). Northwest Avalanche Center, accessed 23 April 2018, https://www.nwac.us/data-portal/location/hurricane-ridge/.

[84] Petersen, W. A., D. Wolff, J. Wang, and Ali Tokay. 2017a. GPM Ground Validation Met One Rain Gauge Pairs OLYMPEX. Subset used: All sites, November-December 2015. NASA Global Hydrology Center DAAC, accessed 23 April 2018.

[85] Petersen, W. A., A. Tokay and P. N. Gatlin, 2017b: GPM Ground Validation Pluvio Precipitation Gauges OLYMPEX. Subset used: Wynoochee site, November-December 2015. NASA Global Hydrology Center DAAC, accessed 23 April 2018.

[86] Petersen, W. A., A. Tokay, P. N. Gatlin ,and M. T. Wingo. 2017c. GPM Ground Validation Autonomous Parsivel Unit (APU) OLYMPEX. Subset used: APU03 and APU06, November-December 2015. NASA Global Hydrology Center DAAC, accessed 28 March 2018.

[87] Picard, L., and C. Mass, 2017: The Sensitivity of Orographic Precipitation to Flow Direction: An Idealized Modeling Approach. *J. Hydrometeor*., 18, 1673–1688.

[88] Purnell, D. J., and D. J. Kirshbaum, 2018: Synoptic Control over Orographic Precipitation Distributions during the Olympics Mountains Experiment (OLYMPEX). *Mon. Wea. Rev.*, 146, 1023–1044.

[89] Ralph, F. M., and Coauthors, 1999: The California Land-falling Jets Experiment (CALJET): Objectives and design of a coastal atmosphere–ocean observing system deployed during a strong El Niño. Preprints, *Third Symp. on Integrated Observing Systems,* Dallas, TX, Amer. Meteor. Soc., 78–81.

[90] Ralph, F. M., P. J. Neiman, and G. A. Wick, 2004: Satellite and CALJET Aircraft Observations of Atmospheric Rivers over the Eastern North Pacific Ocean during the Winter of 1997/98. *Mon. Wea. Rev.*, 132, 1721–1745.

[91] Roe, G. H., 2005: Orographic precipitation, Annu. Rev. *Earth Planet. Sci*., 33, 645–671.

[92] Rotunno, R., and R. Ferretti, 2001: Mechanisms of intense alpine rainfall, *J. Atmos. Sci*., 58, 1732–1749.

[93] Sikora, T. D., G. S. Young, C. M. Fisher, and M. D. Stepp, 2011: A Synthetic Aperture Radar–Based Climatology of Open-Cell Convection over the Northeast Pacific Ocean. *J. Appl. Meteor.,* 50, 594–603.

[94] Siler, N., and D. Durran, 2016: What Causes Weak Orographic Rain Shadows? Insights from Case Studies in the Cascades and Idealized Simulations. *J. Atmos. Sci*., 73, 4077–4099.

[95] Simpson, J. E., 1997: Gravity currents in the environment and the laboratory. Cambridge University Press, 262pp.

[96] Skamarock, W. C., J. B. Klemp, J. Dudhia, D. O. Gill, D. M. Barker, W. Wang, and J. G. Powers, 2005: A description of the Advanced Research WRF version 2. NCAR Tech. Note NCAR/TN-4681STR, 88 pp.

[97] Stoelinga, M. T., and Coauthors, 2003: Improvement of Microphysical Parameterization through Observational Verification Experiment. *Bull. Amer. Meteor. Soc.*, 84, 1807–1826.

[98] Skofronick-Jackson, G. and coauthors, 2017: The Global Precipitation Measurement (GPM) Mission for Science and Society. *Bull. Amer. Meteor. Soc*, 98(8), 1679–1695.

[99] Smith, R. B., 1979: The influence of mountains on the atmosphere, *Adv. Geophys*., 21, 87–230.

[100] Smith, R. B. and I. Barstad, 2004: A linear theory of orographic precipitation. *J. Atmos. Sci*., 61, 1377–1391.

[101] Stoelinga, M. T., and Coauthors, 2003: Improvement of Microphysical Parameterization through Observational Verification Experiment. *Bull. Amer. Meteor. Soc.*, 84, 1807–1826.

[102] Testud, J., S. Oury, R. A. Black, P. Amayenc, and X. Dou, 2001: The Concept of "Normalized" Distribution to Describe Raindrop Spectra: A Tool for Cloud Physics and Cloud Remote Sensing. *J. Appl. Meteor.*, 40, 1118–1140.

[103] Thompson, G., P.R. Field, R.M. Rasmussen, and W.D. Hall, 2008: Explicit Forecasts of Winter Precipitation Using an Improved Bulk Microphysics Scheme. Part II: Implementation of New Snow Parameterization. *Mon. Wea. Rev*., 136:12, 5095-5115.

[104] Thompson, E. J., S. A. Rutledge, B. Dolan, and M. Thurai, 2015: Drop Size Distributions and Radar Observations of Convective and Stratiform Rain over the Equatorial Indian and West Pacific Oceans. *J. Atmos. Sci.*, 72, 4091–4125.

[105] Tokay, A., D. B. Wolff, and W. A. Petersen, 2014: Evaluation of the New Version of the Laser-Optical Disdrometer, OTT Parsivel2. *J. Atmos. Oceanic Technol.*, 31, 1276–1288.

[106] Ulbrich, C. W., 1983: Natural Variations in the Analytical Form of the Raindrop Size Distribution. *J. Climate Appl. Meteor.*, 22, 1764–1775.

[107] Viale, M., R. A. Houze, and K. L. Rasmussen, 2013: Upstream Orographic Enhancement of a Narrow Cold-Frontal Rainband Approaching the Andes. *Mon. Wea. Rev.*, 141, 1708–1730.

[108] Warner, M. D., C. F. Mass, and E. P. Salathé, 2012: Wintertime Extreme Precipitation Events along the Pacific Northwest Coast: Climatology and Synoptic Evolution. *Mon. Wea. Rev.*, 140, 2021–2043.

[109] White, A. B., P. J. Neiman, F. M. Ralph, D. E. Kingsmill, and P. O. G. Persson, 2003: Coastal Orographic Rainfall Processes Observed by Radar during the California Land-Falling Jets Experiment. *J. Hydrometeor.*, **4**, 264–282.

[110] White, A. B., P. J. Neiman, J. M. Creamean, T. Coleman, F. M. Ralph, and K. A. Prather, 2015: The impacts of California's San Francisco Bay Area gap on precipitation observed in the Sierra Nevada during HMT and CalWater. *J. Hydrometeor.,* 16, 1048–1069.

[111] Willis, P. T., 1984: Functional fits to some observed drop size distributions and parameterization of rain. *J. Atmos. Sci.*, 41, 1648–1661.

[112] Zagrodnik, J. P., L. McMurdie and R. A. Houze, Jr, 2018: Stratiform Precipitation Processes in Cyclones Passing over a Coastal Mountain Range. *J.Atmos.Sci*., 75, 983-1004.

[113] Zagrodnik, J. P., L. McMurdie, R. A. Houze, Jr., and S. Tanelli, 2019: Vertical Structure and Microphysical Characteristics of Frontal Systems Passing over a Three-Dimensional Coastal Mountain Range, *J.Atmos.Sci.,* in press.

[114] Zangl G. 2007: Interaction between dynamics and cloud microphysics in orographic precipitation enhancement: Ahigh-resolution modeling study of two north Alpine heavy-precipitation events. *Mon. Weather Rev.* 135, 2817–2840.

[115] Zhu, Y., and R. E. Newell, 1994: Atmospheric rivers and bombs. *Geophys. Res. Lett.*, 21, 1999–2002.

[116] Zhu, Y., and R. E. Newell, 1998: A Proposed Algorithm for Moisture Fluxes from Atmospheric Rivers. *Mon. Wea. Rev.*, 126, 725–735.

VITA

Joseph P. Zagrodnik was born in St. Louis, Missouri and grew up in Milwaukee, Wisconsin. He became interested in weather at a young age and has fond memories of many severe thunderstorm outbreaks and blizzards from the 1990s. His interest in science was fostered by his parents, Miss Provencher (his third grade teacher), and his favorite meteorologists on the Weather Channel and local news.

Joseph attended the University of Wisconsin-Madison and received bachelor's degrees in Atmospheric & Oceanic Sciences and History. While he was a student, he participated in a research trip to Storm Peak Laboratory in Steamboat Springs, Colorado, chased storms in Nebraska and South Dakota, and worked part-time as a data and graphics technician at Weather Central, LLC in Madison, WI. Joseph then joined Haiyan Jiang's research group at Florida International University in Miami, FL where he received a Master of Science in Geosciences with a Meteorology concentration for his studies on the role of precipitation and latent heating in the rapid intensification of tropical cyclones.

Joseph joined the Mesoscale Group at the University of Washington in 2013. His research focused on the modification of precipitation in mid-latitude cyclones passing over coastal mountain ranges. He participated in the Olympic Mountains Experiment (OLYMPEX) from 2014-2016 and was extensively involved in the testing, deployment, and maintenance of the ground instrumentation network. As a graduate student he co-lead the department's WxChallenge forecasting team for 5 years. Joseph graduated from the University of Washington with a Doctor of Philosophy in 2019.